72-29,912

SHEETS, Robert C., 1937-
ANALYSIS OF STORMFURY DATA USING THE VARIATIONAL OPTIMIZATION APPROACH.

The University of Oklahoma, Ph.D., 1972
Physics, meteorology

University Microfilms, A XEROX Company, Ann Arbor, Michigan

THE UNIVERSITY OF OKLAHOMA

GRADUATE COLLEGE

ANALYSIS OF STORMFURY DATA USING THE VARIATIONAL OPTIMIZATION APPROACH

A DISSERTATION

SUBMITTED TO THE GRADUATE FACULTY

in partial fulfillment of the requirements for the

degree of

DOCTOR OF PHILOSOPHY

BY

ROBERT C. SHEETS

Norman, Oklahoma

1972

ANALYSIS OF STORMFURY DATA

USING THE VARIATIONAL OPTIMIZATION APPROACH

APPROVED BY

[signatures]

DISSERTATION COMMITTEE

ACKNOWLEDGMENTS

Professor Sasaki deserves considerable credit for his scientific advice, without which the research reported on in this paper would not have been completed. In addition, he has provided personal and scientific guidance over the past eight years which has enabled the author to reach the point in academic accomplishments represented by this work. Considerable computer time on the University of Oklahoma IBM 360 and 1130 systems as well as the CDC 6600 and 7600 at the National Center for Atmospheric Research was also provided through the efforts of Professor Sasaki.

The basis for the work presented in this paper has evolved from more than six years of research effort by the author at the NOAA National Hurricane Research Laboratory and during a year at the University of Oklahoma under a NOAA scholarship. Scientific direction and advice have been received from Dr. R. Cecil Gentry, Dr. Harry F. Hawkins, Dr. Stanley L. Rosenthal, and Dr. Banner I. Miller during this period. Almost the entire staff of NHRL have contributed to some phase of the research effort and getting this paper in a form for publication. The primary people involved and their respective contributions are Messrs S. Pearce and R. Sourbeer (data processing), Mrs. R. Sherill, Miss L. Kelly, and Mr. C. Meeks (data plotting, etc.), Messrs R. Carrodus, D. Senn, M. Cudlipp and D. Shields (drafting), Mr. C. True (photography), and Mrs. C. Delgado and Mrs. S. Keen (typing).

Special thanks is also due to Mrs. Keven Amrein of the University Oklahoma Department of Meteorology who typed the final manuscript, and to the operational crews of the NOAA Research Flight Facility aircraft who collected the majority of the data used in this study. These crews often do not receive the credit that they deserve for the considerable effort required in these research missions. The author has participated in these hurricane research missions over the past 7 years and continues to be impressed by the cooperation and enthusiasm of the crews in their efforts to obtain the desired data.

Portions of this research effort were supported by NSF Grant #GA-30976.

ABSTRACT

The variational optimization technique is used to develop an analysis scheme for application to the high energy portion of a hurricane (wind speeds of 30 kt or more contained in the storm circulation). The derived analysis equations are used to filter the data in an attempt to obtain the signal for selected scales of motion. The design of the filters used in this study was based on empirical evidence. These filters are also used to develop variability factors for the standard meteorological variables and selected scales of motion. A second set of analysis equations is derived which includes the first set as well as the gradient wind condition.

The analysis schemes are applied to data collected in Hurricane Debbie (1969) during two artificial modification attempts. The results of these analyses are then used to define a more explicit seeding hypothesis which can be used in the explanation and statistical evaluation of future seeding experiments.

The validity of the technique is based on empirical evidence since statistical evaluation is quite difficult to obtain. While it is felt that strong physical inferences can be drawn from the analysis results, more such data analyses are required before strong statistical support can be claimed.

TABLE OF CONTENTS

LIST OF TABLES

Table | Page

LIST OF ILLUSTRATIONS

Figure		Page

Figure Page

Figure | Page

Figure		Page

ANALYSIS OF STORMFURY DATA USING THE VARIATIONAL OPTIMIZATION APPROACH

CHAPTER I

INTRODUCTION

Two basic questions must be answered in any attempt to determine possible effects of artificial modification attempts. The first question which should be answered is what changes in structure or intensity actually occurred. The second question is were all or any portion of these changes a result of the modification experiments. This approach attempts to provide answers for the first question and presents strong evidence for answering the second.

There are many background questions which must also be considered before looking at the details for the particular cases. For instance, what is the likelihood that a hurricane goes through a natural diurnal variation? The seeding cases studied in this paper were continuously monitored for nearly twenty four hours and the actual seeding occurred over a ten hour period. Therefore, any natural diurnal variation would have to be considered in the analysis. Many other factors must be taken into account in the analysis, such as are changes in intensity of the hurricanes related to the location of the storm, or is there any correlation between the size of the hurricane eye and its present or future changes in intensity? Do stronger or weaker storms or intensifying or decaying storms exhibit characteristic fluctuations? There are many more questions similar to these which could be asked and the author has attempted to answer many of these questions in previous papers (Sheets, 1969, 1970, 1972a,b).

Theoretically, it would appear to be a simple matter to determine what changes occur. However, in practice, this becomes a very difficult problem.

Highly instrumented aircraft have been collecting invaluable information within the high energy portion of the hurricane for the past few years. Many problems associated with the processing of the data collected have been encountered and solved. However, some significant sources of error continue to plague the researcher when analyzing these data. One such source of error is in positioning the data with respect to some fixed reference point such as the center of the moving storm. This center is usually taken as the geometric center of the "eye" of the storm as determined by radar. Often the radar eye is not circular and sometimes is discontinuous. Even more detrimental is the fact that continuous displays of the radar center are not always available. In addition, the doppler radar system is affected by the moving surface water and heavy precipitation and can contribute to these position errors. Other parameters also contain significant sources of errors and the result is that considerable effort is required in the processing of these data. Much skill and knowledge has been attained in the art of processing these data over recent years and is directed at minimizing these errors. However, significant errors remain in the processed data.

Several case studies of the high energy portion of the hurricane have been completed over the past few years. These studies show a variety of types, sizes and strengths of hurricanes. For instance, Hurricanes Dora (1964) (Sheets, 1968), and Helene (1958) (Colon, 1964) were relatively strong storms which covered a very large area while Hurricane Daisy (1958) (Colon, 1961) was a small, concentrated, intense storm during the period investigated. Hurricanes Hilda (1964) (Hawkins & Rubsam, 1968) and Cleo (1958) (La Seur & Hawkins, 1963) were somewhere between these two extremes in size and structure while Janice (1958) and Ella (1962)(Sheets, 1967a,b) were generally less organized than any of the above storms during the period of the studies. However, there were many common features for all these storms.

Quite pertinent to this study is the presence of small areas of extremum (maximum and minimum) values of the various parameters such as wind speed, temperature, and moisture, as shown in the horizontal analyses. Often, these maximum centers are associated with major rainbands or strong cells within the rainbands. These features apparently circulate, propagate, or form and dissipate around the storm center and are quite prominent in the mid and lower troposphere. The result of this natural condition is that large fluctuations of a given variable such as wind speed are observed both in space and time. For instance, it is not uncommon to note wind speed changes of as much as 30 percent or more in a few minutes time at a position fixed with respect to the storm center. Fluctuations of this same magnitude are observed over short horizontal distances in space. Both of these features are readily apparent in the analyses of Hurricane Dora on September 7 and 8, 1964 (Sheets, 1968). These fluctuations can easily mask changes in the mesoscale intensity or structure of the storm. We would like to study all scales present, but this would require a density of data in both time and space which is not operationally possible to obtain at this time.

It appears that much of the large fluctuations are contained in a few selected scales of motion. If this is true, then it seems necessary to determine what these scales are, their contributions to the total change, their conservativeness from hour to hour, day to day, and storm to storm, and whether or not these features are affected by specified types of artificial modification attempts. In order to accomplish this task, some filtering techniques must be devised which will effectively separate the contributions from the desired scales of motion. An indication of the probable success of this approach was attained in an earlier study by the author (unpublished) which showed that simple filtering techniques considerably decreased the magnitude of the changes. For instance, some short space and time averages of the maximum wind speed bands reduced the fluctuation of the maximum wind speed to less than one third of its original value in four of five storms studied and still appeared sensitive to major changes. Standard filtering techniques seem to be somewhat difficult to apply due to the overwhelming percentage of the variance being contained in the longer wavelength features. Unequal data length records, large variations in end point values and mispositioned data present other problems of significant magnitude. The removal of some mean profile would allow one to study the smaller scale features in more detail. However, the construction of this profile is quite arbitrary and mispositioned data could give very large misleading results. Many of the more refined techniques become quite complicated and, even more damaging, require a considerable number of fixed end point values. The variational optimization approach offers a method of obtaining nearly the same information with much less difficulty as well as providing a systematic method for filling in missing data.

A major portion of this study was directed at developing and applying the variational optimization technique to the data collected in Hurricane Debbie on August 18 and 20, 1969. Another portion of this study uses the variational optimization approach as a means of determining the degree of the validity of the gradient wind model. A discussion of these techniques will be given in the next chapter.

The filtered data were stratified according to the scale of motion and a determination of the variability of the various parameters within each scale was made. An attempt was made to determine if there was an organized sequence of changes, say from small scales to larger scales. This was done to develop a more explicit seeding hypothesis. Particular emphasis is placed on determining a set of events which may occur with the seeded case and not with the non-seeded case. This approach seems necessary since it is improbable that enough seeding cases will be available in the near future for applying standard statistical tests. The desired result would be that the probability that this set of events would occur naturally would be quite low.

CHAPTER II

HURRICANE DEBBIE (1969) SEEDING EXPERIMENTS AND RELEVANT HYPOTHESES

Rosenthal (1971) has provided an excellent historical review and interpretation of the development and evolution of hurricane "eyewall" seeding hypotheses. Selected excerpts of the report are repeated below, but it is recommended that the reader refer to Chapters IV and V of the report referenced above to obtain a more complete understanding of the "seeding hypothesis evolution".

Many studies have shown that the hurricane "eyewall" cloud is generally located in the region of maximum low-level pressure gradient. Early investigators believed that these wall clouds contained significant quantities of supercooled water. This belief was verified in recent investigations (Sheets, 1969). These facts led Simpson and Malkus (1964) to propose an "eyewall" seeding hypothesis. This hypothesis (referenced as Hypothesis I) is paraphrased by Rosenthal (1971) as follows:

> "if this supercooled water were frozen through nucleation by silver iodide crystals, the released heat of fusion would produce temperature increases; and therefore, hydrostatically, pressure decreases near the region of the strongest pressure gradient. If the central pressure did not concomitantly decrease, a reduction in maximum pressure gradient, and in turn, a reduction in wind speed should be the net result."

(The freezing of the supercooled water, of course, enhances the natural processes of ice crystal growth and splintering, providing many more freezing nuclei, which results in a rapid multiplication of the rate of release of latent heat of sublimation and fusion.)

Rosenthal then offers several arguments indicating a necessary modification of the hypothesis and implied experiments in order to attain the desired results. The most significant of these arguments is that "the fact that the eyewall drives the storm's transverse circulation and seeding this region alone would very likely accelerate this circulation thus providing a more rapid inflow of both angular momentum and water vapor to the eyewall region".

Rosenthal performed several simulated seeding experiments with his numerical hurricane model. The results of these experiments and the physical arguments against Hypothesis I led him and others associated with Project Stormfury to propose a different hypothesis as follows:

> "Hypothesis II differs from Hypothesis I in that the latter calls for seeding the eyewall alone whereas the former suggests seeding either from the eyewall outward or entirely outward from the eyewall. While the logistics of these hypotheses differ only slightly, the physical arguments are substantially different. In Hypothesis II, the basic idea is to stimulate convection and ascent at radii greater than that of the eyewall. The region of stimulated convection is intended to compete with the eyewall for the inflowing air at low levels. If significant portions of the inflow can be diverted upward at the seeded radii, the angular momentum and water vapor supplies to the original eyewall and wind maximum will be reduced. As a consequence, one would expect the original wind maximum to be reduced and the eyewall convection to be diminished."

Calculations by Sheets (1969) indicate that it is difficult to get much more vertical growth of the hurricane eyewall cloud by seeding. This is a result of the very stable condition caused by the release of latent heat at the upper levels. However, as one proceeds outward from the eyewall, the potential for increased growth of clouds extending above the freezing level and containing supercooled water increases markedly. This fact along with the knowledge of the presence of the required supercooled water in the clouds outside the eyewall (Sheets, 1969) offer further evidence supporting Hypothesis II.

The Hurricane Debbie experiments carried out on August 18 and 20 of 1969 were performed in the manner suggested by Hypothesis II. These experiments are described in considerable detail by Gentry (1969). Only that portion directly related to the analysis in this paper is given here. Fig. 1 shows the track and geographical locations of the storm during the two experiments. Fig. 2 shows the pattern of the seeding track. Five seeding runs were made at approximately two hour intervals during each of the two seeding experiments. Fig. 3 shows the monitoring patterns for the various levels and Fig. 4 shows the flight tracks of the NOAA Research Flight Facility DC-6 aircraft. The analysis performed in this paper is based on the data obtained during these missions. There were three monitoring flights at the 12,000 ft level on each of the two seeding days. The pattern basically consisted of two traverses through the center of the storm along the direction of motion and then repetitive traverses normal to the axis of the storm movement for the remainder of the flight. The monitoring missions began some two hours prior to the first seeding run and lasted some four to six hours after the final seeding event. Measurements of the standard meteorological parameters are digitally recorded on magnetic tape at one second intervals (Friedman et al, 1969). These data then go through a rigorous processing procedure where the winds, aircraft position, etc. are recomputed from the raw data recorded on the original tape. This procedure includes calibration of the signal recorded from several instruments. These processed data were then averaged over one nautical mile radial distance intervals from the storm center for input into the analysis scheme developed in the next chapter.

CHAPTER III

DEVELOPMENT OF THE ANALYSIS EQUATIONS AND VARIABILITY FACTORS

The variational technique (Sasaki, 1970b) is used in this paper as a means of filtering and for developing a more explicit seeding hypothesis. The method is based on a functional that defines selected optimization constraints. Two different functionals are used in this study. The first functional, J_1, consists of two low-pass filters with an "observational constraint". The second functional, J_2, contains the "gradient wind constraint" in addition to J_1.

The first functional is defined as follows:

$$J_1 = \int_r \{\beta(\frac{\partial^2\theta}{\partial r^2})^2 + \gamma(\frac{\partial\theta}{\partial r})^2 + \alpha(\theta - \tilde{\theta})^2\} \, dr \, , \qquad (1)$$

where θ is any variable, $\tilde{\theta}$ is the observed value of θ and r is radial distance from the hurricane center. The first two terms act as low-pass filters and the last term is similar to a "least-square fitting" of the derived field to the observations (Wagner, 1971). These three terms will be referred to in the remainder of this paper as the curvature, gradient, and observational constraints,respectively. The quantities α, γ, and β are the weights placed on their respective terms and as will be shown later determine the degree of filtering imposed on the analyses.

The nondimensional finite difference analog for (1) as derived in Appendix A (symbols are defined in Appendix A) become:

$$J_1 = \sum_r \{\beta(\nabla_r{}^2\theta)^2 + \gamma(\nabla_r\theta)^2 + \alpha(\theta - \tilde{\theta})^2\} \Delta r \qquad (2)$$

All terms are quadratic. Therefore, the minimum of the value of the functional will be obtained by taking the first variation of (2) with respect to θ and letting the first variation vanish under the proper boundary condition.

Before performing the manipulations associated with variational calculus, three rules should be noted:

i. Variation and differentiation are permutable processes, thus:

$$\delta\nabla_r\theta = \nabla_r\delta\theta$$

ii. Variation and integration are permutable processes, thus:

$$\delta \sum_r (\ ) = \sum_r \delta\ (\ )$$

and

iii. $$\Sigma\, \varphi\, \nabla_r\, \delta\psi = - \Sigma\, \nabla_r\varphi\cdot\delta\psi$$

where φ and ψ represent arbitrary functions which can include differential operators and δ represents the variational operator.

Applying the above rules and taking the first variation of (2) with respect to θ, we obtain

$$\delta_\theta J_1 = \delta_\theta \sum_r \{\beta(\nabla_r{}^2\theta)^2 + \gamma(\nabla_r\theta)^2 + \alpha(\theta - \tilde{\theta})^2\} \Delta r = 0$$

or

$$\delta_\theta J_1 = \sum_r \{2\beta(\nabla_r{}^2\theta)(\nabla_r{}^2(\delta\theta)) + 2\gamma(\nabla_r\theta)(\nabla_r(\delta\theta)) + 2\alpha(\theta - \tilde{\theta})\delta\theta\} \Delta r = 0 \qquad (3)$$

We now use summation by parts and assume natural boundary conditions (Sasaki, 1969), i.e.,

$$\sum_x \nabla_x (A\delta\theta)\delta x = \sum_x \nabla_x (A)\delta\theta\delta x + \sum_x A\nabla_x (\delta\theta)\delta x$$

which becomes

$$\sum_x A\nabla_x (\delta\theta)\delta x = \sum_x \nabla_x(A)\ \delta\theta\delta x = -\sum_x \nabla_x (A)\delta\theta\delta x$$

when we assume the boundary conditions of $\delta\theta = 0$ and/or $A = 0$ on the boundaries. Therefore, (3) becomes

$$\delta_\theta J_1 = \sum_r \{2\beta\nabla_r^2(\nabla_r^2\theta)\delta\theta - 2\gamma\nabla_r(\nabla_r\theta)\delta\theta + 2\alpha(\theta - \tilde{\theta})\delta\theta\}\ \Delta r = 0$$

or

$$\delta_\theta J_1 = \sum_r \{[2\beta\nabla_r^4\theta - 2\gamma\nabla_r^2\theta + 2\alpha(\theta - \tilde{\theta})]\delta\theta\}\Delta r = 0 \qquad (4)$$

Since the variation $\delta\theta$ is arbitrary, Eq. (4) implies that

$$\beta\nabla_r^4\theta - \gamma\nabla_r^2\theta + \alpha(\theta - \tilde{\theta}) = 0 \qquad (5)$$

which is the classical Euler-Lagrange or Euler equation and also is referred to as the analysis equation in Sasaki's method of variational analysis. This equation is readily solved by standard iterative techniques. The Liebmann method was used for this paper and is illustrated in Appendix A.

Response Function

The response function for the finite difference analog of the analysis Eq. (5) is derived in order to determine the desired values for the weights α, λ, and β. The components of the "true" and analyzed field, $\tilde{\theta}_n$ and θ_n, respectively, are assumed to be represented by

$$\tilde{\theta}_n = Ae^{ikn\Delta r} \text{ and } \theta_n = Be^{ikn\Delta r}$$

$$\theta_{n+1} = Be^{ik(n+1)\Delta r} = Be^{ikn\Delta r}\ e^{ik\Delta r}$$

$$\theta_{n+2} = Be^{ikn\Delta r}\, e^{2ikn\Delta r}$$

$$\theta_{n-1} = Be^{ikn\Delta r}\, e^{-ik\Delta r}$$

$$\theta_{n-2} = Be^{ikn\Delta r}\, e^{-2ik\Delta r} \qquad (6)$$

$$d = \Delta r \quad \text{and} \quad r = n\Delta r$$

where k is the wave number and A and B are constants.

Substituting (6) into (5) we obtain

$$Be^{ikn\Delta r}\{\beta[e^{2ik\Delta r} + e^{-2ik\Delta r} + 6 - 4e^{ik\Delta r} - 4e^{-ik\Delta r}]/\Delta r^4$$
$$- \gamma[e^{ik\Delta r} + e^{-ik\Delta r} - 2]/\Delta r^2 + \alpha\} = \alpha Ae^{ikn\Delta r}$$

or

$$\frac{Be^{ikn\Delta r}}{Ae^{ikn\Delta r}} = \alpha/\{\alpha - \gamma[2\cos k\Delta r - 2]/\Delta r^2 + \beta[2\cos 2k\Delta r - 8\cos k\Delta r + 6]/\Delta r^4\}$$

Defining the response function R to be the ratio of the analyzed value to the true value results in

$$R = \theta/\tilde{\theta}$$

or

$$R = 1/[1 - 2\gamma(\cos k\Delta r - 1)/\alpha\Delta r^2$$
$$+ 2\beta(\cos 2k\Delta r - 4\cos k\Delta r + 3)/\alpha\Delta r^4] \qquad (7)$$

The wavelength L is expressed in multiples of the grid size and desired quantities are defined as

$$L = P\Delta r \qquad k = 2\pi/L$$

or

$$L = 2\pi/k \quad \text{and} \quad \Delta r = L/P = 2\pi/kP \qquad (8)$$

where P is the number of grid intervals per wavelength. Substituting from

(8) into (7) for Δr in all locations, for k in the argument of the cosine function, and introducing the factor k/k_0, where k_0 is some characteristic wave number which is taken as $2\pi/100$n mi in this paper, we obtain

$$R = 1/\{1 - \frac{\alpha}{\gamma}\frac{\alpha k_0{}^2P^2}{2\pi^2}(\frac{k}{k_0})^2[\cos\frac{2\pi}{P} - 1] + \frac{\beta}{\alpha}\frac{k_0{}^2P^4}{32\pi^4}(\frac{k}{k_0})^4[\cos(\frac{4\pi}{P}) - 4\cos(\frac{2\pi}{P}) + 3]\} \quad (9)$$

Substituting for P in (9) where

$$P = L/\Delta r,\ k_0 = \frac{2\pi}{100\text{n mi}},\ k/k_0 = \frac{100}{L} \text{ or } L = 100(\frac{k_0}{k})$$

and

$$\Delta r = 1\text{n mi} \quad \text{or finally, } P = 100/(k/k_0),$$

we obtain

$$R = 1/\{1 - \frac{\alpha}{\gamma}\frac{k_0{}^2}{2\pi^2}(100)^2[\cos(\frac{2\pi(k/k_0)}{100}) - 1] + \frac{\beta}{\gamma}\frac{k_0{}^2(100)^4}{32\pi^4}[\cos(\frac{4\pi(k/k_0)}{100}) - 4\cos(\frac{2\pi(k/k_0)}{100}) + 3]\} \quad (10)$$

Fig. 6 illustrates the above response factor plotted as a function of the wavelength and for selected values of the weights α, γ, and β. Fig. 6 also illustrates the difference between selected low-pass filter response curves. In some cases, the resulting difference has been amplified to make the peak response value equal to 1. These low-pass and band-pass filters are used extensively in the analysis portion of this paper. They will be referred to as filters A, B, and C, and band filters D, E, and F, corresponding to their designation in Fig. 6.

Dynamic Constraint

A simple model which is sometimes applied to portions of the hurricane is the gradient wind model. The gradient wind equation which represents a balance among the centrifugal, coriolis, and pressure gradient forces, which results in circular motion parallel to the iosbars is believed to reasonably describe the relationship between the wind and pressure in most of the high energy portion of the hurricane. This relationship per unit mass can be written mathematically as

$$\frac{c^2}{r} + fc - \frac{1}{\rho}\frac{\partial p}{\partial r} = 0 \tag{11}$$

where

- c is the gradient wind speed
- r is the radial distance from the center of the circulation
- p is pressure
- ρ is the density, and
- f is the coriolis parameter which is assumed to be constant over the range of the storm in this paper, i.e., $f = 4.98802 \times 10^{-5}\ \mathrm{sec}^{-1}$ at 20°N.

Eq. (11) can be rewritten as

$$\frac{c^2}{r} + fc - g\frac{\partial z}{\partial r} = 0 \tag{12}$$

where by use of the hydrostatic approximation the pressure gradient term is rewritten as

$$\frac{1}{\rho}\frac{\partial p}{\partial r} = g\frac{\partial z}{\partial r}$$

A functional containing the observational and gradient wind constraints as well as the two low-pass filters contained in J_1 can be written as

$$J_2 = \int_r \{\alpha(c - \breve{v})^2 + \gamma(z - \breve{z})^2 + \beta(\frac{c^2}{r} + fc - g\,\frac{\partial z}{\partial r})^2$$

$$+ \mu_1(\frac{\partial c}{\partial r})^2 + \mu_2(\frac{\partial^2 c}{\partial r^2}) + \mu_3(\frac{\partial z}{\partial r})^2 + \mu_4(\frac{\partial^2 z}{\partial r^2})^2\}\ dr \qquad (13)$$

where μ_1, μ_2, μ_3, and μ_4 are the respective weights on the low-pass filters, α and γ are the weights on the wind and height observational constraints, respectively,

- β is the weight on the gradient wind constraint
- $\breve{v}$ is the observed wind speed
- $\breve{z}$ is the observed height of the designated pressure surface
- g is the acceleration due to gravity

and the remaining variables are as previously defined.

The nondimensional finite difference analog for (13) as derived in Appendix A is

$$J_2 = \sum_r \{\alpha(c - \breve{v})^2 + \gamma(z - \breve{z})^2 + \beta(\frac{c^2}{r} + \frac{c}{R_0} - \frac{1}{F^2}\nabla_r z)^2$$

$$+ \mu_1(\nabla_r c)^2 + \mu_2(\nabla_r{}^2 c)^2 + \mu_3(\nabla_r z)^2 + \mu_4(\nabla_r{}^2 z)^2\}\ \nabla r \qquad (14)$$

We wish to minimize the summation. Since all terms are quadratic, we take the first variation of the functional (14) with respect to c and z, and then set the result euual to zero. Using the rules of calculus of variations and integration by parts as were previously shown, we obtain

$$\delta_{c,z} J_2 = \delta_{c,z} \sum_r \{\quad\}\Delta r$$

$$= \sum_r \{2\alpha(c - \breve{v})\delta c + 2\gamma(z - \breve{z})\delta z$$

$$+ 2\beta(\frac{c^2}{r} + \frac{c}{R_0} - \frac{1}{F^2}\nabla_r z)(-\frac{1}{F^2}\nabla_r(\delta z))$$

$$+ 2\beta(\frac{c^2}{r} + \frac{c}{R_0} - \frac{1}{F^2}\nabla_r z)(\frac{2c}{r} + \frac{1}{R_0})\delta c$$

$$- 2\mu_1 \nabla_r{}^2 c\delta c + 2\mu_2 \nabla_r{}^4 c\delta c - 2\mu_3 \nabla_r{}^2 z\delta z + 2\mu_4 \nabla_r{}^4 z\delta z\}\Delta r$$

$$= 0$$

or

$$\delta_{c,z}J_2 = \Sigma\{[2\alpha(c - \tilde{v}) + 2\beta(\frac{c^2}{r} + \frac{c}{R_0} - \frac{1}{F^2}\nabla_r z)(\frac{2c}{r} + \frac{1}{R_0})$$

$$- 2\mu_1 \nabla_r{}^2 c + 2\mu_2 \nabla_r{}^4 c]\delta c$$

$$+ [2\gamma(z - z) + 2\frac{\beta}{F^2}(\frac{1}{r}\nabla_r c^2 - \frac{c^2}{r^2} + \frac{1}{R_0}\nabla_r c - \frac{1}{F^2}\nabla_r{}^2 z) \tag{15}$$

$$- 2\mu_3 \nabla_r{}^2 z + 2\mu_4 \nabla_r{}^4 z]\delta z\}\ \Delta r = 0$$

Since δc and δz are arbitrary, we obtain

$$\beta[-\frac{1}{F^2}(\frac{2c}{r} + \frac{1}{R_0})\nabla_r z + \frac{2c^3}{r^2} + \frac{3c^2}{rR_0} + \frac{c}{R_0{}^2}]$$

$$+ \mu_2 \nabla_r{}^4 c - \mu_1 \nabla_r{}^2 c + \alpha(c - \tilde{v}) = 0 \tag{16}$$

and

$$\frac{\beta}{F^2}[-\frac{1}{F^2}\nabla_r{}^2 z + \frac{1}{R_0}\nabla_r c + \frac{1}{r}\nabla_r c^2 - \frac{c^2}{r^2}]$$

$$+ \mu_4 \nabla_r{}^4 z - \mu_3 \nabla_r{}^2 z + \alpha(z - \tilde{z}) = 0 \tag{17}$$

where (16) and (17) are the resulting nondimensional finite difference analogs to the Euler-Lagrange or analysis equations for the functional (13). This set of analysis equations is solved by the Liebmann iterative technique as discussed in Appendix A.

Variability Factors

The variability factors defined and used in this paper are similar to the typical gust factor used in wind analyses. However, the factors defined in this paper are for the selected scales of motion and are defined not only for the wind speed, but also for other standard meteorological parameters. This factor is determined from the filtered quantities and except for the wind speed, uses Jordan's (1958) mean tropical conditions as a base. The mean tropical wind speed is assumed to be small in comparison to the hurricane wind speed and is therefore neglected.

The wind variability associated with scales of motion determined by band-pass filters D, E, and F respectively are defined as

$$\text{VARIB W1} = [\text{BFLTR (D)}]/[\text{FLTR (A)}], \quad (18)$$

$$\text{VARIB W2} = [\text{BFLTR (E)}]/[\text{FLTR (B)}], \quad (19)$$

and

$$\text{VARIB W3} = [\text{BFLTR (F)}]/[\text{FLTR (C)}], \quad (20)$$

where BFLTR (D), (E), and (F) are the absolute values of the analyzed field obtained by applying band filters (D), (E), and (F) (Fig. 2) respectively, to a set of observed wind data. Likewise, FLTR (A), (B), and (C) are the analyzed values obtained by applying filters (A), (B), and (C) to the same set of data.

The pressure variability is defined in the same manner as for the winds except that a base condition is applied using the mean tropical atmosphere. That is,

$$\text{VARIB P1} = [\text{BFLTR (D)}]/[\bar{H}_T - \bar{H}_U - \text{FLTR (A)}] \quad (21)$$

$$\text{VARIB P2} = [\text{BFLTR (E)}]/[\bar{H}_T - \bar{H}_U - \text{FLTR (B)}] \quad (22)$$

and

$$\text{VARIB P3} = [\text{BFLTR (F)}]/[\bar{H}_T - \bar{H}_U - \text{FLTR (C)}] \quad (23)$$

where BFLTR and FLTR are defined as above except that the data are 'D' values, $\overline{H}_T$ is the height of the pressure surface in the mean tropical atmosphere from which the 'D' value is obtained (reference level), and $\overline{H}_U$ is the height of that same pressure surface in the U.S. standard atmosphere. This factor is required because the 'D' value is defined as the height deviation of the pressure surface from the height of that same pressure surface in the U.S. standard atmosphere.

The temperature variability is also defined, through use of a base condition determined from the mean tropical atmosphere, i.e.,

$$\text{VARIB T1} = [\text{BFLTR (D)}]/[\text{FLTR (A)} - .98\text{x}\overline{T}] \quad (24)$$

$$\text{VARIB T2} = [\text{BFLTR (E)}]/[\text{FLTR (B)} - .98\text{x}\overline{T}] \quad (25)$$

and

$$\text{VARIB T3} = [\text{BFLTR (F)}]/[\text{FLTR (C)} - .98\text{x}\overline{T}] \quad (26)$$

where BFLTR and FLTR are as previously defined except that the analysis now refers to temperature and $\overline{T}$ is the mean tropical temperature for the desired reference level. The arbitrary factor of .98 was used to avoid discontinuities which arise when the deviation approaches zero. In practice, the values for FLTR and $\overline{T}$ are used in degrees absolute.

The mixing ratio variability is defined as

$$\text{VARIB M1} = [\text{BFLTR (D)}]/[\text{FLTR (A)} - \overline{M}] \quad (27)$$

$$\text{VARIB M2} = [\text{BFLTR (E)}]/[\text{FLTR (B)} - \overline{M}] \quad (28)$$

and

$$\text{VARIB M3} = [\text{BFLTR (F)}]/[\text{FLTR (C)} - \overline{M}] \quad (29)$$

where all factors are as previously defined where applied to the moisture field and $\overline{M}$ is the mixing ratio value for the specified reference level in the mean tropical atmosphere.

CHAPTER IV

ANALYSIS OF HURRICANE DEBBIE AUGUST 18, 1969

The method of analysis described in Chapter II is applied to data collected in hurricane Debbie on August 18, 1969. These data were recorded onboard the NOAA DC-6 aircraft and were processed in the manner described in Chapter II. The variables investigated are wind, temperature, moisture, and pressure. The data are assumed to be collected instantaneously on a given pass. In actuality, the time required for the aircraft to make a single pass through the storm is approximately 20 to 30 min. These data are then averaged over small space and time intervals for insertion into the analysis equations. The grid interval chosen for the analysis was 1 n mi.

Kinetic Energy

The application of filters "A", "B", and "C" show large changes in the kinetic energy during the seeding experiment. The sequence of profiles shown in Fig. 8 are for prior to seeding, immediately after the third seeding run, and finally, some four hrs after the final seeding for left and right sides of the storm. These profiles exhibit a large decrease in the maximum value of the kinetic energy for the sum of all wavelengths represented. This total decrease amounted to approximately 40 percent for each filtered quantity for the northeast or right side of the storm. The left side showed a net decrease of 31 and 18 percent for the kinetic energy in the wavelengths represented by "A" and "B" respectively, but a net increase of 9 percent for those wavelengths associated with filter "C". The southwest or left side of the storm also shows an increase in kinetic energy with time for larger radial distances from the storm center. The profiles of kinetic energy associated with these same filters for the northwest and southeast quadrants are shown in Fig. 9. The changes for the southeast quadrant ranged from 25 to 38 percent decreases for the three filtered quantities (Table 1) while a 15 percent decrease for filter "A", 4 percent for filter "B", and a 14 percent increase for filter "C" are shown for the northwest quadrant.

Of particular interest is that approximately two-thirds of the total change, which was to occur in the longer wavelengths (Filter "C"), has occurred by the time of the third seeding except for the southeast quadrant. The net change of kinetic energy for this same time period associated with filters "A" and "B" was considerably less. In fact, the change in specific kinetic energy associated with filters "A", "B" and "C" for this time period were approximately 300, 500 and 650 knots squared, respectively, for the right side of the storm. These results indicate that an enhancement of the small scale features was occurring during the period of the decrease in the longer wavelengths since filter "A" contains filter "B" and filter "B" contains filter "C".

The kinetic energy associated with the cumulonimbus scale (band filter "D") indicates that the southwest and northwest quadrants were the most active for this scale throughout the period of the experiment (Figs. 10 and 11). There seemed to be no large changes in this quantity through the time of the third seeding, except for some enhancement in the southeast quadrant. However, a significant decrease then occurred, reaching a minimum of activity near 0200 GMT on August 19. An increase is then noted through the end of the monitoring period. This scale also seemed to be quite active along the axis of storm movement (northwest and southeast quadrants) again reaching a minimum of activity near 0200 GMT on August 19 (Fig. 11). It is also interesting to note that the most active region for this scale was in the area immediately downstream from the seeding area (northwest and southwest quadrants) while the least active areas were behind and to the right of the storm center. However, it should be pointed out that these areas behind and to the right of the storm center were quite active prior to the first seeding and the degree of activity did not change markedly until the time of the third seeding.

The response for the intermediate wavelengths (approximately rainband scale) indicates an increase in the northeast quadrant through the time of the third seeding and then a considerable dampening for all quadrants (Figs. 12 and 13) through the end of the monitoring period. Again, prior to the time of this general decrease, the most active areas for these scales were ahead and to the left of the storm center (northwest and southwest quadrants).

The response associated with the slightly longer wavelengths, (approximately eyewall scale) shows increases in nearly all quadrants prior to the third seeding (Figs. 14 and 15). Also, the decrease in the eye diameter during this period is noted which agrees with the radar structure as depicted in Black ét al. (1970). Probably the most significant feature of these two figures is the dramatic decrease in the eyewall response after the third seeding. This response is almost nonexistent near the end of the monitoring period. It should also be noted that the kinetic energy associated with this scale is generally twice as large as for the intermediate (rainband) scale and more than an order of magnitude larger than for the cumulonimbus scale.

The variability of the wind associated with the cumulonimbus scale (VARIB W1) is shown in Fig. 16. Prior to seeding, the maximum values of this variability outside of the eyewall region was approximately 0.05. This value more than doubled through the early portion of the seeding runs on the southwest side of the storm center and remained nearly unchanged on the northeast quadrant. The horizontal variation of the wind in the southwest quadrant reached a minimum after the final seeding run, but appeared to be on the increase by the time of the final monitoring pass.

The wind variability associated with the rainband scale (VARIB W2) is shown in Fig. 17. The peak values outside the eye on the left side of the storm prior to seeding ranged from 0.3 to 0.45. Near the time of the third seeding run, these values had decreased by some 30 to 40 percent. During the same period, the values on the right side increased by 30 to 40 percent. The values became somewhat unsettled during the period between the third and fourth seeding which was followed by a general reduction in the values for both sides of the storm. The peak values outside the eye for the final monitoring pass were approximately 0.1 as compared to the 0.3 to 0.4 value prior to the seeding events.

The eyewall scale wind variability (Fig. 18), showed little change through the time of the third seeding run. However, the peak value outside the eye on the southwest side of the storm showed a 50 percent reduction by the end of the monitoring period. The peak value on the northeast side showed little change during the experiment except that it was located some 5 n mi closer to the storm center near the end of the monitoring period.

Pressure

The filtered "D" values show little change in the large scale features of the pressure field during the period of the modification experiment (Fig. 19). The profiles resulting from application of filters "A" and "B" indicate a significant reduction in the pressure gradient on the southwest side of the storm during the experiment. The pressure profile for the northeast or right side of the storm indicated little change during this same period. The minimum value obtained from all three filters indicate a small decrease in pressure during the seeding, but the value recorded approximately four hrs after the final seeding period was nearly identical to that recorded prior to any seeding.

Many of the small scale features which were almost totally masked by the large scale features shown in the previous figure are readily observed in Fig. 20. These cumulonimbus scale features exhibit a large horizontal variability in time and space. However, the dominant feature in this time sequence of profiles appears to be how the magnitude of these band filtered "D" values decreased by the end of the seeding period. This reduction averaged more than 50 percent over the horizontal distance depicted in these profiles.

The band filtered 'D' value profiles for the "rainband scale" also exhibited this reduction in pressure gradient, especially on the left or southwest side of the storm (Fig. 21). Again, the magnitude of these values decreased by as much as 50 percent, with almost none of the change taking place prior to the time of the third seeding run.

The band filtered 'D' value for the "eyewall scale" (50n mi) shows a net reduction in the minimum value and the maximum value on the left side of the storm (Fig. 21). However, the right side showed an increase maximum value and gradient. In contrast to the results obtained for the cumulonimbus and rainband scales, most of the net change occurred prior to the time of the third seeding run.

The pressure variability associated with the cumulonimbus scale (VARIB P1) seemed to be largest prior to the first seeding run (Fig. 22). However, the most apparent change did not take place until after the third seeding period. This variability then remained small for the remainder of the monitoring period, averaging about 1/4 of the value determined for the period monitored prior to the first seeding event.

The pressure variability for the "rainband scale" (VARIB P2) (Fig. 23) exhibited nearly the same characteristics observed for the cumulonimbus scale. However, the final monitoring run showed less horizontal variation, but the magnitude of this variability, exclusive of the eye region increased markedly over that shown for the period one hour earlier.

Figure 24 shows the pressure variability associated with the "eyewall scale". A reduction in the magnitude of this variability is shown to have occurred in the left and central portion of the storm during the seeding operation. However, the region beyond approximately 30n mi on the right side of the storm showed an increase during this same period. It is significant to note that most of these changes occurred prior to the time of the third seeding run.

Temperature

The filtered temperature profiles (Fig. 25) show a net reduction in the maximum temperatures from prior to seeding until four hrs after the final seeding. Also shown in a significant change in the temperature field on the southwest side of the storm from prior to seeding until after the third seeding (1313 GMT to 1825 GMT). However, the temperature field showed little change on the northeast side for the same period of time. By the end of the seeding operation, the thermal structure on the southwest side of the storm had returned to a state similar to that observed prior to the first seeding event (except for the eye and eyewall region). However, a significant change had taken place on the northeast side of the storm where the temperature had increased by approximately 2 C in the outer regions after the third seeding. This change occurred in the longer wavelengths as is evidenced by the fact that nearly the same change is shown for the values obtained by application of filter "C" as compared to that obtained from filter "A". It is also observed that most of the temperature reduction with time observed over the central region occurred in the shorter wavelengths.

The time sequence of temperature profiles obtained by application of band filter "D" (cumulonimbus scale), indicates a significant reduction in the magnitude of these values after the third seeding event (Fig. 26). This of course corresponds favorably to the same feature observed in the pressure profiles. The range of these values before the first seeding until after the third seeding was approximately ± 1 C. The last two profiles shown for this day and location showed maximum values to generally be less than ± 5 C. Again as was the case for the pressure profiles, the southwest side appeared to be more active than the right side of the storm for this scale of motion.

The rainband scale (band filter "E") temperature profiles showed maximum values to be about 1.5 times larger than those associated with the cumulus scale (Fig. 27). Of particular significance again is the reduction in the amplitude of the temperature profile that occurred during the period of the modification experiment. The eyewall scale (band filter "F") temperature profiles also indicated a reduction in amplitude to have occurred with time. Of particular interest is the reduction in the temperature gradient in the eyewall region (approximately 15 to 30 n mi from the storm center) for this scale of motion. Also, it should be noted that the temperature reduction over the central region exceeded 1 C for this scale indicating that the reduction of temperature noted over the central regions in Fig. 25 was primarily concentrated in the eyewall scale.

The cumulonimbus scale temperature variability (VARIB T1) seemed to increase slightly up through the time of the third seeding and then decrease markedly as was noted for the pressure profiles (Fig. 28). This reduction generally exceeded 50 percent. Again, the southwest side, in general appeared to be more active than the northeast side. The northeast side was quite active at times and even surpassed the southwest side near the end of the monitoring period. The sensitivity of this parameter is readily observed in the large variations over short time and space intervals. As one would expect, the temperature variability for the rainband scale (VARIB T2) appears to be more conservative (Fig. 29). The same trend is noted for this scale as for the cumulonimbus scale, in that the value of the parameter seemed to increase during the early seeding periods and then decrease markedly after the third seeding event where the average value decreased by 30-40 percent. The eyewall scale temperature variability (VARIB T3) exhibited the most dramatic change of these three temperature variability parameters (Fig. 30). Reductions in the maximum value of this parameter of 57, 37 and 52 percent for the southwest central and northeast portions of the storm, respectively, were observed during the monitoring period. As was noted for the previous parameters, most of this change took place after the time of the third seeding event.

Moisture

The eye and eyewall region were quite prominent in the moisture field prior to the first seeding run as illustrated in Fig. 31 (filter "A"). That is, the eyewall region showed a relative maximum moisture content with a distinct minimum region present over the interior portion of the eye. These features remained prominent throughout the time of the third seeding. However, the region of maximum mixing ratio on the northeast side of the storm had started to enlarge by 1825 GMT and the moisture gradient had decreased. The prominent regions of maximum values associated with the eyewall at 1313 GMT had nearly disappeared by 0157 GMT on August 19 (filter "A"). The maximum moisture values continued to be located on the right side of the storm, but the moisture had been diffused over a much larger area. The moisture profiles associated with filters "B" and "C" also indicate a considerable increase in moisture for the entire area monitored. This increase seemed to be concentrated in the longer wavelength features with average values rising by 1 to 1.5 grams per kilogram over the entire area within 50 nmi of the storm center. Also of interest is that a significant portion of this increase had occurred prior to the time of the third seeding, especially in the outer regions monitored. However, as was the case for other parameters, the greatest portion of this change took place after the third seeding event.

The cumulonimbus scale (band filter "D") mixing ratio field (Fig. 32) did not exhibit the major reduction in amplitude with time that was noted for the previously discussed parameters. However, there were a few points where a significant reduction in the extreme values were noted, particularly on the southwest side of the storm. The most prominent of these areas is the one located between 10 and 20 n mi left of the storm center which persisted as an identifiable feature through more than the first 6 hrs of the monitoring period. The rainband scale (band filter "E") mixing ratio profiles (Fig. 33) showed a major decrease in the magnitude of the values during the monitoring period, particularly on the southwest side of the storm. The resulting values were less than 0.5 grams per kilogram by the end of the monitoring period for this area. Most of this change took place after the time of the third seeding run. The northeast section did not show as large a net change, but in contrast to the southwest side, a major reduction had occurred by the time of the intermediate pass shown and the magnitude of the values appeared to be on the increase by the end of the monitoring period. The larger scale features (band filter "F") exhibited nearly the same features as for the rainband scale (Fig. 33). However, the values for the northeast side apparently continued to decrease through the end of the monitoring period.

The mixing ratio variability for the cumulonimbus scale (VARIB M1) showed maximum values located on the southwest side prior to the first seeding (Fig. 34). The magnitude of the variability on the right side of the storm was about one half of that for the left side through the first 6 or 7 hrs of the monitoring period. These values generally decreased by about 40 percent through the seeding period and then increased to values as large as were observed on the first two monitoring passes. At the same time, the values on the east side decreased during the early seeding runs and then remained relatively steady through the end of the monitoring period. The net result was that moisture variability was nearly the same for both sides of the storm at the end of the monitoring period. The rainband scale (VARIB M2) mixing ratio variability exhibited similar characteristics (Fig. 35). The maximum values of this parameter were largest on the southwest side at the beginning, decreased during the seeding operations, and were approximately equal to those computed for the northeast side of the storm at the end of the monitoring period. The total reduction in the peak value was more than 50 percent.

The largest net change in the mixing ratio variability occurred in the longer wavelengths (Fig. 36). The mixing ratio variability associated with the eyewall scale (VARIB M3) decreased by 73 percent for the southwest side of the storm and 57 percent for the northeast side. Also the character of this variability changed with the horizontal variations being considerably less by the end of the monitoring period as compared to the earlier passes.

Comparison of Analysis Results with Seeding Hypotheses I and II

Seeding Hypothesis I is rather vague and difficult to evaluate in terms of the data collected. Also, the experiment as conducted was not exactly as proposed in seeding Hypothesis I. That is, the seeding was not confined to the eyewall region but extended some distance outward from the eyewall. No direct measurements were made of the change in the supercooled water to ice ratio in the seeded regions of hurricane Debbie. However, temperature, wind and pressure measurements were made which give an indication of what probably occurred in the areas of supercooled water.

This hypothesis basically suggests that a reduction in the maximum temperature and pressure gradients should result along with a corresponding reduction in the maximum wind speeds. These conditions were all observed to have occurred in the analysis previously discussed. However, other changes took place which do not correspond favorably with Hypothesis I. Primary among these changes is that the reduction in temperature gradients was to be the result of increasing the temperature on the exterior edge of the maximum temperature gradient. In actuality, this reduction in temperature gradient was more a result of the decrease in temperatures over the central region whereas the temperature in the maximum wind speed region showed only small net changes from prior to the first seeding run until after the final monitoring pass through the storm during the experiment.

Seeding Hypothesis II is more explicit and the experiment as carried out in hurricane Debbie conformed much more to the procedure proposed by Hypothesis II than Hypothesis I. Hypothesis II calls for stimulating convection at radii from the region of maximum wind speeds outward. This region of increased convection would compete with the eyewall region for the inflowing air at low levels. The result would be a reduction in the prominence of the eyewall region, reduced temperature and pressure gradients in the eyewall region and a resulting decrease in the maximum wind speeds. The results of the experiment in hurricane Debbie on August 18, 1969 strongly suggest that all of these events occurred at least through the period of the first three seeding runs. That is, the reduction in temperature over the central region and slight increases at larger radii indicate some portion of the inflowing air at low levels that would normally serve to drive the storms transverse circulation through the eyewall region was being intercepted at larger radii. Also, there was some evidence of increased convection during the early portion of the seeding operation. After the time of the third seeding, the small and intermediate scale features become much more diffuse, indicating a possible merging of the smaller scale features.

The large reduction in the large-scale feature which occurred on August 18, 1969 in hurricane Debbie was not predicted by either Hypothesis I or II. In fact calculations of the decrease in maximum winds to be expected from the seeding experiment were of the order of 10 to 15 percent. These results imply that the seeding effects were being superimposed on a large scale change that was occurring naturally.

CHAPTER V

ANALYSIS OF HURRICANE DEBBIE AUGUST 20, 1969

The method of analysis described in Chapter II is applied to data collected in hurricane Debbie on August 20, 1969. This is the scheme used in the previous chapter and the same parameters are investigated. The same form of data is used for Chapter IV except that these data were collected on August 20, 1969. More data were obtained during the August 20 operation than during the August 18 experiment and the seeding operation began approximately two hrs earlier than on the 18th. These differences were primarily a result of the fact that the storm was nearer the base of operations on August 20 as compared to that on August 18 (Fig. 1).

Kinetic Energy

The kinetic energy profiles obtained by applying filters "A", "B" and "C" to the observed data are shown in Figs. 37 and 38. The double maxima structure is quite evident in the profiles in all quadrants obtained prior to the seeding runs by application of filter "A". This double structure was reduced considerably by the time of the intermediate pass and had disappeared by the time of the final profile shown for each quadrant. Also quite evident is that the radius of these maxima in the northeast and southwest quadrant had increased by more than 10 n mi between

1140 GMT and 1700 GMT and then decreased slightly by the time of the pass at 0210 on August 21. The change in the location of these maxima was not nearly as great for the northwest and southeast quadrants.

The kinetic energy increased significantly in the northeast and southwest quadrants during the period from 1140 GMT (prior to seeding) to 1700 GMT (after the third seeding) as indicated in Fig. 40 and Table 2. This increase was 20.59 and 5.48 percent for the southwest and northeast quadrants,respectively, for filter "A", 23.28 and 23.93 percent for filter "B", and 12.34 and 15.54 percent for filter "C". The change in the southeast and northwest quadrants for this period were considerably less. However, the increase in the northwest quadrant was significant, being 4.18, 15.23, and 10.86 percent for filters "A", "B", and "C" respectively. This set of numbers indicates that most of this change was taking place in the longer and intermediate wavelengths since filter "A" contains filter "B" and filter "B" contains filter "C". A major decrease of approximately 20 percent and 10 to 12 percent occurred between 1700 GMT August 20 and 0210 GMT August 21 for all three filtered quantities in the northeast and southwest quadrants respectively. The net result was an overall decrease in the northeast quadrant of 14, 1, and 9 percent for filters "A", "B" and "C" respectively while a net increase of 6, 8, and 2 percent for the same respective filtered quantities was noted for the southwest quadrant. There was a general reduction in the rear (southeast) portions of the storm and an increase in the front (northwest) portions. The rate of increase was much larger during the period from 0955 GMT to 1445 GMT than from 1445 GMT until 2311 GMT. Also of particular interest is that the kinetic energy increased at larger radial distances from the storm center in two quadrants (northwest and southwest) and the same trend appeared to be taking place in the northeast quadrant.

The kinetic energy profiles associated with the cumulonimbus scale (bandfilter "D") are shown in Figs. 39 and 40. This scale seemed to show a considerable enhancement in the northeast quadrant almost immediately after the first seeding run (1155-1237 GMT). The pass which was made just after the second seeding run was along the direction of motion. The response for this scale increased considerably in the northwest quadrant (1428-1456). A similar sequence of events is noted for the northeast quadrant after the third seeding. During this same period, the level of activity for this scale seemed to be on the increase in the southwest quadrant. This activity reached its peak near the end of the seeding period, and then subsided through the end of the monitoring period. The level of activity for this scale in the northeast quadrant apparently reached its peak earlier and then decreased nearly through the end of the monitoring period. However, the final two passes through this area which occurred some five to six hrs after the final seeding run indicated that the level of activity was increasing. These same profiles for the northwest and southeast quadrants for the period of some three to four hrs after the final seeding period indicated a high level of activity in the southeast quadrant for this scale with almost no response in the northwest quadrant.

The kinetic energy profiles associated with the rainband scale (band filter "E") show the maximum value in all quadrants decreasing through most of the seeding period (Figs. 41 and 42). This decline seemed to be quite steady through the first six hrs of the operation, fluctuated somewhat during the period between the fourth and fifth seeding events and then decreased again through the end of the monitoring period. The value of the maximum kinetic energy outside the eye decreased by approximately 72, 69, 50 and 14 percent for the northeast, southwest, northwest, and southeast quadrants respectively for the period from prior to seeding until the final monitoring passes were made through these quadrants, well after the final seeding event.

The kinetic energy profiles associated with the eyewall scale of motion (band filter "F") are shown in Figs. 43 and 44. Prior to the time of the first seeding, the maximum kinetic energy outside the eye was relatively low. In fact, these values were only about one half of what were observed on August 18 (Fig. 14). These values fluctuated considerably, but generally increased through the period of the fourth seeding and then decreased. The final result was that these values at the end of the monitoring period were nearly the same as those obtained prior to the first seeding run.

The wind speed variability profiles for approximate cumulonimbus scale motion (VARIB W1) shows a considerable increase in the northeast quadrant, just after the first seeding run (Fig. 45). This response level then decreased during the period after the seeding. (Compare the pass for 1155 to 1235 GMT with that for 1240 to 1308 GMT.) The next two monitoring passes through this region occurred just prior to and shortly after the third seeding period. Again, the significant increase is noted after the seeding for the northeast quadrant. A similar sequence of events is noted for the period surrounding the fourth seeding event (~1800 GMT) in the northeast quadrant. The peak response in the southeast quadrant occurred approximately one and one half hrs after the fourth seeding. The peak value (exclusive of the central region) was located at a radial distance of approximately 30 n mi from the storm center. It would take approximately one and one half hrs to carry the seeding agent to this area from its point of release if it remained suspended in the tangential flow at the proper levels.

The wind speed variability profiles for approximate rainband scale motion (VARIB W2) are shown in Fig. 46. The magnitude of this variability outside the eye increased considerably in the northeast quadrant after the first seeding run. It is interesting to note that this variability continued to increase through the one hour period after this seeding run whereas the cumulonimbus scale variability tended to show a decrease near the end of this same period. This rainband scale variability had subsided considerably just prior to the third seeding period, and then showed a dramatic increase (~300 percent increase). The wind speed variability for the rainband scale was also on the increase in the southwest quadrant during this same period. The wind speed variability continued to increase on both the right and left (NE-SW) sides of the storm, reaching a maximum near the end of the seeding period and then subsided. The two profiles obtained at the end of the monitoring period were quite similar in maximum magnitudes to those recorded prior to the first seeding event.

The wind speed variability profiles for eyewall scale motion (VARIB W3) indicate little net change in the magnitude of the response for the three passes shown in Fig. 47. These profiles are again for the period prior to seeding (1140 GMT), after the third seeding (1700 GMT), and at the end of the monitoring period (21/0210 GMT). Although there was little change in the magnitudes of the peak values, there was a distinct shift outward in the location of these maxima regions indicating an expansion of the eye diameter between 1140 and 1700 GMT. A shift inward then occurred, but the final location of these peak values was approximately 5 n mi farther from the storm center than for the period prior to the first seeding.

Pressure

The minimum value of the filtered "D" values shows an increase occurred between the time of the third seeding and the final monitoring pass of the day (Fig. 46). Approximately one half of this increase took place in the long wavelengths with most of the remainder occurring in the rainband to eyewall scale of motion. Although the central pressure was steady through the first six hrs of the experiment for the sum of the long and intermediate wavelengths (filters "A" and "B"), a decrease is noted for the long wavelength features (filter "C"). This of course implies that an increase in pressure must have occurred in the intermediate wavelengths.

The cumulonimbus scale "D" value profiles (band filter "D") generally show an increase in the magnitude of the horizontal variations after the first seeding (Fig. 49). This parameter generally remained quite active through the seeding period and then dampened considerably by the end of the monitoring period. The maximum values at the end of the monitoring period were approximately 50 percent smaller than those generally observed during the seeding operation.

The rainband scale "D" value profiles (band filter "E") show a distinct decrease in the pressure gradients particularly in the eyewall region (Fig. 50). Most of this pressure change occurred before the fourth seeding period. However, the final profile shown is much smoother than either of the two recorded earlier. Also, the maximum amplitude of the curve obtained on the last monitoring pass is 40 percent smaller than that recorded prior to seeding.

The eyewall scale D value profiles (band filter "F") also exhibit the decrease in amplitude and the pressure gradient in the eyewall region during the seeding operation. Again, a major portion of this change took place before the fourth seeding, but a significant amount of this change occurred between the time of the fourth seeding and the final monitoring pass.

The cumulonimbus scale pressure variability profile (VARIB P1) are shown in Fig. 51. No major change in the magnitudes of this parameter occurred during most of the seeding period, except at a few isolated points. However, a general dampening is noted near the end of the seeding period until the final monitoring pass. In fact, the average magnitude of this parameter within 30 n mi of the storm center is approximately one half of that recorded prior to the first seeding period.

The rainband scale pressure variability profiles (VARIB P2) are shown in Fig. 52. Although there are considerable horizontal and time variations of this parameter, it is difficult to determine any significant trends. The average amplitude of the profiles remains nearly the same through most of the monitoring period except for a few select points. The eyewall scale pressure variability profiles (VARIB P3), however exhibit distinct changes (Fig. 53). The magnitude of this parameter decreased by about 14 percent, with little net change taking place in the northeast quadrant during the monitoring period.

Temperature

The filtered temperature profiles (Fig. 54) show that a large change occurred during the seeding operation. The maximum temperature observed in the central regions of the storm shows a steady decrease with time, especially for the short and intermediate wavelengths (filters "A" and "B"). However, the major portion of the reduction which occurred in the longer wavelengths (filter "C") came after the time of the third seeding. This reduction of temperature in the longer wavelengths during the latter portion of the monitoring period accounts for most of the change in maximum temperature depicted in the illustrations for filters "A" and "B". These results imply that a possible sequence of events occurred where the changes first occurred in the shorter wavelength features and then progressed through the longer wavelengths. Also of particular interest in this set of profiles is the reduction of temperature gradient particularly in the eyewall region on the northeast side which occurred during the monitoring period. This feature is evident for all three filter results. Also, the temperature profiles became smoother during the experiment as illustrated by the disappearance of the secondary temperature maximum located on the northeast side of the storm. During this same time interval, the temperature increased in the outer regions of the storm covered by the monitoring pattern.

The time sequence of temperature profiles representing the cumulonimbus scale (band filter "D") indicates that a considerable reduction in the maximum value occurred during the monitoring period (Fig. 55). In fact the maximum amplitude of the curves for the temperatures recorded at the end of the monitoring period was less than one half of that observed prior to the first seeding. The largest portion of this reduction appears to have occurred during the early portion of the monitoring period. The northeast and southwest sides of the storm appeared to be about equally active for this scale of motion during most of the monitoring period. However, there was the general trend of the maximum values which decreased through most of the period of the experiment.

The temperature profiles representing the rainband scale (band filter "E") also showed a considerable reduction in amplitude to have occurred during the period of the experiment (Fig. 56). Most of this change occurred prior to the time of the fourth seeding event. The reduction in the temperature gradient for this scale of motion was quite large, particularly in the northeast quadrant. The eyewall scale temperature profiles (band filter "F") indicated this same general trend (Fig. 56). The central value decreased by 2 C during the monitoring period with 3/4 of this change taking place prior to the time of the fourth seeding. During the same period, the minimum temperatures increased by approximately 1 C. These two changes resulted in a major reduction of the temperature gradient.

The cumulonimbus scale temperature variability profiles (VARIB T1) for the left and right sides of the storm (SW-NE) are shown in Fig. 57. The maximum magnitudes of this parameter fluctuated considerably during the seeding operation. The peak values on the southwest side of the storm increased in magnitude significantly during the first five or six hours of the monitoring period. These peak values then decreased slowly through the end of the monitoring period. The values recorded for the final two monitoring passes through this area averaged 25 to 50 percent less than those observed near the time of the third and fourth seedings. The peak values for the northeast side of the storm followed this same general trend, except that the maximum values were recorded near the time of the first seeding run and decreased through the end of the monitoring period.

The rainband scale temperature variability profiles (VARIB T2) depicted in Fig. 58 show large horizontal and time variations. The maximum values of this parameter were observed prior to the time of the fourth seeding. These values then decreased and the maximum values recorded near the end of the monitoring period averaged some 20 to 50 percent less than that recorded prior to the first seeding event.

The temperature variability profiles for the eyewall scale (VARIB T3) are shown in Fig. 59. A significant reduction in the maximum values for this variable had occurred in the southwest and central portions of the storm prior to the time of the fourth seeding event. During the same period the double maxima located on the northeast side of the storm was replaced by a single peak. The total reduction of the peak values of the temperature variability for the period of the monitoring missions was approximately 41, 30, and 25 percent, respectively, for the southwest, central and northeast portions of the storm, respectively.

Moisture

The double eye structure present during the early portions of the modification experiment in hurricane Debbie on August 20, 1969 is quite evident in the moisture field analysis for this time and data (Fig. 60), This feature was present prior to the first seeding ($\sim$1140 GMT), but had become considerable less distinct by 1700 GMT. However, some semblance of this structure remained throughout the monitoring period, especially in that obtained by application of filter "A". Also of considerable interest is that the minimum central value increased during the period of the experiment. This feature is quite prominent in both of the sets of profiles obtained through use of filters "A" and "B". During this same period, the total amount of moisture was increasing over the central and southwestern portions of the storm. This was especially true for the longer wavelengths, where the value increased by approximately 1.0 to 1.5 gm/kg.

The cumulonimbus scale mixing ratio profiles (band filter "D") show a trend toward a slight decrease with the passing of time after the first seeding period (Fig. 61). The minimum average amplitude was recorded some 4 to 5 hrs after the final seeding event and then increased amplitudes are noted for the final two passes through the area at the end of the monitoring period.

The mixing ratio profiles associated with the rainband scale (band filter "E") are depicted in Fig. 62. The average amplitude of the profile for 21/0210 GMT was approximately 1/2 that recorded prior to the first seeding event. The eyewall scale mixing ratio profiles (band filter "F") show a trend toward less horizontal variations, particularly over the central regions, which occurred during the period of the experiment. The minimum central value increased by approximately 2 gm/kg during this period while the value in the eyewall remained nearly constant.

The cumulonimbus scale mixing ratio variability profiles (VARIB M1) show very little change in the average amplitude during the experiment (Fig. 63). Local changes are observed, but it is difficult to associate them with a particular event. The mixing ratio variability profiles associated with rainband scale motion (VARIB M2) showed a decrease in the average amplitude which occurred during the monitoring period (Fig. 64). The average values obtained some 3 to 5 hours after the final seeding event were approximately 10 to 20 percent smaller than those observed during the early portion of the monitoring period. The eyewall scale mixing ratio variability profiles (VARIB M3) show an average amplitude reduction of 20 to 30 percent to have occurred over the central and southwest portions of the storm during the period of the modification attempts (Fig. 65). This reduction reflects the trend toward smoother profiles which was depicted earlier (Fig. 60).

Comparison of Analysis Results with Seeding Hypotheses I and II

The changes that occurred in hurricane Debbie in the cumulonimbus and intermediate (rainband and eyewall) scales of motion on August 20, 1969 were quite similar to those which occurred on August 18, 1969. However, the large scale changes were quite different. Apparently, any seeding effects taking place were being superimposed on a large scale increase in storm intensity, particularly during the first half of the seeding experiment period.

The seeding experiment conducted on August 20, 1969 was identical to that for August 18, 1969. That is, it was quite similar to that proposed under Hypothesis II and different from that suggested by Hypothesis I. The net results indicate that temperatures decreased in the central region and increased in the outer regions, offering considerable support for Hypothesis II. That is, there is a strong indication that the low level flow was being intercepted at larger radii and that the convective activity increased at these locations during the early seeding periods and competed with the eyewall region for the low level flow. The prominence of the eyewall structure decreased during the experiment. This feature was particularly evident in the moisture field analyses. The net result was smoothing oof the intermediate scale features in the pressure, temperature, and moisture fields, particularly after the time of the third or fourth seeding period. Again, these data do not offer much support to Hypothesis I since the temperature gradient reduction in the eyewall region was primarily the result of a decrease in temperature over the central region and an increase at larger radii rather than in the immediate eyewall area.

CHAPTER VI

GRADIENT WIND ANALYSIS OF HURRICANE DEBBIE

The gradient wind model developed in Chapter III and Appendix A is applied to the observed wind and pressure fields. The analyzed data are presented in two forms. The first is in nondimensional scaled component; this shows the contribution from each term contained in the gradient wind equation. The second is in the form of the filtered relative winds (relative to the moving storm center) and the gradient wind computed from the filtered pressure field. There are also two sub-groups of analyses presented for each of the storms mentioned above. The first was obtained by applying equal weight to the relative wind and pressure fields and zero weight to the gradient wind constraint. That is, the wind and pressure fields were filtered simultaneously and each were assumed to be equally accurate. If the measurements of one parameter was believed to be less reliable than the other, then more weight would have been placed on the terms containing the more reliable measurements.

A base condition was obtained by use of zero weight on the gradient wind constraint. That is, we would like to determine what parts of the storm meet the gradient wind conditions for selected degrees of filtering. In the cases presented, filters "A" and "B" were chosen. As was mentioned previously, the wind and pressure fields were filtered simultaneously through the use of analysis equations (16) and (17). The results from application of filter "C" are not presented as they contain only the long wavelength features and deviate considerably from the gradient wind condition.

The second sub-group was also obtained by use of analysis equations (16) and (17). However, in this case, the gradient wind constraint was assigned a weight ≥ 100 times that placed on the low pass filtering terms. This of course causes the analysis to approach the gradient wind condition. Profiles of the resulting wind field along with the gradient wind computed from the resulting pressure field are presented. In this manner, we can determine where or if the gradient wind equation is applicable in the hurricane where information has been obtained from both the observed D values and the observed wind field. This becomes very useful when developing simple hurricane models or when attempting to fill in missing data areas when either the pressure or wind measurements are missing.

Hurricane Debbie August 18, 1969

The series of profiles shown in Fig. 66 are for the periods prior to the first seeding, after the third seeding, and approximately 4 hours after the final seeding. Filter "A" removed most of the high frequency components and some cumulus scale motion. However, some relatively large horizontal pressure gradient variations continue to exist. These variations were much greater when only the components with wavelengths less than two n mi were removed (not illustrated). The response profiles for the centrifugal and the coriolis terms are much smoother, reflecting the effect of the radial distance factor in the centrifugal term and the constant coriolis parameter. The contribution from the coriolis term is an order of magnitude smaller than the other two terms over the high energy portion of the storm. The primary effect that the gradient wind constraint has on the response of these three components is to smooth out the pressure gradient profile. The other two profiles only undergo minor changes.

The pressure gradient profile, particularly on the southwest side of the storm underwent a major change during the monitoring period. This quantity showed its largest horizontal variations during the actual seeding period (~1825) and the least some 4 hrs after the final seeding event. That is, the analysis with the gradient wind constraint deviated most from that without the gradient wind constraint during the seeding period and least at the end of the monitoring period.

The wind profiles in Fig. 67 correspond to the analyses indicated in Fig. 66. The profiles shown in panels A through C and D through F of Fig. 67 were obtained from the analysis represented by the solid and dashed lines respectively in Fig. 66. The relative wind profiles resulted directly from the analysis while the gradient wind was computed from the pressure profiles obtained in the analysis. By comparing these sets of profiles, we can determine how well the analyzed pressure and wind fields approximate the gradient wind condition.

Panels A, B, and C of Fig. 67 illustrate the analysis results which exclude the gradient wind constraint. It is rather obvious that in generally, the gradient wind condition is not satisfied by the results obtained by application of filter "A" to the observed wind and pressure fields. Also of considerable interest is the fact that the pressure field shows a distinct trend toward satisfying the gradient wind condition during the monitoring period. That is, the gradient wind computed from the analyzed pressure field at 19/0157 GMT (panel C), is a much closer approximation of the analyzed relative wind profile for that time and location than was obtained for the same two parameters at 1313 GMT (panel A).

The wind speed analyses obtained by the simultaneous applications of the gradient wind constraint and filter "A" for the same observed data described above are illustrated in D, E, and F of Fig. 67. The best agreement between the analyzed relative wind and the computed gradient wind is shown for the eyewall region at 1825 GMT. The gradient wind constraint forces an adjustment on both the pressure and wind fields in an effort to force the analysis to satisfy the gradient wind condition. The only reason that the two wind profiles are not identical is that the gradient wind condition was not totally satisfied. If this were the desired result, one would place a larger relative weight on the gradient wind constraint or derive a different set of analysis equations using Lagrange multipliers. However, in this case, we wish to determine how well the pressure and wind fields satisfy the gradient wind condition, and which must be adjusted the most to approximate this condition. As was stated earlier, the pressure and wind field measurements were assumed to be equally reliable. However, it appears that the greatest effect of including the gradient wind constraint was to adjust the pressure field beyond that imposed by filter "A". This condition is illustrated by the fact that the gradient wind profiles in upper panels of Fig. 67 differ considerably from their corresponding profiles in the lower panels.

At the same time, the relative wind speed profiles for the two analyses differ only slightly for the same time periods.

The gradient wind speed component analysis resulting from application of filter "B" with and without the gradient wind constraint is illustrated in Fig. 68. The general effect of filter "B" is to remove the cumulonimbus and smaller scale motions. This effect of this additional filtering is quite evident when comparing the results shown in Fig. 68 with those depicted in Fig. 66. Another major difference between these two sets of data is that the difference between the profiles with and without the gradient wind constraints for the centrifugal and coriolis terms is generally larger for filter "B" than for filter "A". This implies that the major effect of the gradient wind constraint was to adjust the wind speed for filter "B" and to adjust the pressure field for filter "A". The results shown in Fig. 69 also indicate the presence of this effect. For instance, the imposition of the gradient wind constraint caused the analyzed value of the wind speed to be increased by 10 kt on the southwest side of the storm at approximately 1313 GMT (Fig. 69 A and B). However, if one compares the relative wind profiles obtained by use of filters "A" and "B" with the inclusion of the gradient wind constraint (dashed lines in panels D, E, and F of Figs. 67 and 69) only small differences are noted. These results imply that the major problem with the computed gradient wind profiles without inclusion of the gradient wind constraint was in the method of evaluating the pressure gradient force over short distances. This method of course amplifies the small errors which may exist in the pressure field. Of course, as the pressure field became smoother as resulted from greater filtering imposed by the inclusion of the gradient wind constraint or greater relative weights on the low pass filter terms (filter "B") then the evaluation procedure became less critical. The combination of these results indicates that the conditions imposed on the wind and pressure fields by filter "A" more closely satisfy the gradient wind condition than those resulting from application of filter "B".

Hurricane Debbie August 20, 1969

The components of the gradient wind (Fig. 70) indicate a relatively good agreement between the profiles obtained with and without the gradient wind constraint for the three sets of profiles shown. Again, the profile of the pressure gradient shows the largest fluctuations and the general effect of the inclusion of the pressure gradient constraint is to smooth out these horizontal variations. These horizontal variations are amplified by the method of finite differencing over short space intervals that was used to obtain the gradient wind profiles shown in A, B, and C of Fig. 71. The smoothing effect of inclusion of the gradient wind constraint is shown in D, E, and F of Fig. 71. It should also be noted that the gradient wind model over estimates the wind speed over most areas outside the eye of the storm.

The gradient wind component analysis resulting from application of filter "B" shows excellent agreement between the pressure gradient profiles obtained with (dashed line) and without (solid line) inclusion of the gradient wind constraint (Fig. 72). This result indicates that the method of evaluating the difference operator is sufficiently accurate for scales of motion represented by filter "B". However, the inclusion of the gradient wind constraint results in an increase in the analyzed wind speed which is reflected by the increased values for the coriolis and centrifugal terms. This effect is further illustrated in Fig. 73. Here again, the gradient wind model tends to overestimate the actual wind speed for nearly all of the high energy portion of the storm monitored. The results obtained with inclusion of the gradient wind constraint with filter "B" indicated a larger increase in the wind speed than were obtained were filter "A". That is, the dashed line profiles for A, B, and C of Fig. 71 differ only slightly from the corresponding profiles in D, E, and F of the same figure. However, these same respective profiles illustrated in A, B, and C of Fig. 73 differ considerably from the corresponding profiles in D, E, and F of the same figure. These results indicate that the gradient wind condition is more nearly satisfied by the sum of the scales of motion represented by filter "A" than those represented by filter "B". A similar result was obtained for the data collected in hurricane Debbie on August 18, 1969.

CHAPTER VII

SUMMARY AND CONCLUSIONS

The research reported on in this paper is concerned with three basic problems. The first was to develop consistent analysis techniques that can be used to evaluate the structure and intensity of tropical storms as well as changes in the state of the storm with time. Particular attention was to be placed on the cumulonimbus, rainband, and eyewall scales of motion. Also, the techniques should provide an objective means of comparing the analyzed results from one time to another and from one storm to another where particular interest is placed on the high energy portion of the storm. The second goal was to apply these techniques to the data collected during modification experiments conducted in Hurricane Debbie on August 18 and 20 of 1969, and evaluate changes which occurred in the storm structure. Also, we wished to determine what portion of these changes could reasonably be attributed to the seeding experiments. The third goal was to use the results of the analyses of Hurricane Debbie to develop a more explicit and detailed seeding hypothesis which could be used in the statistical evaluation of future modification experiments. That is, to determine a set or sequence of events which would occur with a seeded storm but would have a low probability of occurring under natural conditions.

Evaluation of Analysis Techniques

The analysis methods used in this paper are primarily based on variational optimization techniques (Sasaki, 1958, 1968, 1969, 1970a,b,c) The first series of analyses were based on analysis equation (5) derived in Chapter III and Appendix A. This analysis equation contains an observational constraint and two low pass filter terms. By varying the relative weights on these terms, we attempted to selectively filter the recorded signal or input data observed from the airborne platform. Filtering of the data seems to be required in order to observe and study in detail the small scale motions which are often masked by the large scale features in the hurricane. Likewise, the ability to study small changes in the large scale motions is also quite important and these changes are often masked by the small scale features. The changes in the large scale occurring over the time scales covered by the seeding experiment monitoring period are generally believed to be caused by features other than the seedings. Therefore, these contributions must be separated in order to determine the immediate and short range effects of the seeding operation. This separation of scales of motion was accomplished through use of low pass and band pass filters based on Eq. (5). The end point problem which often arises in standard filtering techniques seemed to be minimal in these analyses. The degree to which we were successful in effectively separating these small scale features from the large scale system is amply illustrated in the numerous figures presented.

The variability factors developed and used are based on the filtered and band filtered data and some base condition such as the mean tropical atmosphere. These factors were defined for selected scales of motion and the standard meteorological parameters. The information extracted by use of this technique generally compliments that obtained by use of the band filters. In addition, the signal is normalized by being a function of the magnitude of the parameter being investigated. This feature allows one to make a direct comparison of the variability factor for storms of various intensities. Also, these comparisons can be made in time and space for a particular storm. This feature is of particular importance, if the character and/or magnitude of the computed factor for a particular scale is expected to change due to some natural or artificial phenomenon. The effectiveness of this analysis scheme varies, depending on the variable and scale being investigated.

The analysis equations which contained the gradient wind constraint were designed to simultaneously extract information from the observed pressure and wind fields. In this manner we could determine where, when, and for what scales of motion that the gradient wind condition was most nearly satisfied. To accomplish this task, we have computed and displayed the scales values for each of the contributing terms contained in the gradient wind equation. We found that in general, the gradient wind computed from the pressure field overestimates the wind speed for most areas of the high energy portion of the storm. It was found that the most critical step in these calculations is in the method of evaluating the pressure gradient. This is particularly critical for the signal containing the shorter wavelength features and becomes less critical as more of these high frequency components are removed from the pressure data. This fact is amply illustrated in Figs. 66 through 73where a comparison is made between the results obtained with filters "A" and "B". Also, the inclusion of the gradient wind constraint acts as additional low pass filter.

A comparison of the results for the individual components illustrated in Figs. 66 and 70 indicate that the primary effect of inclusion of the gradient wind constraint was to smooth out the response for the pressure gradient term. In contrast, the cases illustrated in Figs. 68 and 69 show that the primary effect of the inclusion of the gradient wind constraint was to increase the wind speed as reflected in the increased values for the centrifugal and coriolis terms. The reason for the difference between these two sets of figures is that filter "B" removes more of the high frequency components than does filter "A".

The results illustrated in Figs. 67, 69, 71 and 73 indicate that the gradient wind model provides a better representation of the observed wind field than does a straight forward computation of the gradient wind based upon the filtered pressure field. This is a result of two conditions. The first and most important is that information is extracted from both the pressure and wind fields and second, the errors arising from the finite difference method of evaluating the pressure gradient term is decreased by the increased filtering imposed by the gradient wind constraint. This fact is illustrated by first comparing the dashed line profiles in panels D, E, and F with the corresponding profiles in panels A, B, and C for each of the figures cited above. Next, compare the solid line profiles in panels D, E, and F with the corresponding dashed line profiles in panels A, B, and C for each of these figures. The result is that the dashed lines show a greater degree of correspondence than the solid lines of the lower panels with the dashed lines of the upper panels. That is, the wind analysis resulting from the gradient wind model (dashed lines in lower panels) provides a better representation of the filtered wind (dashed lines in the upper panels) than does the gradient wind computed from the pressure field (solid lines in lower panels) undergoing the same degree of filtering.

The results from the gradient wind model of course have not been forced to identically satisfy the gradient wind condition as is illustrated by the fact that the solid and dashed lines in the lower panels of the above mentioned figures are not identical. However, the analysis has been forced to approach this condition by placing a relatively large weight on the gradient wind constraint. The analysis could be forced even more toward the gradient wind condition by placing even a larger relative weight on the appropriate constraint, but as can be seen from the results illustrated in the lower panels of Figs. 67, 69, 71 and 73, the resulting analysis would deviate more from the corresponding relative wind profiles illustrated in the upper panels of these same figures.

The result of this set of analyses is that the gradient wind model does a relatively good job of simulating the wind speed profiles over the high energy portion of the storm. This is especially true for those scales of motion retained with the application of filter "A". This model could then be used in areas where wind speed data are missing such as sometimes happens in very heavy precipitation areas. The results for the missing data areas would be even better than those obtained from analysis equation (5) which can be viewed as somewhat of a least strain curve fitting technique, since the model extracts information from the wind and pressure fields simultaneously.

Evaluation of Hurricane Debbie (1969) Analyses

Hurricane Debbie was seeded five times on both August 18 and 20, 1969. The maximum wind speed prior to the seeding events was nearly the same for both days. However, the structure of the storm was somewhat different in that on August 18, a single eyewall structure was present (Figs. 18 and 19), while a double eyewall structure was initially present on August 20 (Figs. 37 and 38). Many of the changes which occurred prior to, during, and after the seeding events were different for the two days. However, many common features were also observed to occur during this same period.

The kinetic energy profiles shown in Figs. 8 and 9 and the percentage changes listed in Table 1 indicate that the maximum kinetic energy value decreased for all represented wavelengths from prior to seeding until the end of the monitoring missions on August 18. The net changes listed in Table 1 show that a major portion of the reduction associated with the intermediate and shorter wavelengths occurred after the period of the third seeding, while that associated with the longer wavelengths (filter "C") occurred prior to the time of the third seeding event. In fact, if one computes the change in kinetic energy from the last column in Table 1, values of -341, -479, and -640 kt^2 are obtained for filters "A", "B", and "C" respectively for the change between (1) and (2). Since filter "A" contains "B" and filter "B" contains "C", these results indicate that a major reduction was taking place in the longer wavelengths and that the intermediate and shorter wavelengths were actually enhanced during this period. However, if these same quantities are computed for the time period from (2) to (3), (after the third seeding until near the end of the monitoring period) values of -1369, -942, and -280 kt^2 are obtained for filters "A", "B", and "C", respectively. These values indicate that the long wave feature continued to decrease in intensity during this time period, but at a much slower rate than earlier. Also, the intermediate and shorter wavelength features which were enhanced prior to the time of the third seeding underwent a dramatic reduction during this time period. These characteristics are further illustrated in Figs. 10 through 15 which show a time series of band filtered kinetic energy profiles. A general enhancement is shown for most of the scales of motion represented through the time of the third seeding and then a dramatic decrease is shown through the end of the monitoring period.

The results in changes of kinetic energy obtained for August 20, 1969 show some different characteristics. The changes in kinetic energy for the last column in Table 2 are 138, 233, and 21 kt^2 for filters "A", "B", and "C" for the time period of (1) to (2) (prior to the first seeding until after the third seeding event). These results indicate an increase in kinetic energy for the sum of all the wavelengths represented. However, most of this increase was confined to features of eyewall scale or larger for this time period. The same quantities for the period of after the third seeding until the end of the monitoring period are -167, -90, and -60 kt^2 for filters "A", "B" and "C" respectively. These results imply a reduction at all wavelengths represented since the value for filter "A" is a larger negative number than for "B" and likewise the value for filter "B" is a larger negative number than for "C". These results are also illustrated in Figs. 39 through 43 where a distinct increase in the eyewall scale (Figs. 43 and 44) is noted through the periods of the first three or four seedings and then a decrease is observed. During this same period, the rainband scale (Figs. 41 and 41) appeared to be decreasing somewhat steadily through the period of the modification experiment. At the same time, the cumulonimbus scale (Figs. 39 and 40) shows an overall enhancement up through the period of the third or fourth seeding events and then a considerable decrease.

A summary of the kinetic energy analyses for these two seeding experiments indicates that on August 18, a large scale decrease occurred prior to and during most of the monitoring period which cannot reasonably be attributed to the seeding operation. Likewise, a large scale increase in intensity was taking place on August 20 during the early portion of the seeding operation. A major portion of this increase was apparently associated with the change from a double to a single eyewall structure and also could not reasonably be attributed to the seeding operation. However, a significant decrease occurred in these longer wavelength features after the time of the third or fourth seeding. In general, the results for the smaller and intermediate scale features showed some enhancement during the early portion of the seeding operations on both days, and then a distinct decrease through the end of the monitoring periods.

The analyses of the pressure fields for August 18 showed a general decrease in the pressure gradient associated with the large scale feature (Fig. 19) to occur during the seeding experiment. Most of this change took place prior to the time of the third seeding, a condition which was observed in the kinetic energy analyses. However, the minimum central pressure showed little change between the times of the first and last passes illustrated. The pressure profiles associated with cumulonimbus (Fig. 20), rainband, and eyewall (Fig. 21) scales also exhibited characteristics similar to those of the kinetic energy analyses. That is, these scales showed a general decrease in the magnitudes of their extreme values, with most of the change taking place after the time of the third seeding period.

The analyses of pressure for August 20 also shows a general decrease in the pressure gradient for the long wave features (Fig. 48) to have occurred basically after the time of the third seeding event. The cumulonimbus scale pressure profiles (Fig. 49) also indicate a reduction in the magnitudes of the extreme values near the end of the seeding operation. This reduction was not as large as was observed for the August 18 case, but it is interesting to note that the variability associated with this parameter for August 20 (Fig. 51) was initially considerably smaller than for August 18. However, the results at the end of the monitoring periods were quite similar for both days. The rainband and eyewall scales on August 20 also showed distinct pressure gradient decreases to have occurred during the seeding operation.

The temperature analyses for these same time periods exhibit characteristics almost identical to those depicted in the pressure analyses. That is, a general reduction in the temperature gradients for nearly all scales represented is noted to have occurred during the period of the modification experiment. In addition, a temperature decrease occurred over the central regions of the storm and an increase is shown to have occurred during this period in the outer regions (Figs. 25 and 54). This same feature was generally present in the corresponding pressure profiles, but is not as readily discernable due to the scale of the plotted graphs.

The moisture analyses also exhibit the same general characteristics as the pressure and temperature fields. However, in addition to these characteristics, the moisture level shows a distinct and significant increase to have occurred over most of the high energy portion of the storm during the period of the modification experiments on both days (Figs. 31 and 60). Most of this increase is associated with the longer wavelength feature. Also, the distinct dry region over the central portions of the storm which were present during the early passes became almost non-existent by the end of the monitoring period. The eyewall regions, quite distinct in the moisture analyses for the early passes, were also nearly eliminated (Figs. 33 and 62).

The following general observations can be made concerning the overall changes in structure which occurred during the seeding experiments conducted in Hurricane Debbie on August 18 and 20 of 1969. First, a general reduction in the amplitudes and gradients of most of the parameters analyzed occurred on both days for scales of motion of eyewall scale or smaller during the period of the experiments. This reduction generally occurred after the time of the third or fourth seeding, i.e., some four to six hours after the first seeding run. There appeared to be a temporary enhancement of the smaller scale features during the early portions of the seeding operation, but the evidence for this condition was generally not as strong as for the decrease for these same scales during the latter portions of the experiment periods. Also of particular interest is that the moisture level rose over most of the high energy portion of the storm and in general, the structure of the storm became more symmetrical for nearly all parameters during the modification experiments. These similarities in changes for the two seeding cases (August 18 and 20) occurred despite the fact that the long wave features were acting in opposite directions for the 18th as compared to that for August 20. These results offer strong evidence supporting the basic seeding hypothesis discussed in Chapter II of this paper. They are the basis for the more explicit hypothesis which is proposed in the next section.

Proposed Seeding Hypothesis

The hypothesis proposed in this section is basically an elaboration of Hypothesis II discussed in Chapter II. The details of this proposed hypothesis are based on the interpretation of the results obtained in the analyses described earlier and results of other seeding experiments conducted on cloud lines, individual clouds, and cloud groups. The intent is to help explain the events which may occur in a hurricane seeding operation and to propose a sequence of events which hopefully are likely to occur with a particular seeding experiment and highly unlikely to occur naturally. If successful, this hypothesis would be of considerable aid in the statistical evaluation of hurricane seeding experiments.

Hypothesis II calls for seeding from the exterior edge of the band of maximum winds radially outward for a distance of approximately 20n mi The basic idea is to enhance convection at radii greater than the eyewall. The analysis results indicate that this effect probably took place during the early portions of the seeding operations on both August 18 and 20. The sequence of events which could reasonably be expected to occur is that first, the individual towers or cells containing supercooled water would grow and this along with the fact that the seeding occurs in a somewhat continuous manner over a 20n mi interval would cause the systems to merge over this region. The fact that individual cloud systems can be caused to extend in horizontal coverage and probably merge have been amply demonstrated in Stormfury cloud line seeding operations and by Woodley (1970) and Simpson and Woodley (1971) during experiments conducted over south Florida. At the same time, the strong horizontal wind components would spread the seeding agent and its effect around the high energy portion of the storm. This widespread enhanced convection would raise the moisture levels throughout the high energy portion of the storm. At the same time, the increased ascent at larger radii than the eyewall would decrease the prominence of the eyewall by competing with the eyewall for the low level inflowing moisture laden air. The merging of the cloud systems would also decrease the prominence of the individual cumulonimbus clouds and hurricane rainbands. Each of these features was observed to have occurred in hurricane Debbie (1969) on both August 18 and 20. The time periods over which these changes took place was sometimes difficult to determine primarily because of the inability to monitor seeded areas continuously. Some areas in the immediate vicinity of the seeded areas were monitored shortly after seeding and there apparently was nearly instantaneous reaction to the seeding. Of course, the number of such cases are few and it is difficult to state with a large degree of confidence that this short term change was directly related to the seeding event. However, an almost instantaneous reaction to seeding agents has been observed in Stormfury cloudline seeding experiments (Fig. 1) and in numerous individual cumulus seeding experiments such as those conducted by Woodley and Simpson (1970). It is not unreasonable to assume that this same reaction could be expected in the hurricane environment considering the computations previously made by the author (Sheets, 1969). We will now enumerate the sequence of events which should occur in a hurricane seeded in a manner similar to that conducted in Hurricane Debbie (1969) and having a distinct eyewall structure with an associated maximum wind speed band. This same sequence of events were observed to have actually occurred on both Hurricane Debbie (1969) seeding days or at least can be implied to have occurred based on interpretation of the analyzed data.

The sequence of events and results are:

1. Enhancement of small scale features as depicted in the wind, temperature, and pressure fields (cumulus and cumulonimbus scales) in the immediate vicinity of the seeded area, particularly beyond the eyewall region, within minutes of the actual seeding event. This reaction

to occur with the first three or four seeding events (4-6 hour period after first seeding run) and spreading around the high energy portion of the storm.

2. Intermediate scale features as depicted in the wind, temperature, pressure, and moisture fields (rainband and eyewall scales) remain prominent or slightly enhanced during the first three or four seeding events.

3. By the time of the third or fourth seeding event, the seeding agent and its effects are dispersed over the high energy portion of the storm with the following results which occur and persist through the next 6 to 8 hr period (period of from 6 to 14 hrs. after the commencement of the seeding operation).

a. A general reduction in the temperature, pressure, and moisture gradients, particularly for rainband and eyewall scale motions with the resulting reduction in the prominence of these features.

b. A reduction in the maximum temperature values over the central regions and an increase in temperature at radii beyond the eyewall region.

c. A general increase in the moisture levels for the large scale features covering the high energy portion of the hurricanes.

The conclusions drawn above are based upon and to be applied to data collected in the mid to lower troposphere. However, with the vertical continuity known to exist in the hurricane (several case studies previously cited), these results should apply to most of the tropospheric portion of the hurricane. However, as was indicated earlier the basis for the evaluation is still empirical evidence since statistical confidence levels are difficult to ascertain.

BIBLIOGRAPHY

Black, P.G., et al., 1970: Eye-Size Changes in Hurricane Debbie on 18 and 20 August 1969. Project STORMFURY Annual Report 1969.

Colon, J.A. and Staff, 1961: On the Structure of Hurricane Daisy (1958). National Hurricane Research Project Report No. 48, U.S. Weather Bureau, October 1961.

Colon, J.A., 1964: On the Structure of Hurricane Helene (1958). National Hurricane Research Project Report No. 72, U.S. Weather Bureau December 1964.

Friedman, H.A., et al., 1969a: The ESSA Research Flight Facility Facilities, for Airborne Atmospheric Research. ESSA Technical Report ERL 126-RFF 1, Environmental Science Services Administration August 1969.

Friedman, H.A., et al., 1969b: The ESSA Research Flight Facility Data Processing Procedures. ESSA Technical Services Administration November 1969.

Gentry, R.C., 1970: Hurricane Debbie Modification Experiments, August 1969. Science, Vol. 168, pp. 473-475.

Hawkins, H.F. and D.T. Rubsom, 1968: Hurricane Hilda, 1964 II. Structure and Budgets of the Hurricane on October 1, 1964. Monthly Weather Review, Vol. 96, No. 9, pp. 617-636, September 1968.

Jordan, C.L., 1958: Mean Soundings for the West Indies Area. J. Meteorological, 15, 91-97.

La Seur, N.E. and H.F. Hawkins, 1963: An Analysis of Hurricane Cleo (1958) Based on Data from Research Reconaissance Aircraft. Monthly Weather Review, Vol. 91, Nos. 10-12, Oct-Dec 1963, pp. 694-709.

Rosenthal, S.L., 1971: Numerical Experiments of Relevance to Project STORMFURY. NOAA Technical Memorandum ERL NHRL-95, National Oceanic and Atmospheric Administration, December 1971.

Sasaki, Y., 1958: An objective analysis based on the variational method. J. Meteor. Soc. Japan, 36, 77-88.

______, 1968: Numerical Variational Method of Objective Analysis: Principle of Initialization. University of Oklahoma Research Institute, Report No. 10, 21 pp.

______, 1969: Proposed Inclusion of Time Variation Terms, Observational and Theoretical, in Numerical Variational Objective Analysis. J. Meteor. Soc. Japan, 47, No. 2, 115-124.

______, 1970a: Some Basic Formalisms in Numerical Variational Analysis, Monthly Weather Review, 99, No. 12, 875-883.

______, 1970b: Numerical Variational Analysis Formulated Under the Constraints as Determined by Longwave Equations and a Low-Pass Filter, Monthly Weather Review, 99, No. 12, 884-899.

______, 1970c: Numerical Variational Analysis with Weak Constraint and Application to Surface Analysis of Severe Storm Gust. Monthly Weather Review, 98, No. 12, 900-912.

Sheets, R.C., 1967a: On the Structure of Hurricane Janice (1958). National Hurricane Research Laboratory Report No. 76, Environmental Science Services Administration, April 1967.

______, 1967b: On the Structure of Hurricane Ella (1962). National Hurricane Research Laboratory Report No. 77, Environmental Science Services Administration, April 1967.

______, 1968: The Structure of Hurricane Dora (1964). National Hurricane Research Laboratory Report No. 83, Environmental Science Services Administration, December 1968.

______, 1969a: Some Mean Hurricane Soundings. Journal of Applied Meteorology, Vol. 8, No. 1, February, 1969, pp. 134-146.

______, 1969b: Preliminary Analysis of Cloud Physics Data Collected in Hurricane Gladys (1968), Project STORMFURY Annual Report 1968.

______, 1969c: Computations of the Seedability of Clouds in the Environment of a Hurricane, Project STORMFURY Annual Report 1968.

______, 1970: Application of Bayesian Statistics for STORMFURY Results. Project STORMFURY Annual Report, 1969.

______, 1972a: Diurnal Variation in Hurricanes. To be published in Project STORMFURY Annual Report 1971.

______, 1972b: Some Statistical Characteristics of the Hurricane Eye and the Minimum Surface Pressure. To Be published in Project STORMFURY Annual Report, 1971.

Simpson, J.S. and W.L. Woodley, 1971: Seeding Cumulus in Florida: New 1970 Results. Science, Vol. 172, pp. 117-126.

Simpson, R.H. and J.S. Malkus, 1964: Experiments in Hurricane Modification. Scientific American, Vol. 211, No. 6, pp. 27-37.

Thompson, P.D., 1961: Numerical Weather Analysis and Prediction. The Macmillan Company, New York.

Wagner, K.K., 1971: Variational Analysis Using Observational and Low-Pass Filtering Constraints. M.S. Thesis, University of Oklahoma, 39 pp.

Woodley, W.L., 1970: Rainfall Enhancement by Dynamic Cloud Modification. Science, Vol. 170, pp. 127-132.

APPENDIX A

MATHEMATICAL DEFINITIONS AND DERIVATIONS

Definitions

The definitions and approximations listed below are used in the derivations which follow. The units of the various quantities are given in knots (kt), nautical miles (n mi), degrees centigrade (°C), and grams per kilogram (gm/kg), since these are the units normally associated with airborne meteorological observations.

The scale parameters are

$V = 100$ kt $\quad T = 10^\circ C \quad M = 10$ gm/kg

$L = 20$ n mi $\quad D = .1$ n mi

$g = 980 \text{ cm/sec}^2 = 6.8515 \times 10^4 \text{ n mi/hr}^2$

$f = 4.98802 \times 10^{-5} \text{ sec}^{-1} = .1795687 \text{ hr}^{-1}$ at 20° N.

The nondimensional variables and operators are defined as

$$r = Lr' \qquad c = Vc' \qquad z = Dz'$$

$$v_\theta = Vv_\theta' \qquad T = \bar{T}t' \qquad \theta = \Theta\theta'$$

$$V = VV' \qquad v_r = Vv_r' \qquad M = \bar{M}M'$$

$$z = Dz' \qquad D = \bar{D}D' \qquad \nabla_r = \frac{1}{L}\nabla_r'$$

where the primed quantities are the nondimensional form of the variables and operators. The variables v_θ and v_r are the tangential and radial components of the wind, respectively, T is temperature, M is mixing ratio, D is the height anomaly of a given pressure surface from the same surface in the U.S. standard atmosphere (D-value), V is the observed wind speed, z is the observed height of the pressure surface, and C is the gradient wind speed.

The finite difference operators used are centered differences, i.e.,

$$\nabla_r\theta = (\theta_{n+1} - \theta_{n-1})/2d$$

$$\nabla_r^{\,2}\theta = \nabla_r\nabla_r\theta$$

$$\nabla_r^{\,n}\theta = \overbrace{\nabla_r\nabla_r\ldots\nabla}^{n}\theta$$

where θ is any variable and d is the interval Δr. The subscript n indicates the increment of Δr along the radial axis.

Scaling and Nondimensionalization of J_1

The first functional is defined in Chapter II as

$$J_1 = \int_r \{\beta(\frac{\partial^2\theta}{\partial r^2})^2 + \gamma(\frac{\partial\theta}{\partial r})^2 + \alpha(\theta - \tilde{\theta})^2\}dr \; . \qquad \text{(A.1)}$$

The scale parameters and nondimensional variables defined above are used to derive a nondimensionalized finite difference analog for (A.1), i.e.,

$$J_1 = \sum_r \{\frac{\beta\Theta^2}{L^4}(\nabla'^{\,2}_r\theta')^2 + \gamma\,\frac{\Theta^2}{L^2}(\nabla'_r\theta')^2 + \alpha\Theta^2(\theta' - \tilde{\theta}')^2\}\Delta r \; .$$

The terms $\beta\Theta^2/L^4$, $\gamma\Theta^2/L^2$, and $\alpha\Theta$ must also be nondimensionalized. To accomplish this task, we choose the nondimensional values for β, γ, and α, and then determine the implied dimensional weight from the prior given definitions and scale parameters. For instance, one set of nondimensional weights used in the analyses performed in this paper is $\alpha = 1$, $\gamma = \beta = 100$.

Letting θ be the tangential component of the wind, we obtain

$$\beta' = \frac{\beta\Theta^2}{L^4} = \frac{\beta V^2}{L^4} \text{ or } \beta = \frac{\beta' L^4}{V^2} = \frac{100 \times 100^2 \times 16\,\text{n mi}^4}{100^2\,\text{n mi}^2\,\text{hr}^{-2}}$$

$$= 1.6 \times 10^2\,\text{n mi}^2\,\text{hr}^2$$

$$\gamma' = \frac{\gamma\Theta^2}{L^2} = \frac{\gamma V^2}{L^2} \text{ or } \gamma = \frac{\gamma' L^2}{V^2} = \frac{100 \times 100 \times 4\,\text{n mi}^2}{100^2\,\text{n mi}^2\,\text{hr}^{-2}} = 4\text{ hr}^2$$

and

$$\alpha' = \alpha\Theta = \alpha V \text{ or } \alpha = \frac{\alpha'}{V} = \frac{1}{100\,\text{n mi hr}^{-1}} = 10^{-2}\text{ hr n mi}^{-1}.$$

The nondimensional finite difference analog of (A.1) becomes

$$J_1 = \sum_r \{\beta'(\nabla'^2_r\theta')^2 + \gamma'(\nabla'_r\theta')^2 + \alpha'(\theta' - \bar{\theta})^2\}\Delta r \qquad (A.2)$$

and for convenience we can drop the prime notation since all terms are now nondimensionalized.

Solution of Equation (5)

The analysis equation derived from (A.2) becomes

$$\beta\nabla_r^4\theta - \gamma\nabla_r^2\theta + \alpha(\theta - \bar{\theta}) = 0 \qquad (A.3)$$

The finite difference operators $\nabla_r^2\theta$ and $\nabla_r^4\theta$ are defined by

$$\nabla_r^2\theta = (\theta_{n+1} + \theta_{n-1} - 2\theta_n)/d^2$$

and

$$\nabla_r^4\theta = (\theta_{n+2} + \theta_{n-2} + 6\theta_n - 4\theta_{n+1} - 4\theta_{n-1})/d^4 .$$

This equation is readily solved by iterative techniques. The Liebmann method was used for this paper. This method requires that the corrected values for θ must satisfy the analysis equation. That is, if a residual exists at a point on the νth iteration, then a correction must be applied to that point such that there would be no residual on the ν+1 iteration. However, this calculation uses values from surrounding points which also must be corrected. Therefore, the method "iterates" toward the correct solution. These approximations are made in order to minimize the number of fixed end points required. The residual on the νth scan at the n^{th} point is.

$$R_n^\nu = \beta[\theta_{n+2}^\nu + \theta_{n-2}^{\nu+1} + 6\theta_n^\nu - 4\theta_{n+1}^\nu - 4\theta_{n-1}^{\nu+1}]/d^4 - \gamma[\theta_{n+1}^\nu + \theta_{n-1}^{\nu+1} - 2\theta_n^\nu]/d^2 + \alpha[\theta_n^\nu - \theta_n] \tag{A.4}$$

The required condition for the ν+1th iteration at the nth point is

$$0 = \beta[\theta_{n+2}^\nu + \theta_{n-2}^{\nu+1} + 6\theta_n^{\nu+1} - 4\theta_{n+1}^\nu - 4\theta_{n-1}^{\nu+1}]/d^4 - \gamma[\theta_{n+1}^\nu + \theta_{n-1}^{\nu+1} - 2\theta_n^{\nu+1}]/d^2 + \alpha[\theta_n^{\nu+1} - \theta_n] \tag{A.5}$$

where

$$\theta_n^{\nu+1} = \theta_n^\nu + \Delta\theta_n^\nu \quad \text{or} \quad \Delta\theta_n = \theta_n^{\nu+1} - \theta_n^\nu . \tag{A.6}$$

The term $\Delta\theta_n^\nu$ is the correction factor to be applied to θ_n^ν and is obtained by subtracting (A.4) from (A.5), i.e.,

$$-R_n^\nu = 6\beta(\theta_n^{\nu+1} - \theta_n^\nu)/d^4 + 2\gamma(\theta_n^{\nu+1} - \theta_n^\nu)/d^2 + \alpha(\theta_n^{\nu+1} - \theta_n^\nu)$$

or making use of (A.6),

$$\Delta\theta_n^\nu = - R_n^\nu/[6\beta/d^4 + 2\gamma/d^2 + \alpha]. \tag{A.7}$$

Appropriate values are chosen for the weights α, γ, and β. An initial field is specified based on the observed data and along with the observed values are inserted into Eqs. (A.4), (A.6), and (A.7). In actual practice, an over relaxation factor (Thompson, 1961) is used, i.e., Eq. (A.6) becomes

$$\theta_n^{\nu+1} = \theta_n^{\nu} + 1.9 \times \Delta\theta_n^{\nu} \tag{A.8}$$

The rate of convergence to the solution using this technique is illustrated in Fig. 5 for a typical set of data.

Scaling and Nondimensionalization of J_2

The functional containing J_1 and the gradient wind constraint is defined in Chapter II as

$$\begin{aligned} J_2 = \int_r \{&\alpha(c - \bar{v})^2 + \gamma(z - \bar{z})^2 + \beta(\frac{c^2}{r} + fc - g\frac{\partial z}{\partial r})^2 \\ &+ \mu_1(\frac{\partial c}{\partial r})^2 + \mu_2(\frac{\partial^2 c}{\partial r^2})^2 + \mu_3(\frac{\partial z}{\partial r})^2 + \mu_4(\frac{\partial^2 z}{\partial r^2})^2\}dr \end{aligned} \tag{A.9}$$

The scale parameters and nondimensionalized variables defined previously are used to derive a nondimensionalized finite difference analog for (A.9), i.e.,

$$\begin{aligned} J_2 = \sum_r \{&\alpha V^2(c' - v')^2 + \gamma D^2(z' - z')^2 \\ &+ \beta(\frac{V^2 c'^2}{Lr'} + fvc' - g\frac{D}{L}\nabla'_r z')^2 \\ &+ \mu_1(\frac{V}{L}\nabla'_r c')^2 + \mu_2(\frac{V}{L^2}\nabla'^2_r c')^2 \\ &+ \mu_3(\frac{D}{L}\nabla'_r z')^2 + \mu_4(\frac{D}{L^2}\nabla'^2_r z')^2\}\Delta r \end{aligned}$$

or

$$\begin{aligned} J_2 = \sum_r \{&\alpha V^2(c' - v')^2 + \gamma D(z' - z')^2 \\ &+ \beta\frac{V^4}{L^2}(\frac{c'^2}{r'} + \frac{fL}{V}c' - \frac{gD}{V^2}\nabla'_r z')^2 \end{aligned}$$

$$+ \mu_1 \frac{V^2}{L^2} (\nabla'_r c')^2 + \mu_2 \frac{V^2}{L^4} (\nabla'^2_r c')^2$$
$$+ \mu_3 \frac{D^2}{L^2} (\nabla'_r z')^2 + \mu_4 \frac{D^2}{L^4} (\nabla'^2_r z')^2\}\Delta r \qquad \text{(A.10)}$$

where the primes indicate nondimensional quantities. Recognizing that the Rossby number $R_0 = V/fL$ and the Froude number, $F = V/\ gd$ and defining the nondimensional weights as follows

$$\alpha' = \alpha V^2 \qquad \gamma' = \gamma D^2 \qquad \beta' = \beta V^4/L^2$$
$$\mu_1' = \mu_1 V^2/L^2 \quad \mu_2' = \mu_2 V^2/L^4 \quad \mu_3' = \mu_3 D^2/L^2$$
$$\mu_4' = \mu_4 D^2/L$$

we can write (A.10) as

$$J_2 = \sum_r \{\alpha'(c' - \overline{v}')^2 + \gamma(z' - \widetilde{z}')^2 + \beta'(\frac{c'^2}{r'} + \frac{c'}{R_0} - \frac{1}{F^2} \nabla'_r z')^2$$
$$+ \mu_1'(\nabla'_r c')^2 + \mu_2'(\nabla'^2_r c')^2 + \mu_3'(\nabla'_r z')^2$$
$$+ \mu_4'(\nabla'^2_r z')^2\}\Delta r \qquad \text{(A.11)}$$

where all terms are nondimensional and the prime notation can be dropped for convenience.

Solutions of Equations (16) and (17)

The analysis equations derived from (A.11) result in a set of two non-linear difference equations which must be solved simultaneously. The resulting equations are

$$\beta[- \frac{1}{F^2} (\frac{2c}{r} + \frac{1}{R_0}) \nabla_r z + \frac{2c^3}{r^2} + \frac{3c^2}{rR_0} + \frac{c}{R_0^2}]$$
$$+ \mu_2 \nabla_r^4 c - \mu_1 \nabla_r^2 c + \alpha(c - \overline{v}) = 0 \qquad \text{(A.12)}$$

and

$$\frac{\beta}{F^2}\left[-\frac{1}{F^2}\nabla_r^{\ 2}z + \frac{1}{R_0}\nabla_r c + \frac{1}{r}\nabla_r c^2 - \frac{c^2}{r^2}\right]$$

$$+ \mu_4\nabla_r^{\ 4}z - \mu_3\nabla_r^{\ 2}z + \alpha(z - \tilde{z}) = 0\,. \tag{A.13}$$

These equations are solved by use of the sequential relaxation or Liebmann method. The residual on the νth scale at the nth point for Eq. (A.12) is

$$R_n^\nu = -\frac{2\beta L c_n^\nu}{2F^2 dr_n}(z_{n+1}^\nu - z_{n-1}^{\nu+1}) - \frac{L\beta}{2dF^2R_0}(z_{n+1}^\nu - z_{n-1}^{\nu+1})$$

$$+ \frac{2\beta}{r_n^{\ 2}}(c_n^\nu)^3 + \frac{3\beta}{R_0 r_n}(c_n^\nu)^2 + \frac{\beta}{R_0^{\ 2}}c_n^\nu$$

$$+ L^4\mu_2[c_{n+2}^\nu + c_{n-2}^{\nu+1} + 6c_n^\nu - 4c_{n+1}^\nu - 4c_{n-1}^{\nu+1}]/d^4$$

$$- L^2\mu_1[c_{n+1}^\nu + c_{n-1}^{\nu+1} - 2c_n^\nu]/d^2 + \alpha[c_n^\nu - v_n]\,. \tag{A.14}$$

The required condition for the $\nu+1$ iteration at the nth point is

$$0 = -\frac{2\beta L}{2F^2 d}\frac{c_n^{\nu+1}}{r_n}(z_{n+1}^\nu - z_{n-1}^{\nu+1}) - \frac{L\beta}{2dF^2R_0}(z_{n+1}^\nu - z_{n-1}^{\nu+1})$$

$$+ \frac{2\beta}{r_n^{\ 2}}(c_n^{\nu+1})^3 + \frac{3\beta}{R_0 r_n}(c_n^{\nu+1})^2 + \frac{\beta}{R_0^{\ 2}}c_n^{\nu+1}$$

$$+ L^4\mu_2[c_{n+2}^\nu + c_{n-2}^{\nu+1} + 6c_n^{\nu+1} - 4c_{n+1}^\nu - 4c_{n-1}^{\nu+1}]d^4$$

$$- L^2\mu_1[c_{n+1}^\nu + c_{n-1}^{\nu+1} + 2c_n^{\nu+1}]/d^2 + \alpha[c_n^{\nu+1} - v_n] \tag{A.15}$$

where

$$c_n^{\nu+1} = c_n^\nu + \Delta c_n^\nu \qquad \text{or} \qquad \Delta c_n^\nu = c_n^{\nu+1} - c_n^\nu$$

and

$$z_n^{\nu+1} = z_n^\nu + \Delta z_n^\nu \qquad \text{or} \qquad \Delta z_n^\nu = z_n^{\nu+1} - z_n^\nu \tag{A.16}$$

The terms Δc_n^ν and Δz_n^ν are the correction factors to be applied to c_n^ν and z_n^ν. The term Δc_n can be obtained by subtracting (A.14) from (A.15), i.e.,

$$-R_n^\nu = -\frac{L\beta}{dF^2 r_n}(z_{n+1}^\nu - z_{n-1}^{\nu+1})(c_n^{\nu+1} - c_n^\nu)$$
$$+ \frac{2\beta}{R_0^2}[(c_n^{\nu+1})^3 - (c_n^\nu)^3] + \frac{3\beta}{R_0 r_n}[(c_n^{\nu+1})^2 - (c_n^\nu)^2]$$
$$+ \frac{\beta}{R_0^2}(c_n^{\nu+1} - c_n^\nu) + 6\mu_2 L^4(c_n^{\nu+1} - c_n^\nu)/d^4$$
$$+ 2L^2\mu_1(c_n^{\nu+1} - c_n^\nu)/d^2 + \alpha(c_n^{\nu+1} - c_n^\nu) \qquad \text{(A.17)}$$

Making use of (A.16), we obtain

$$(c_n^{\nu+1})^2 = (c_n^\nu + \Delta c_n^\nu)^2 = (c_n^\nu)^2 + 2c_n^\nu\Delta c_n^\nu + (\Delta c_n^\nu)^2$$

and

$$(c_n^{\nu+1})^3 = (c_n^\nu + \Delta c_n^\nu)^3 = (c_n^\nu)^3 + 3(c_n^\nu)^2\Delta c_n^\nu$$
$$+ 3c_n^\nu(\Delta c_n^\nu)^2 + (\Delta c_n^\nu)^3 \qquad \text{(A.18)}$$

Substituting (A.16) and (A.18) into (A.17), we obtain

$$-R_n^\nu = -\frac{L\beta}{dF^2 r_n}(z_{n+1}^\nu - z_{n-1}^{\nu+1})\Delta c_n^\nu + \frac{2\beta}{r_n^2}$$
$$[(c_n^\nu)^3 + 3(c_n^\nu)^2\Delta c_n^\nu + 3c_n^\nu(\Delta c_n^\nu)^2 + (\Delta c_n^\nu)^3 - (c_n^\nu)^3]$$
$$+ \frac{3\beta}{R_0 r_n}[(c_n^\nu)^2 + 2c_n^\nu\Delta c_n^\nu + (\Delta c_n^\nu)^2 - (c_n^\nu)^2]$$
$$+ \frac{\beta}{R_0^2}\Delta c_n^\nu + \frac{6\mu_2}{d^4}L^4\Delta c_n^\nu + \frac{2\mu_1 L^2}{d^2}\Delta c_n^\nu + \alpha\Delta c_n^\nu$$

or

$$-R_n^\nu = \frac{2\beta}{r_n^2}(\Delta c_n^\nu)^3 + \left[\frac{6\beta}{r_n^2}c_n^\nu + \frac{3\beta}{R_0 r_n}\right](\Delta c_n^\nu)^2$$
$$+ \left[-\frac{L\beta}{dF^2 r_n}(z_{n+1}^\nu - z_{n-1}^{\nu+1}) + \frac{6\beta}{r_n^2}(c_n^\nu)^2 + \frac{6\beta}{R_0 r_n}c_n^\nu\right.$$

$$+ \frac{\beta}{R_0{}^2} + \frac{6\mu_2 L^4}{d^4} + \frac{2\mu_1 L^2}{d^2} + \alpha]\Delta c_n^\nu \tag{A.19}$$

If we assume Δc_n is small, we can ignore the higher order terms in Δc_n and (A.19) becomes

$$\Delta c_n^\nu \approx -R_n^\nu/[- \frac{\beta L}{dF^2 r_n} (z_{n+1}^\nu - z_{n-1}^{\nu+1}) + \frac{6\beta}{r_n{}^2} (c_n^\nu)^2$$
$$+ \frac{6\beta}{R_0 r_n} c_n^\nu + \frac{\beta}{R_0{}^2} + \frac{6\mu_2 L^4}{d^4} + \frac{2\mu_1 L^2}{d^2} + \alpha] \tag{A.20}$$

Following a similar process, the residual on the νth scan at the nth point for Eq. (A.13) is

$$R_n^\nu = \frac{\beta}{F^2}\{- \frac{L^2}{F^2} (z_{n+1}^\nu + z_{n-1}^{\nu+1} - 2z_n^\nu)/d^2 + \frac{L}{R_0} (c_{n+1}^\nu - c_{n-1}^{\nu+1})/2d$$
$$+ \frac{L}{r_n}[(c_{n+1}^\nu)^2 - (c_{n-1}^{\nu+1})^2]/2d - \frac{1}{r_n{}^2} (c_n^\nu)^2\}$$
$$+ \mu_4 L^4[z_{n+2}^\nu + z_{n-2}^\nu + 6z_n^\nu - 4z_{n+1}^\nu - 4z_{n-1}^{\nu+1}]/d^4$$
$$- \mu_3 L^2[z_{n+1}^\nu + z_{n-1}^{\nu+1} - 2z_n^\nu]/d^2 + \gamma(z_n^\nu - z_n) \tag{A.21}$$

The required condition for the $\nu+1$ iteration at the nth point is

$$0 = \frac{\beta}{F^2}\{- \frac{L^2}{F^2} (z_{n+1}^\nu + z_{n-1}^\nu - 2z_n^{\nu+1})/d^2$$
$$+ \frac{L}{R_0}(c_{n+1}^\nu - c_{n-1}^{\nu+1})/2d - \frac{1}{r_n{}^2} (c_n^{\nu+1})^2$$
$$+ \frac{1}{r_n}[(c_{n+1}^\nu)^2 - (c_{n-1}^{\nu+1})^2]/2d\}$$
$$+ \mu_4 L^4[z_{n+2}^{\nu+1} + z_{n-2}^{\nu+1} + 6z_n^{\nu+1} - 4z_{n+1}^\nu - 4z_{n-1}^\nu]/d^4$$
$$- \mu_3 L^2[z_{n+1}^\nu + z_{n-1}^{\nu+1} - 2z_n^{\nu+1}]/d^2 + \gamma(z_n^{\nu+1} - z_n) . \tag{A.22}$$

Subtracting (A.21) from (A.22), we obtain

$$-R_n^\nu = \frac{\beta}{F^2}\{\frac{2L^2}{F^2d^2}(z_n^{\nu+1} - z_n^\nu) - \frac{1}{r_n{}^2}[(c_n^{\nu+1})^2 - (c_n^\nu)^2]\} + \frac{6\mu_4L^4}{d^4}(z_n^{\nu+1} - z_n^\nu) + \frac{2\mu_3L^2}{d^2}(z_n^{\nu+1} - z_n^\nu) + \gamma(z_n^{\nu+1} - z_n^\nu) \tag{A.23}$$

Substituting (A.16) and (A.18) into (A.23) we obtain

$$-R_n^\nu = \frac{\beta}{F^2}\{\frac{2L^2}{F^2d^2}\Delta z_n^\nu - \frac{1}{r_n{}^2}[(c_n^\nu)^2 + 2c_n^\nu\Delta c_n^\nu + (\Delta c_n^\nu)^2 - (c_n^\nu)^2]\} + \frac{6\mu_4L^4}{d^4}\Delta z_n^\nu + \frac{2\mu_3L^2}{d^2}\Delta z_n^\nu + \gamma\Delta z_n^\nu$$

or

$$\Delta z_n^\nu = [-R_n^\nu - \frac{\beta}{F^2r_n^2}(\Delta c_n^\nu)^2 - \frac{2\beta}{F^2r_n^2}c_n^\nu\Delta c_n^\nu]/ [\frac{2\beta L^2}{F^4d^2} + \frac{6\mu_4L^4}{d^4} + \frac{2\mu_3L^2}{d^2} + \gamma] \tag{A.24}$$

Appropriate values are chosen for the weights α, β, γ, μ_1, μ_2, μ_3, and μ_4 and an initial or first guess field is specified by obtaining values at each grid point by a simple extrapolation of the nearest observed values to point. This initial field, along with the observed values are used in Eqs. (A.14), (A.16), (A.20), (A.21), and (A.24) to obtain the analyzed field. Again, in actual practice, an overrelaxation factor is used, i.e., Eq. (A.16) becomes

$$c_n^{\nu+1} = c_n^\nu + 1.9\Delta c_n^\nu \quad \text{and} \quad z_n^{\nu+1} = z_n^\nu + 1.9\Delta z_n^\nu \tag{A.25}$$

An illustration of the rate of convergence to the solution for this set of equations and technique is shown in Fig. 7 for a typical set of data.

TABLE 1

MAXIMUM SPECIFIC KINETIC ENERGY (KT^2)

AND PERCENT CHANGES FOR HURRICANE DEBBIE ON AUGUST 18, 1969

Filter	Obs. Time (GMT) (SW-NE/SE-NW)	QUADRANT				
		SW	NE	SE	NW	NET
"A"	(1) 1313/1204	2604	3878	2625	2475	3878
	(2) 1825/1644	3248	3537	2610	3328	3537
	(3) 0157/0108	1789	2168	1613	2111	2168
	% change (1) to (2)	+24.73	- 8.79	- 0.57	+34.46	- 8.79
	% change (2) to (3)	-44.91	-38.70	-38.19	-36.56	-38.70
	% change (1) to (3)	-31.29	-44.09	-38.55	-14.70	-44.09
"B"	(1) 1313/1204	2049	3370	2251	1953	3370
	(2) 1825/1644	2620	2891	2438	2661	2891
	(3) 0157/0108	1667	1949	1486	1869	1949
	% change (1) to (2)	+27.86	-14.21	+ 8.30	+36.25	-14.21
	% change (2) to (3)	-36.37	-32.58	-39.04	-29.76	-32.58
	% change (1) to (3)	-18.64	-42.16	-33.98	- 4.30	-42.16
"C"	(1) 1313/1204	1307	2557	1712	1432	2557
	(2) 1825/1644	1664	1917	1811	1663	1917
	(3) 0157/0108	1423	1564	1291	1637	1637
	% change (1) to (2)	+27.31	-25.02	+ 5.78	+16.13	-25.02
	% change (2) to (3)	-14.48	-18.41	-28.71	- 1.56	-14.60
	% change (1) to (3)	+ 8.87	-38.83	-24.59	+14.31	-35.97

These values were obtained by application of filters "A", "B", and "C", and are given by quadrant as well as the net change regardless of quadrant.

TABLE 2

MAXIMUM SPECIFIC KINETIC ENERGY (KT^2)

AND PERCENT CHANGES FOR HURRICANE DEBBIE ON AUGUST 20, 1969

Filter	Obs. Time (GMT) (SW-NE/SE-NW)	QUADRANT SW	NE	SE	NW	NET
"A"	(1) 1140/0955	3374	3448	3931	3755	3931
	(2) 1700/1445	4069	3637	3863	3912	4069
	(3) 0210/2311	3576	2959	3822	3902	3902
	% change (1) to (2)	+20.59	+ 5.48	- 1.72	+ 4.18	+ 3.51
	% change (2) to (3)	-12.11	-18.64	- 1.06	- 0.25	- 4.10
	% change (1) to (3)	+ 5.98	-14.18	- 2.77	+ 3.91	- 0.73
"B"	(1) 1140/0955	2929	2691	3378	3033	3378
	(2) 1700/1445	3611	3335	3452	3495	3611
	(3) 0210/2311	3170	2666	3268	3521	3521
	% change (1) to (2)	+23.28	+23.93	+ 2.19	+15.23	+ 6.89
	% change (2) to (3)	-12.21	-20.05	- 5.33	+ 0.74	- 2.49
	% change (1) to (3)	+ 8.22	- 0.92	- 3.25	+16.08	+ 4.23
"C"	(1) 1140/0955	2317	2162	2699	2300	2699
	(2) 1700/1445	2603	2498	2720	2550	2720
	(3) 0210/2311	2368	1973	2306	2660	2660
	% change (1) to (2)	+12.34	+15.54	+ 0.77	+10.86	+ 0.77
	% change (2) to (3)	- 9.02	-21.01	-15.22	+ 4.31	- 2.20
	% change (1) to (3)	+ 2.20	- 8.74	-14.56	+15.65	- 1.44

These values were obtained by application of filters "A", "B", and "C", and are given by quadrant as well as the net change regardless of quadrant.

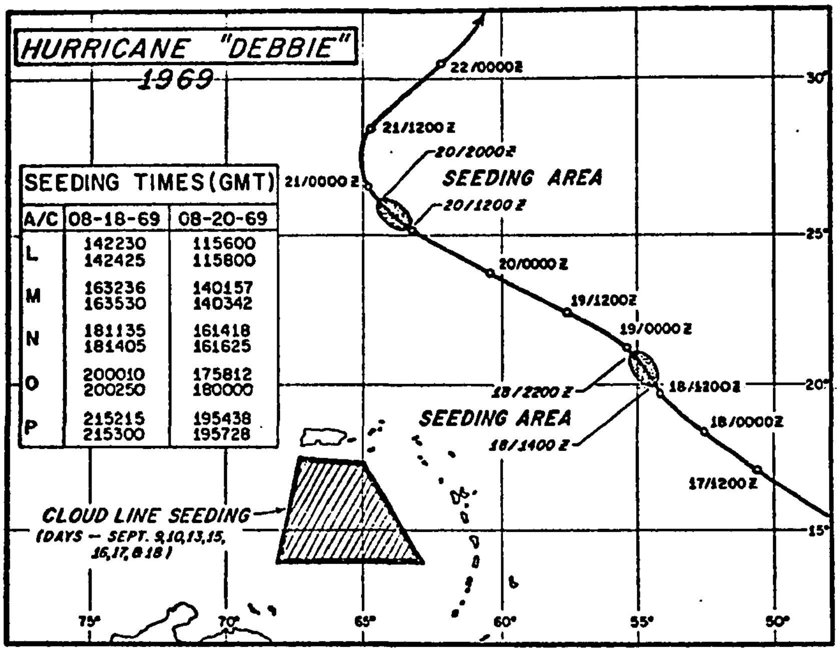

Fig. 1 Hurricane Debbie (1969) storm track and geographical locations of the modification experiments.

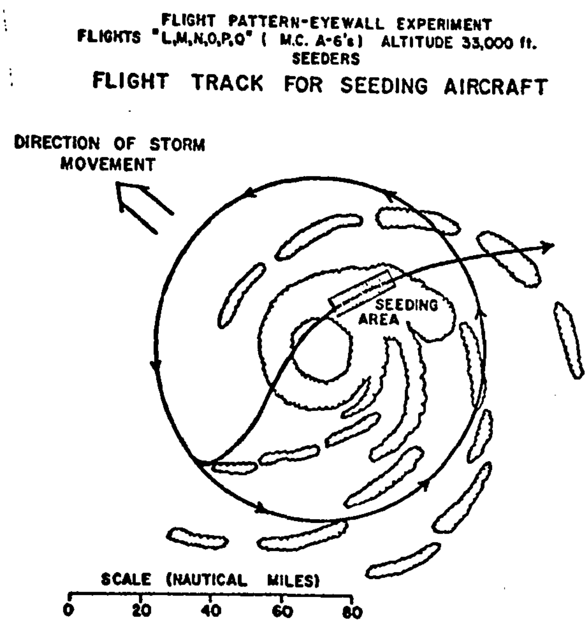

Fig. 2 Seeding area and flight pattern for the seeder aircraft for "eyewall" experiments.

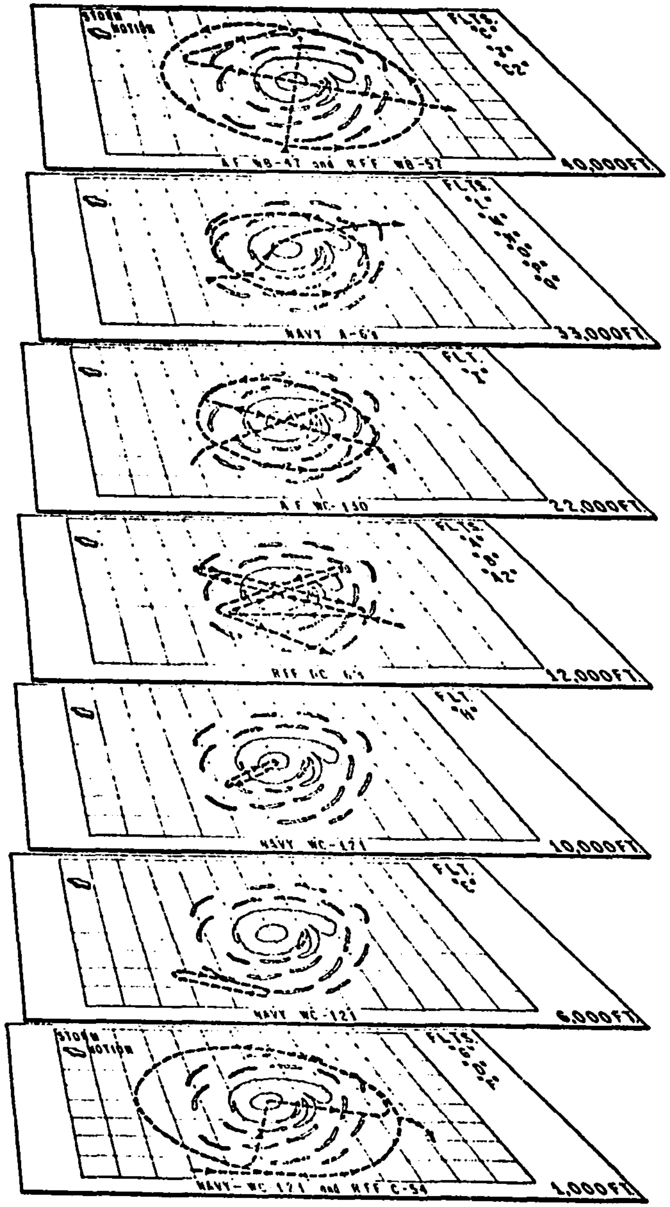

Fig. 3. Flight patterns for aircraft involved in Hurricane "eyewall" experiments.

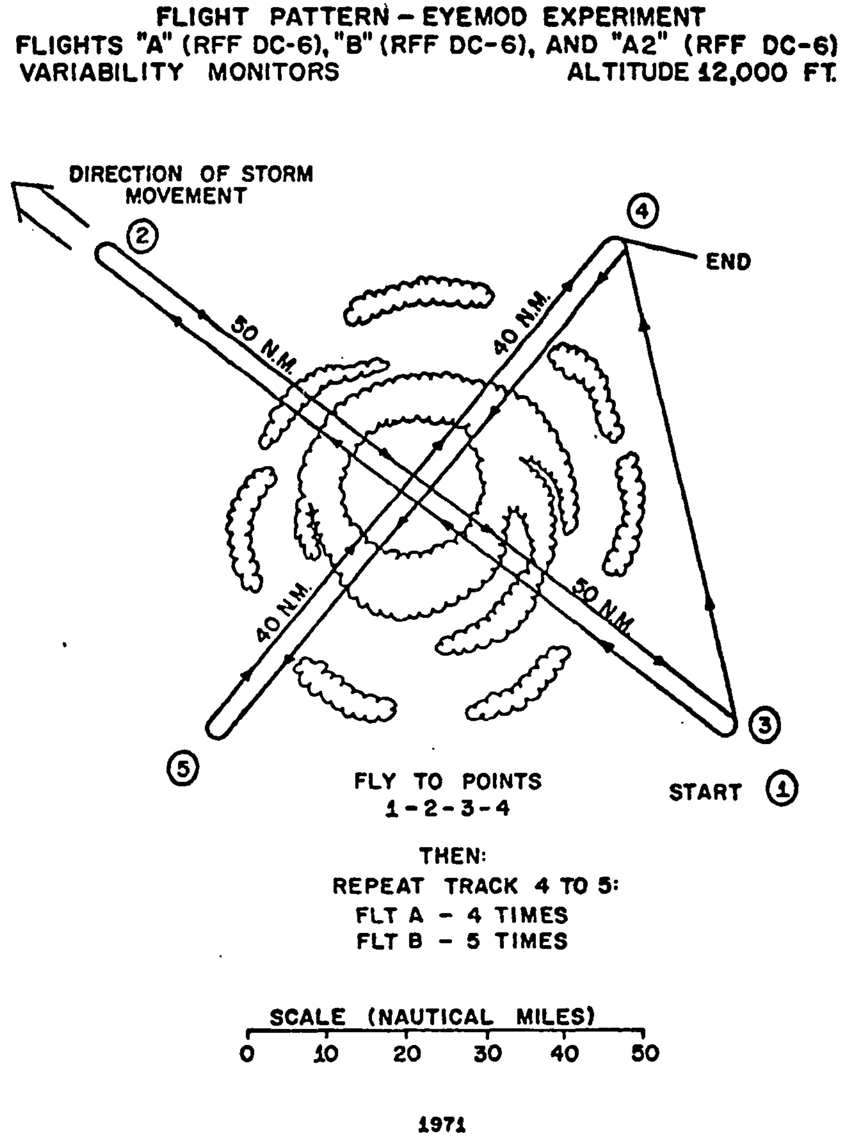

Fig. 4. Flight pattern for NOAA Research Flight Facility DC-6 aircraft eyewall experiment monitoring missions.

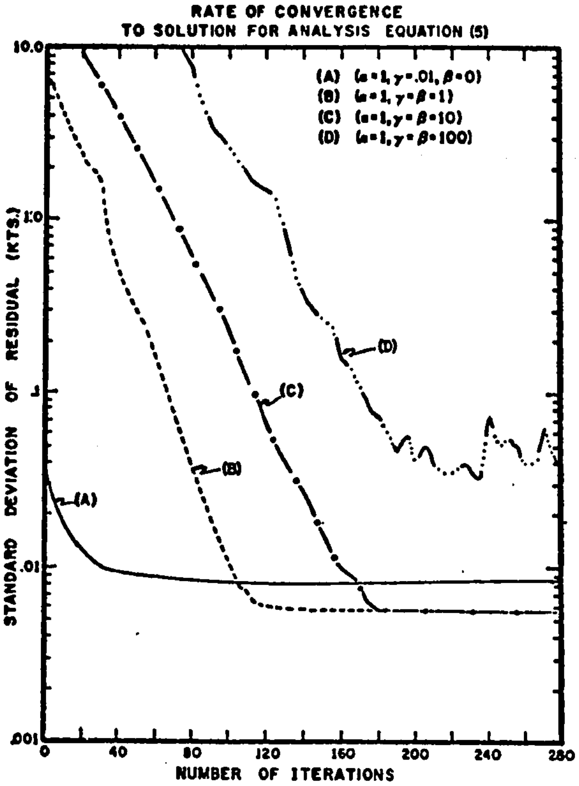

Fig. 5. Rate of convergence to the solution of the analysis equation (5) derived from the functional J1 using the Liebmann sequential relaxation technique and a typical set of data and selected weights.

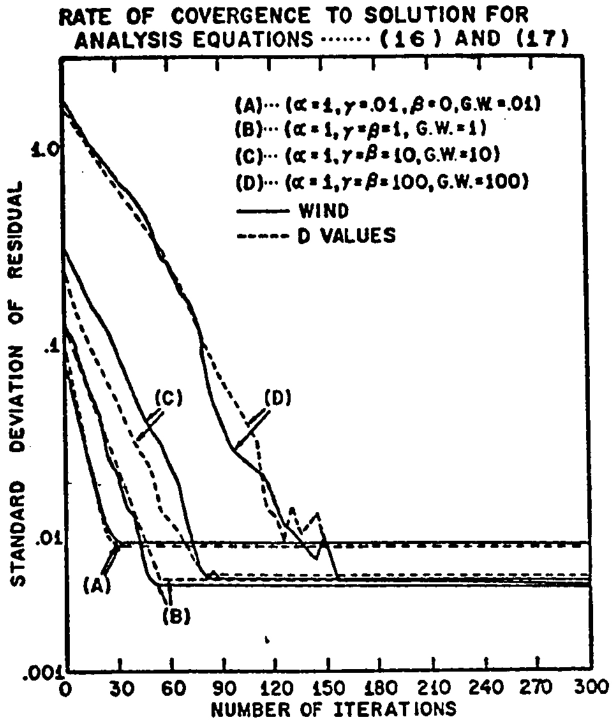

Fig. 7. Rate of convergence to the solution of the analysis equations (16 and 17) derived from the functional J2 using the Liebmann sequential relaxation technight and a typical set of data and selected weights.

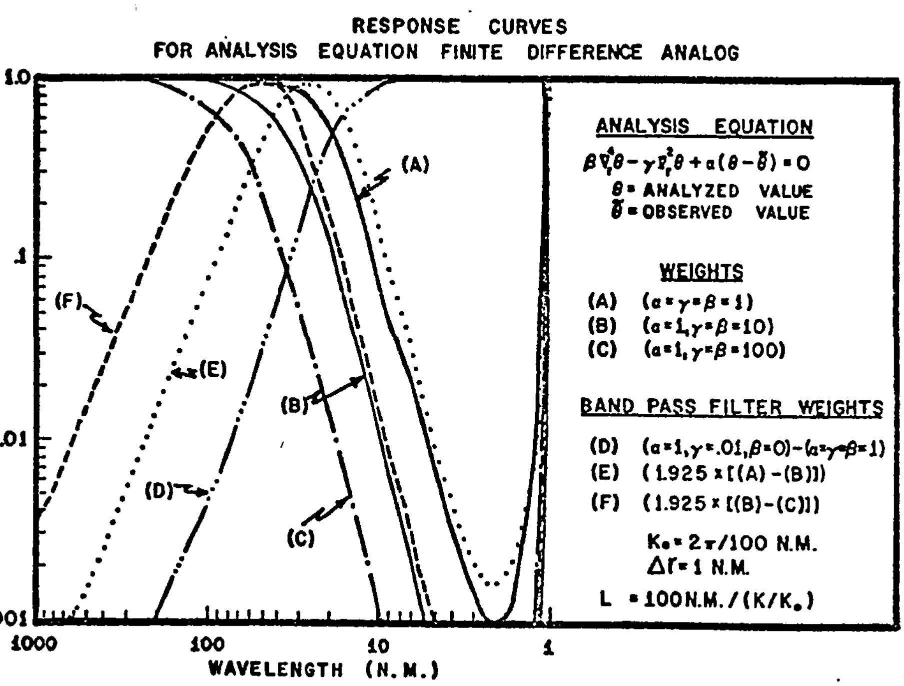

Fig. 6. Response curves for the analysis equation derived from the functional J1 for selected weights.

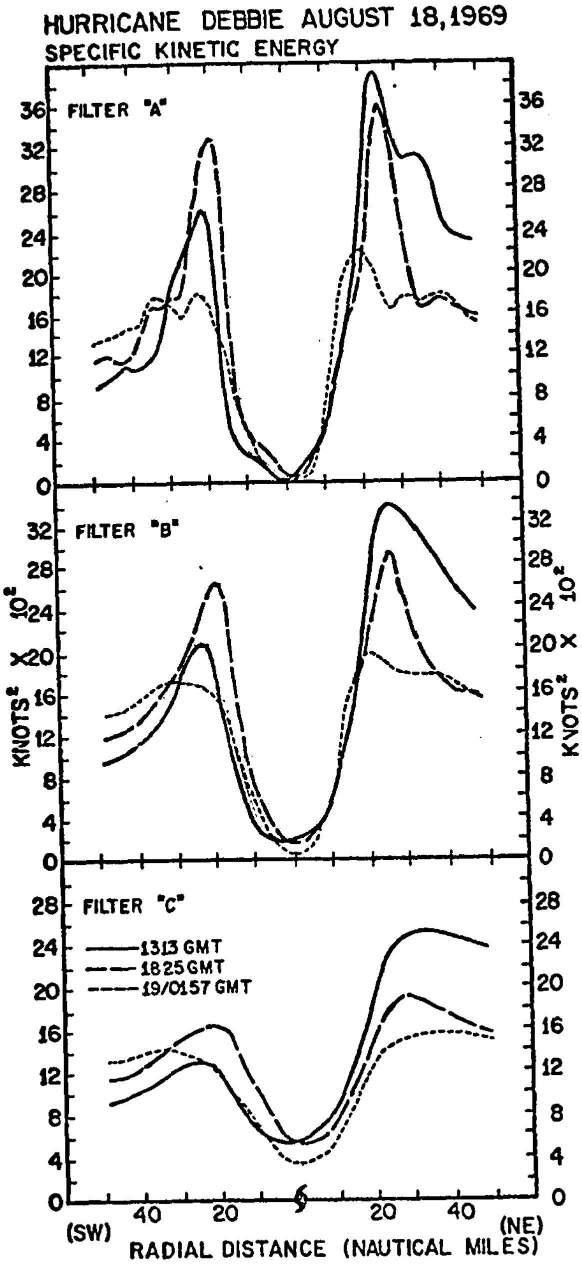

Fig. 8. Kinetic energy profiles for the left and right (SW-NE) sides of the storm, resulting from application of filters "A", "B", and "C" to the observed data.

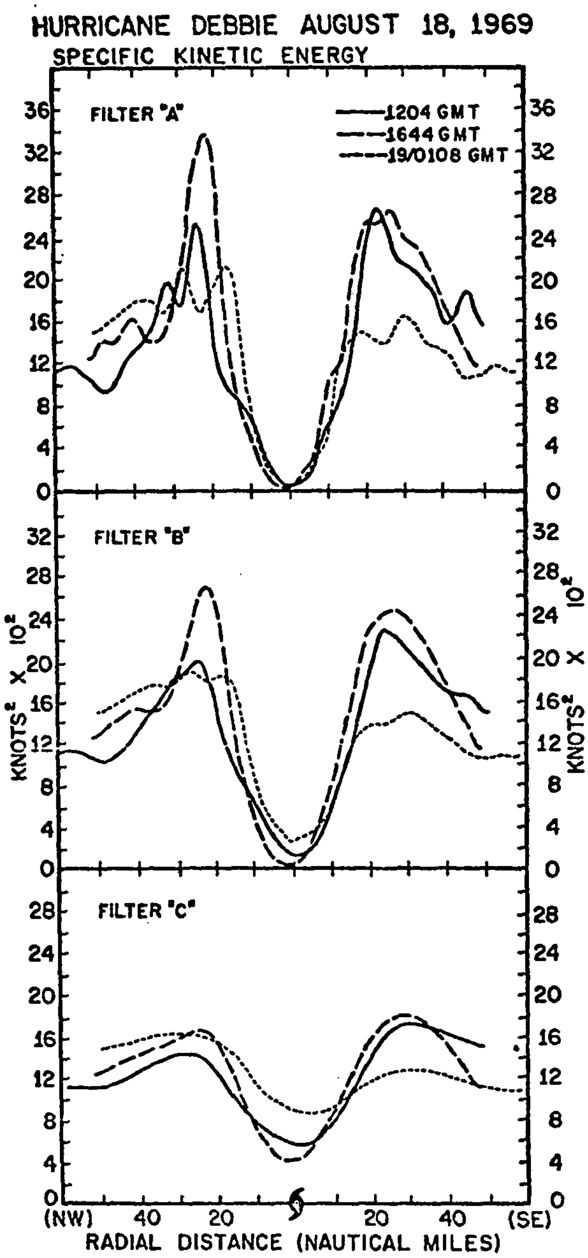

Fig. 9. Kinetic energy profiles for the front and rear (NW-SE) portions of the storm, resulting from application of filters "A", "B", and "C" to the observed data.

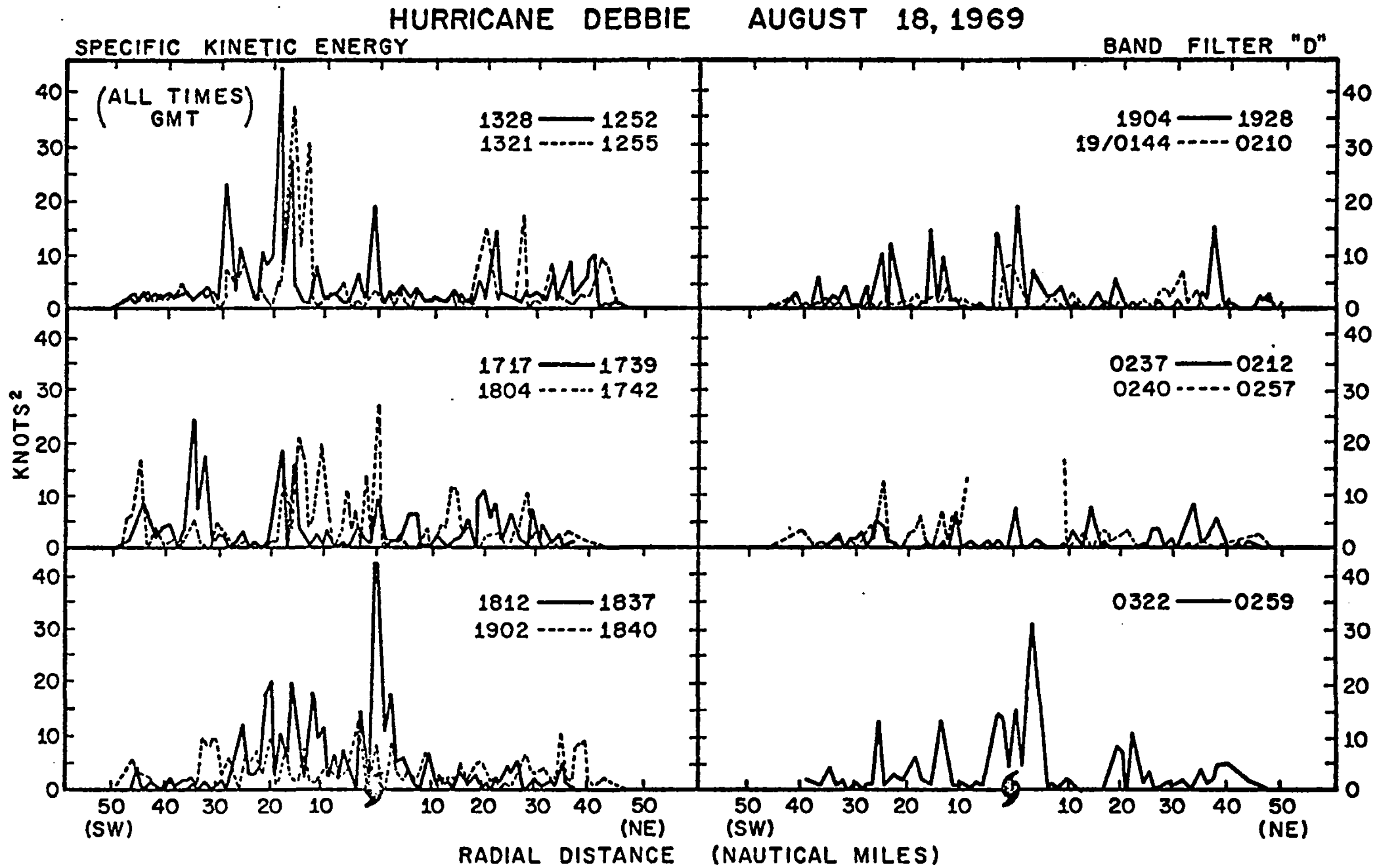

Fig. 10. Kinetic energy profiles resulting from application of band filter "D" (~ cumulonimbus scale) to the data recorded in the southwest and northeast portions of the storm.

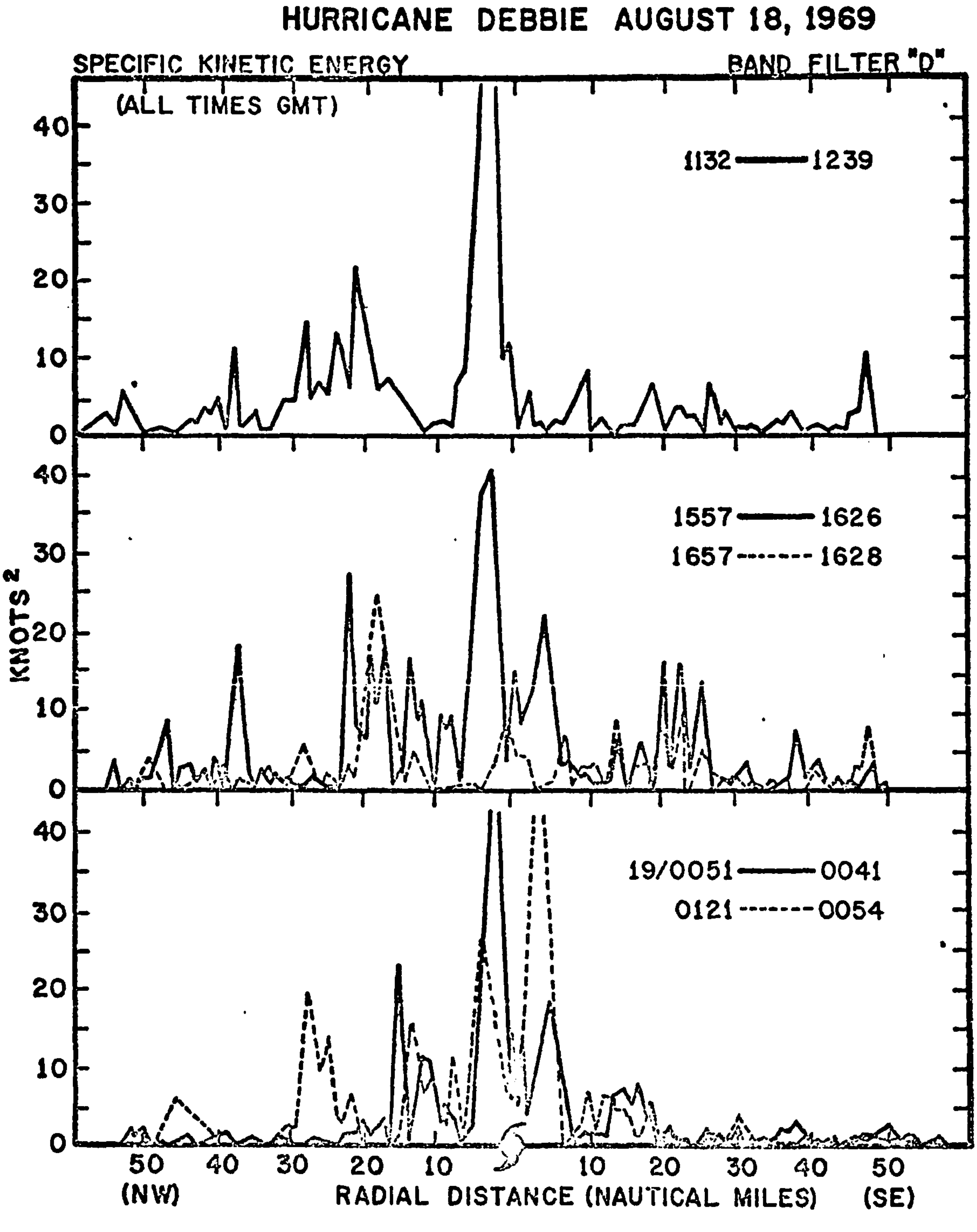

Fig. 11. Kinetic energy profiles resulting from application of band filter "D" (~ cumulonimbus scale) to the data recorded in the northwest and southeast portions of the storm.

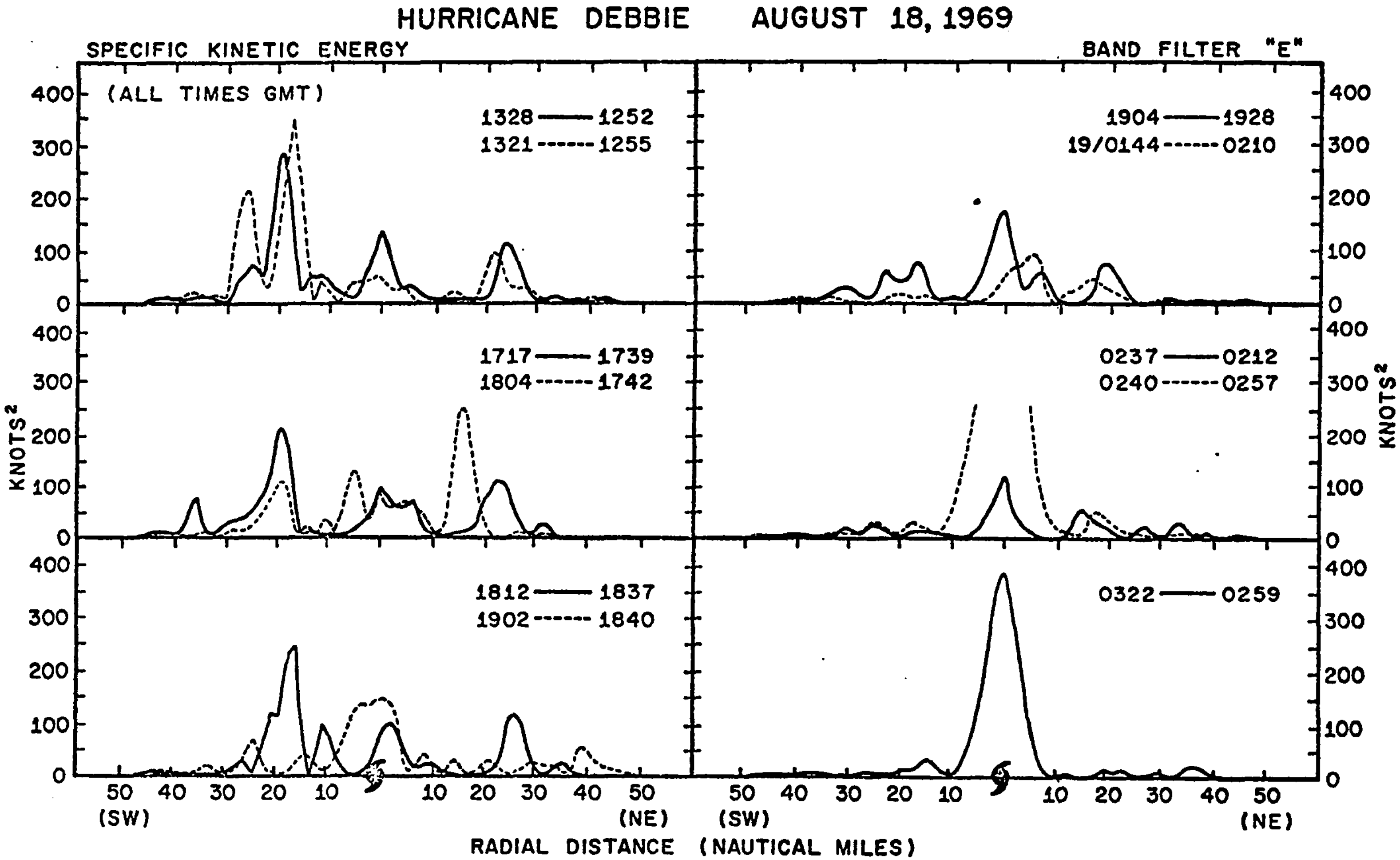

Fig. 12. Kinetic energy profiles resulting from application of band filter "E" (~ rainband scale) to the data recorded in the southwest and northeast portions of the storm.

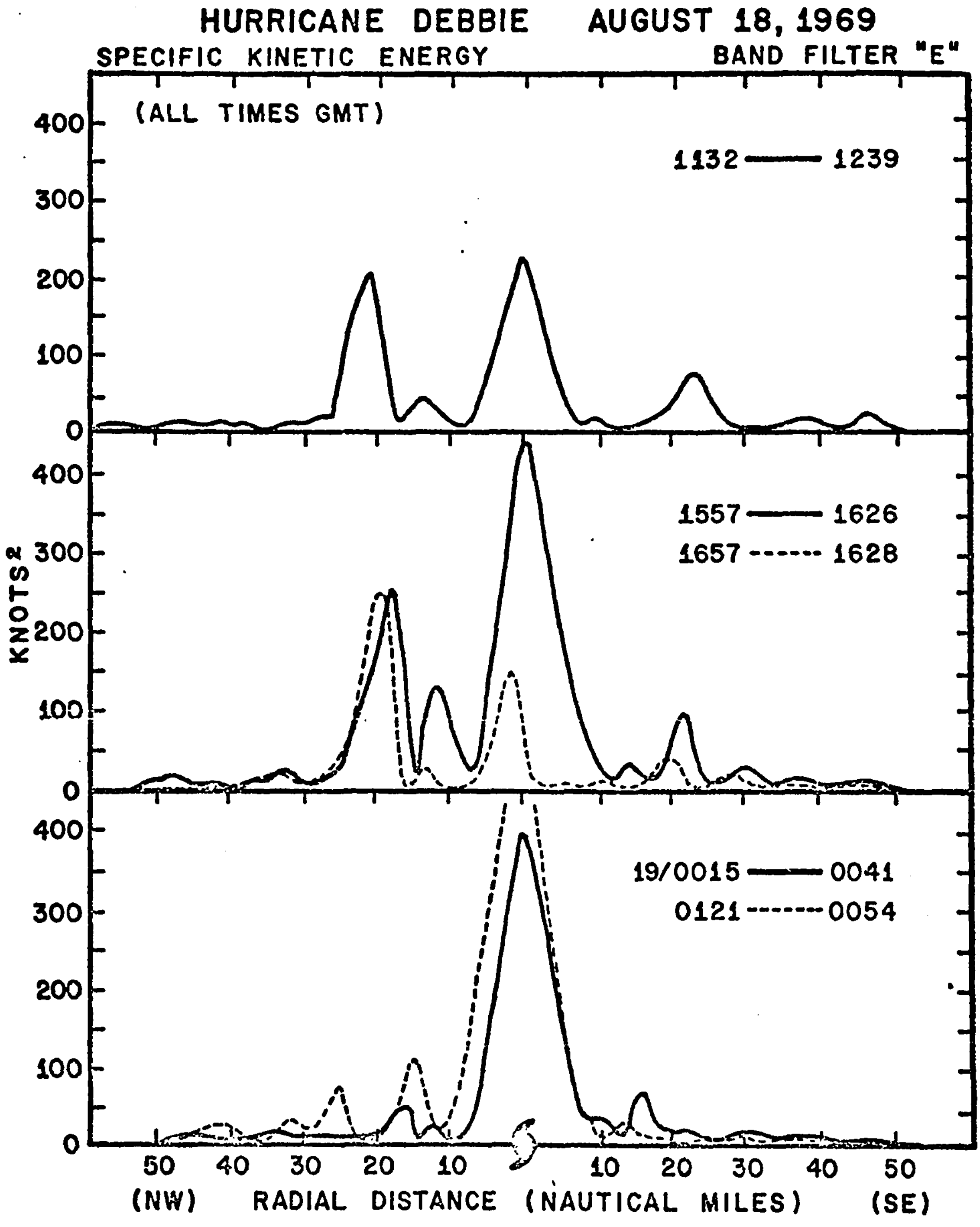

Fig. 13. Kinetic energy profiles resulting from application of band filter "E" (~ rainband scale) to the data recorded in the northwest and southeast portions of the storm.

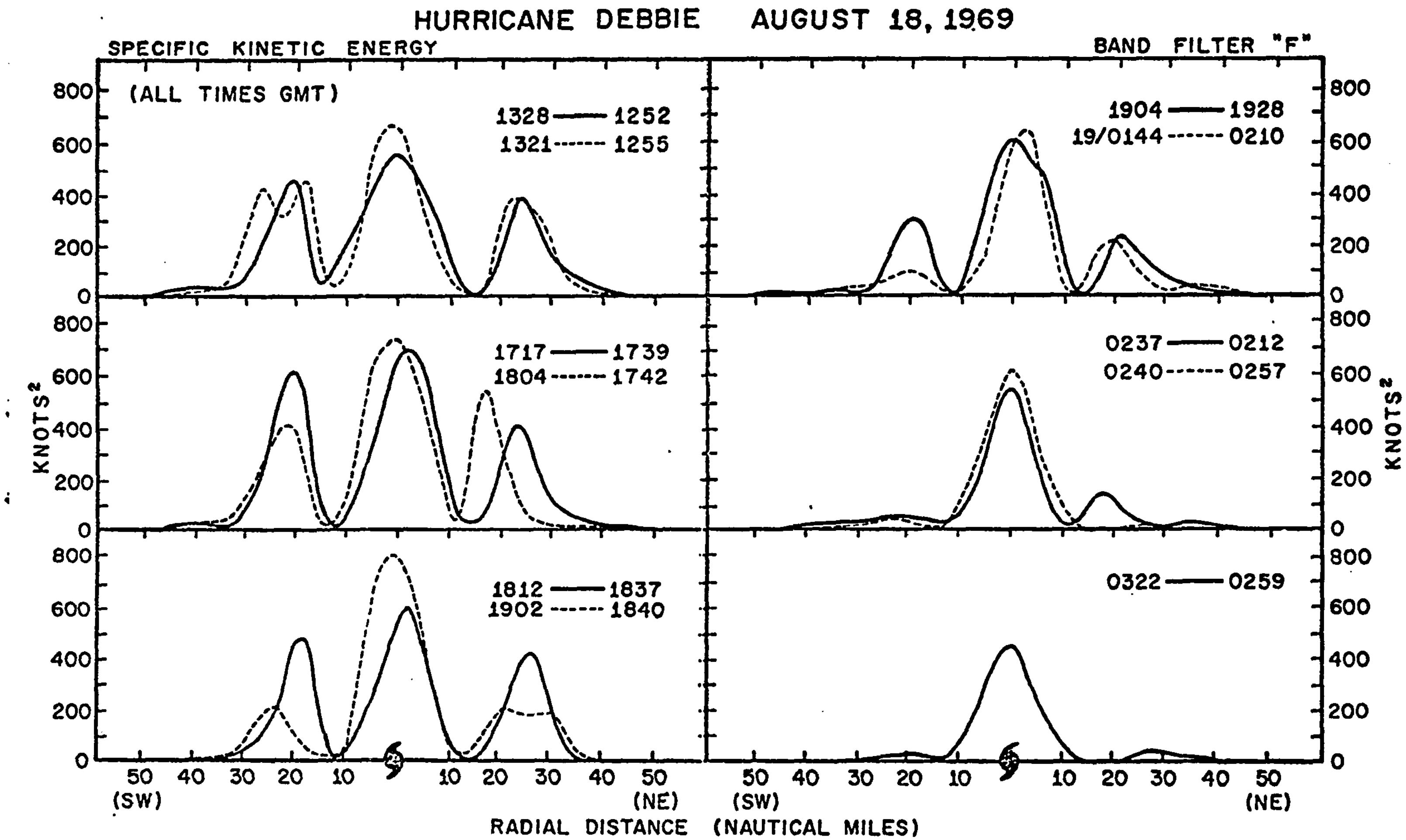

Fig. 14. Kinetic energy profiles resulting from application of band filter "F" (~ eyewall scale) to the data recorded in the southwest and northeast portions of the storm.

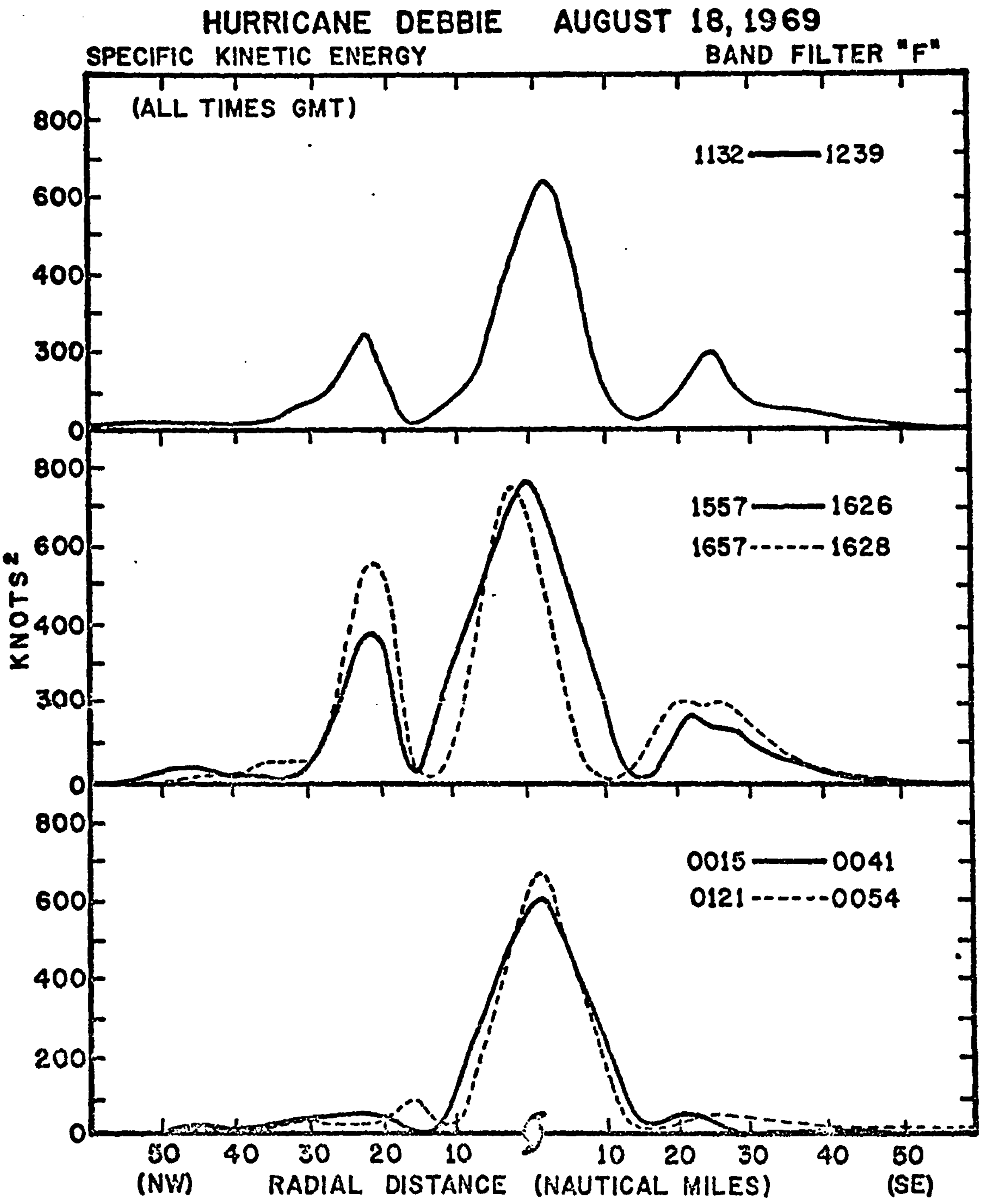

Fig. 15. Kinetic energy profiles resulting from application of band filter "F" (~ eyewall scale) to the data recorded in the northwest and southeast portions of the storm

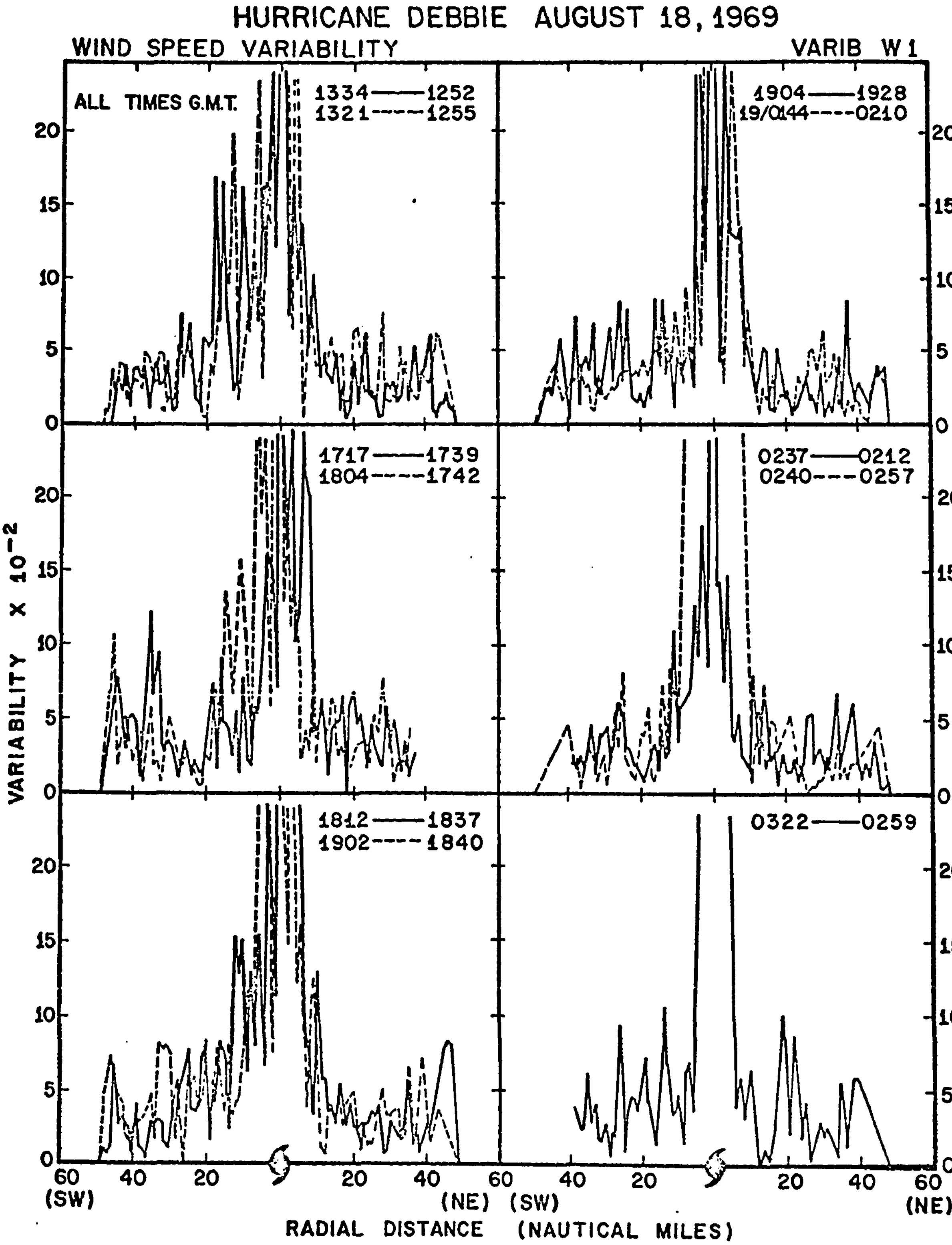

Fig. 16. Relative wind speed variability profiles for approximate cumulonimbus scale motion (VARIB W1).

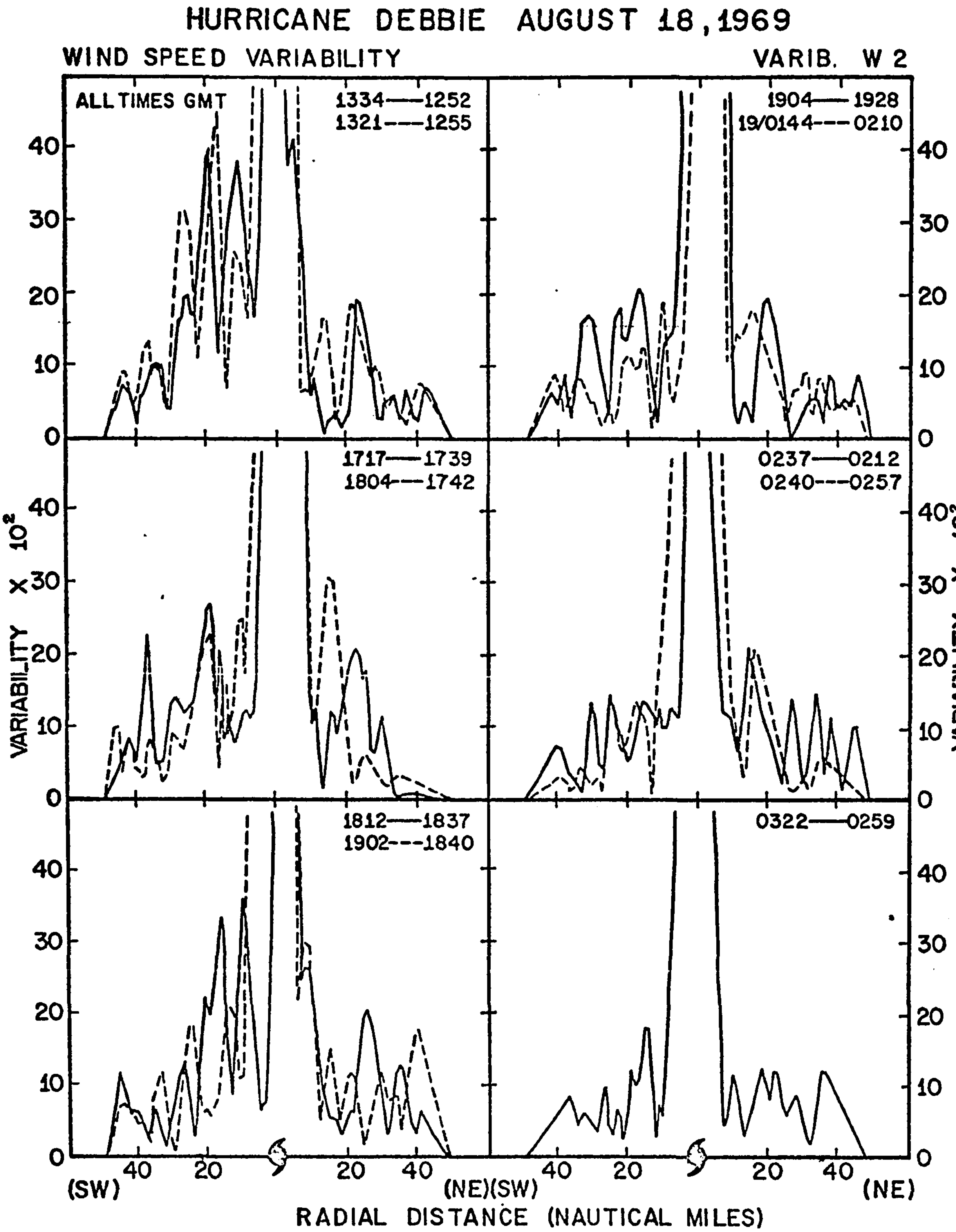

Fig. 17. Relative wind speed variability profiles for approximate rainband scale motion (VARIB W2).

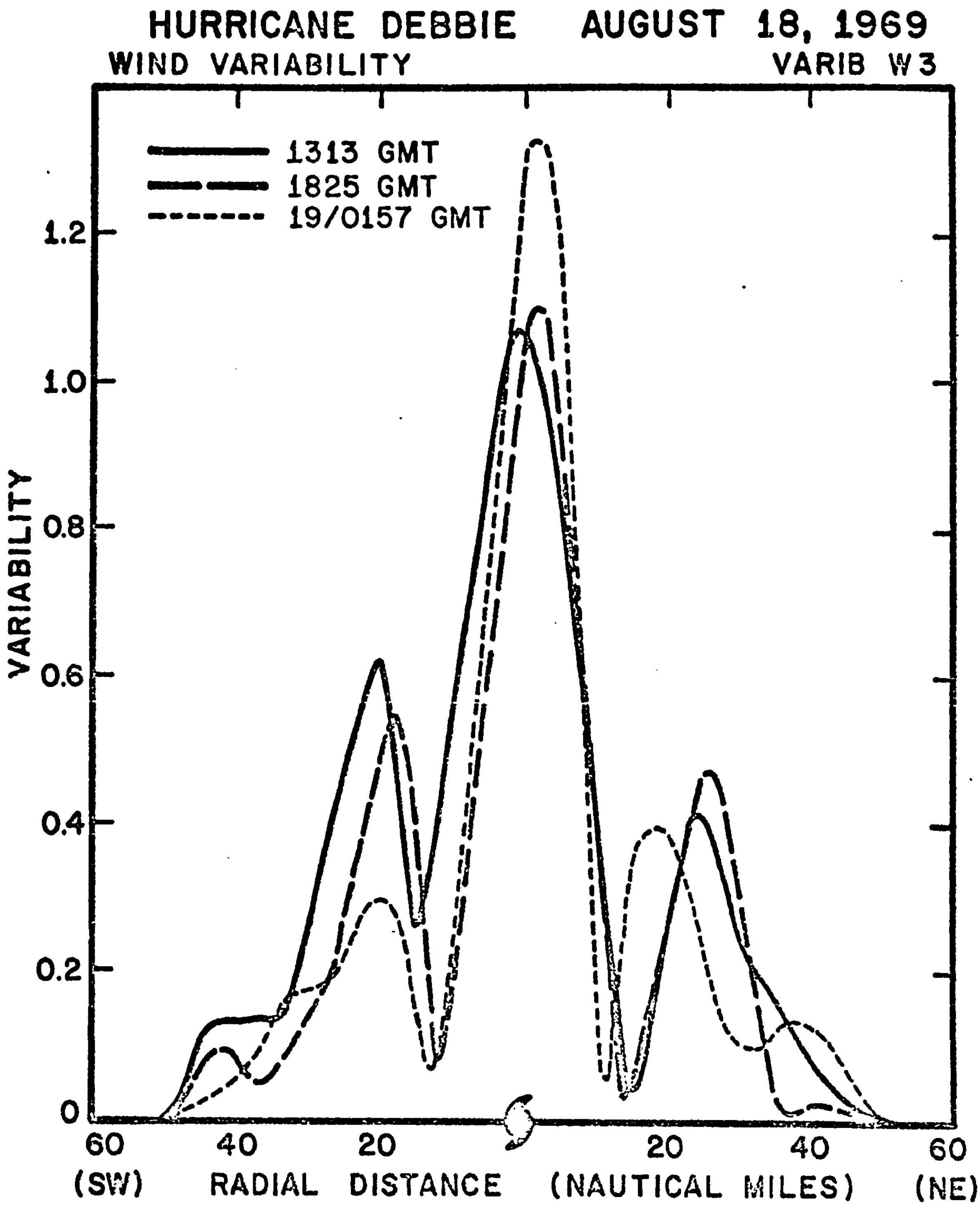

Fig. 18. Relative wind speed variability profiles for approximate eyewall scale motion (VARIB W3).

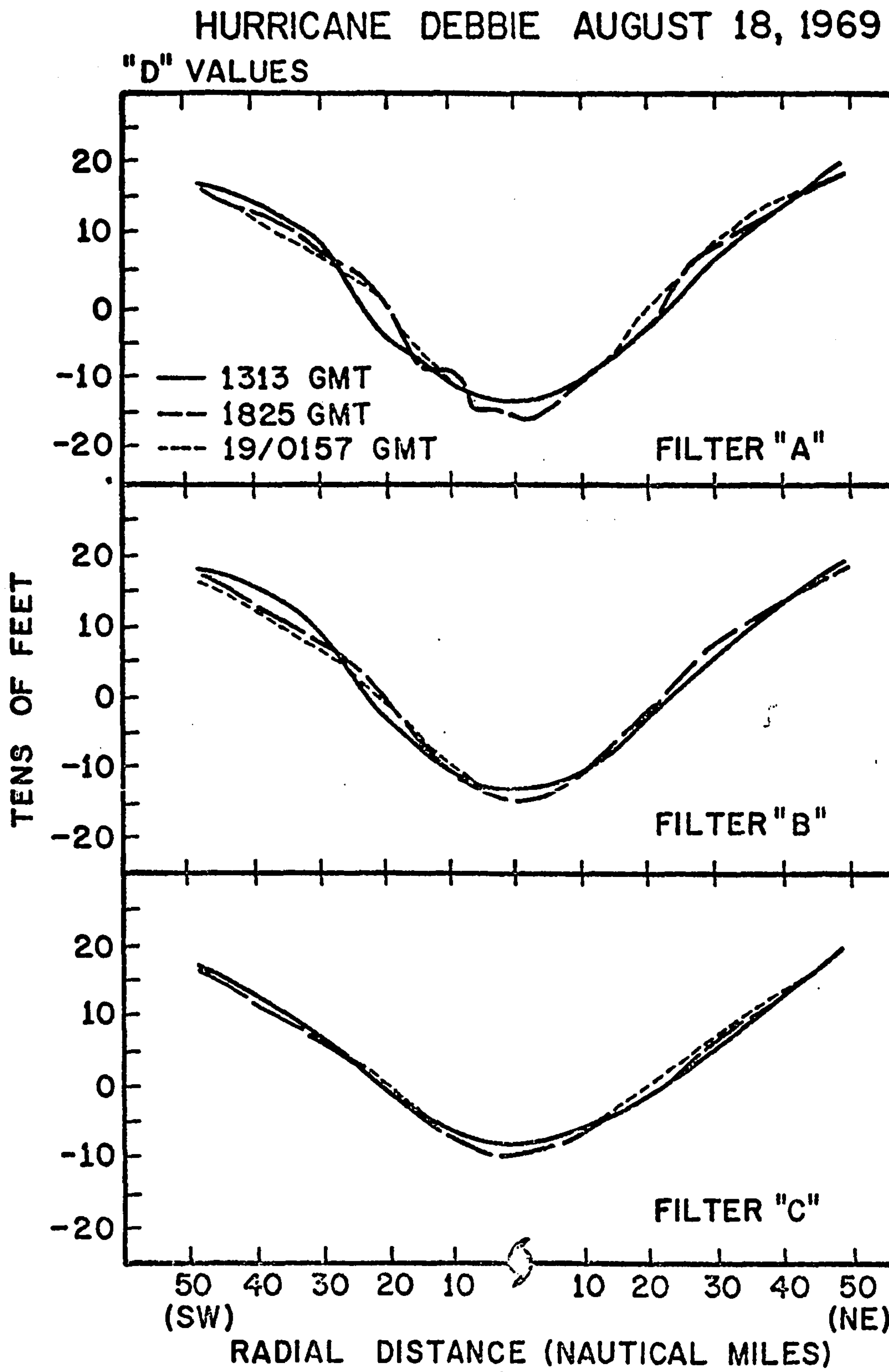

Fig. 19. Profiles of "D" values resulting from application of filters "A", "B", and "C" to the observed data for the periods of before, during, and after the series of seeding events.

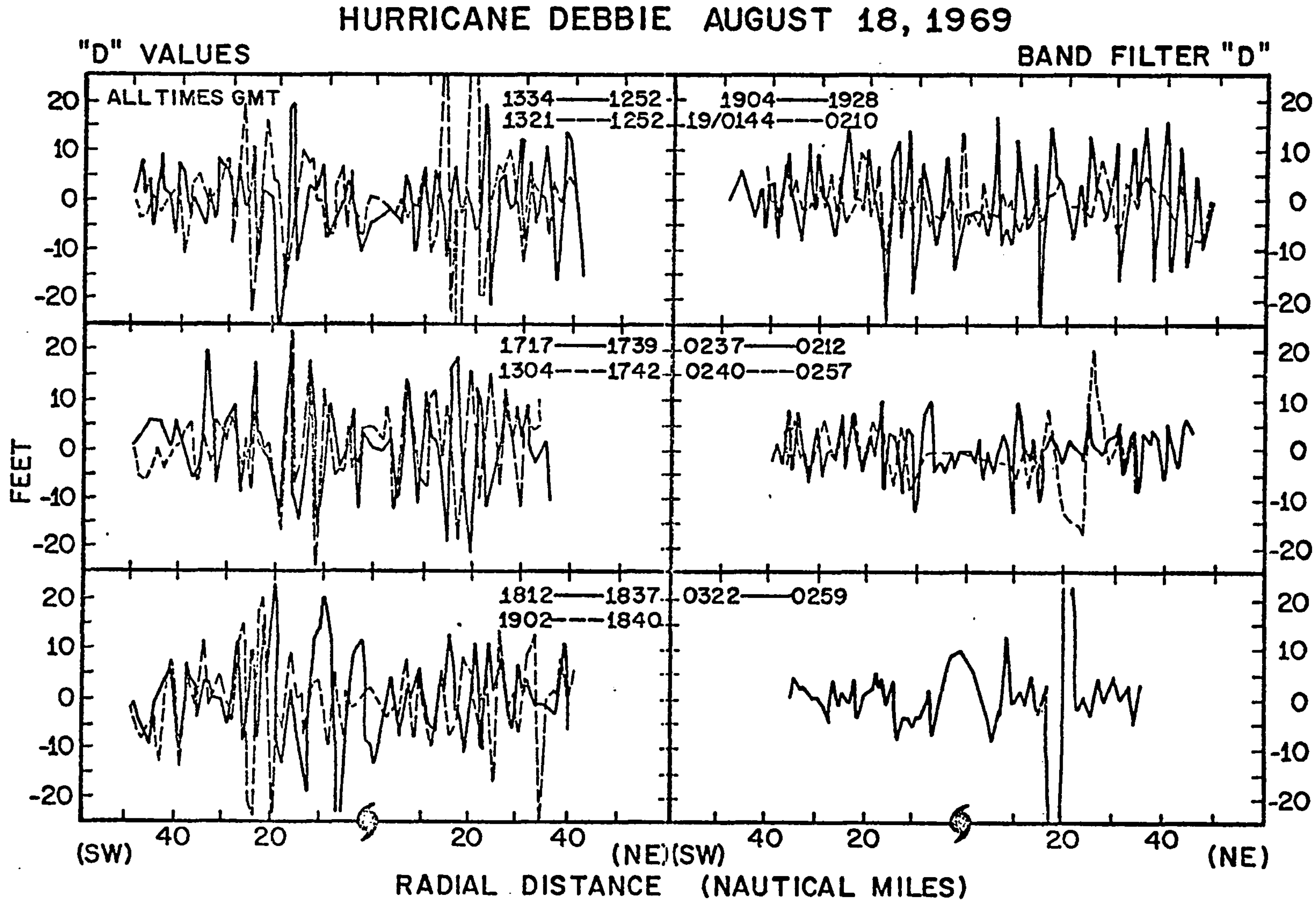

Fig. 20. Profiles of "D" values resulting from application of band filter "D" to the observed data (~ cumulonimbus scale).

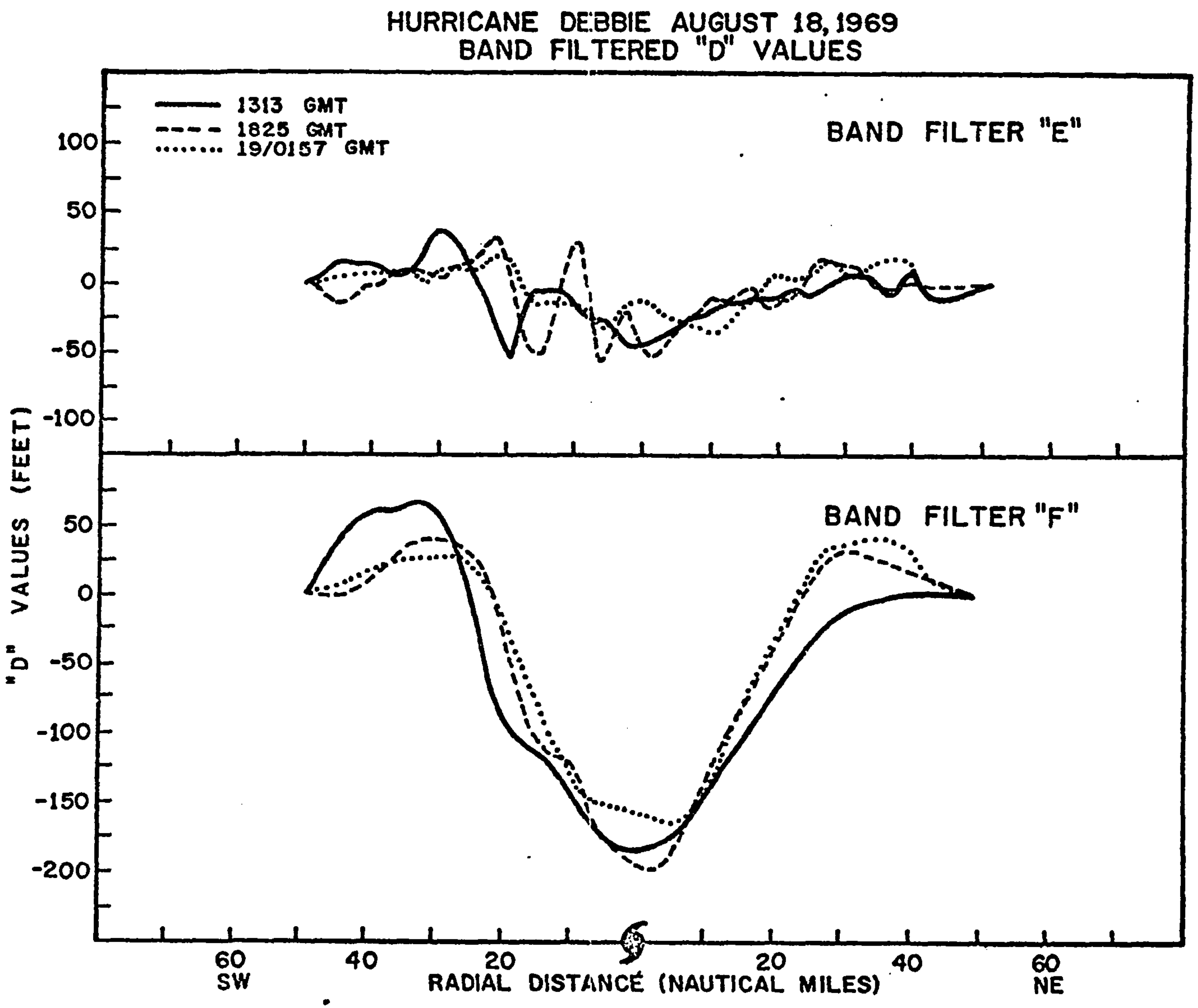

Fig. 21. Profiles of "D" values resulting from application of band filters "E" and "F" (~ rainband and eyewall scales respectively) to the observed data.

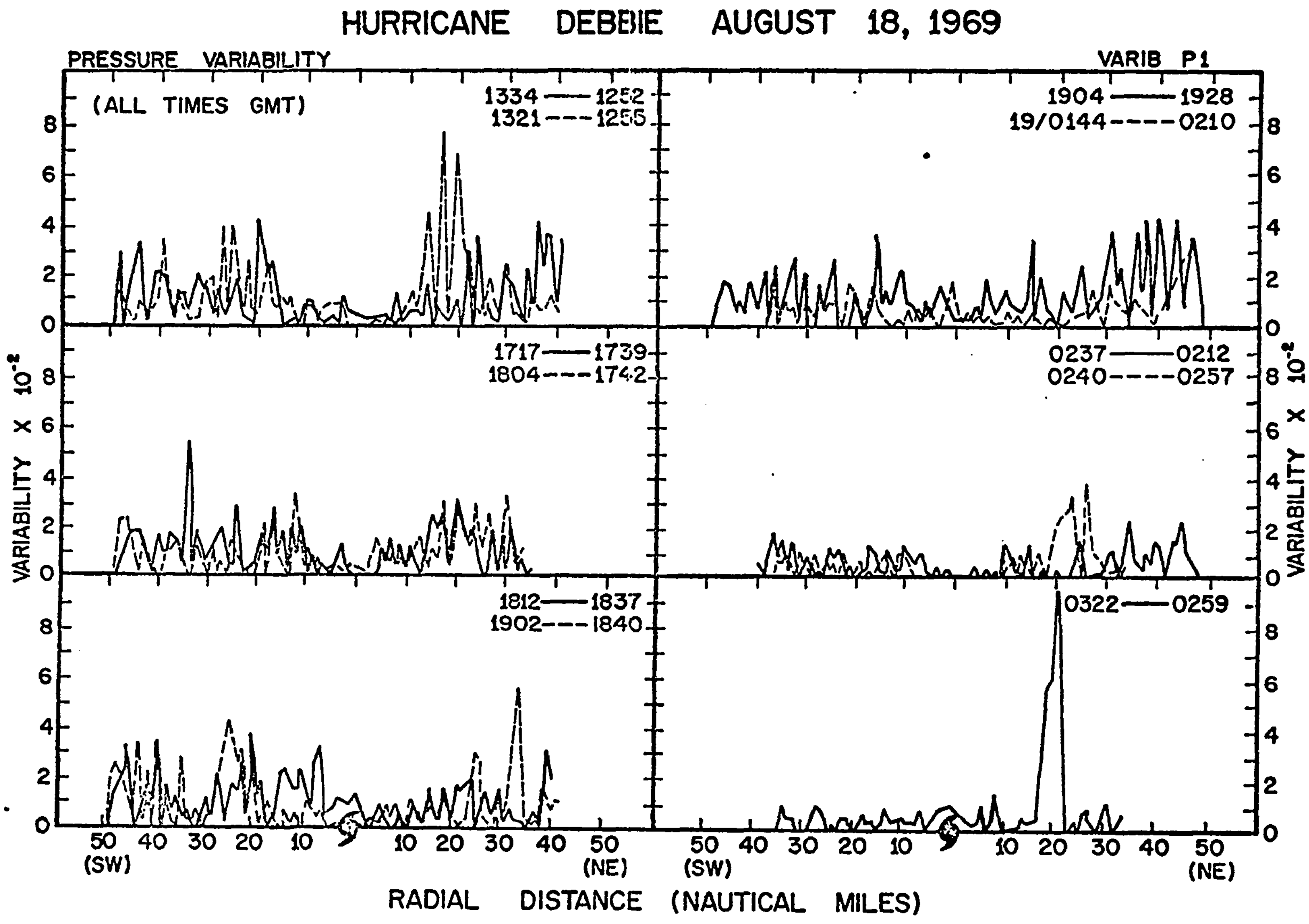

Fig. 22. Pressure variability profiles for approximate cumulonimbus scale motion.

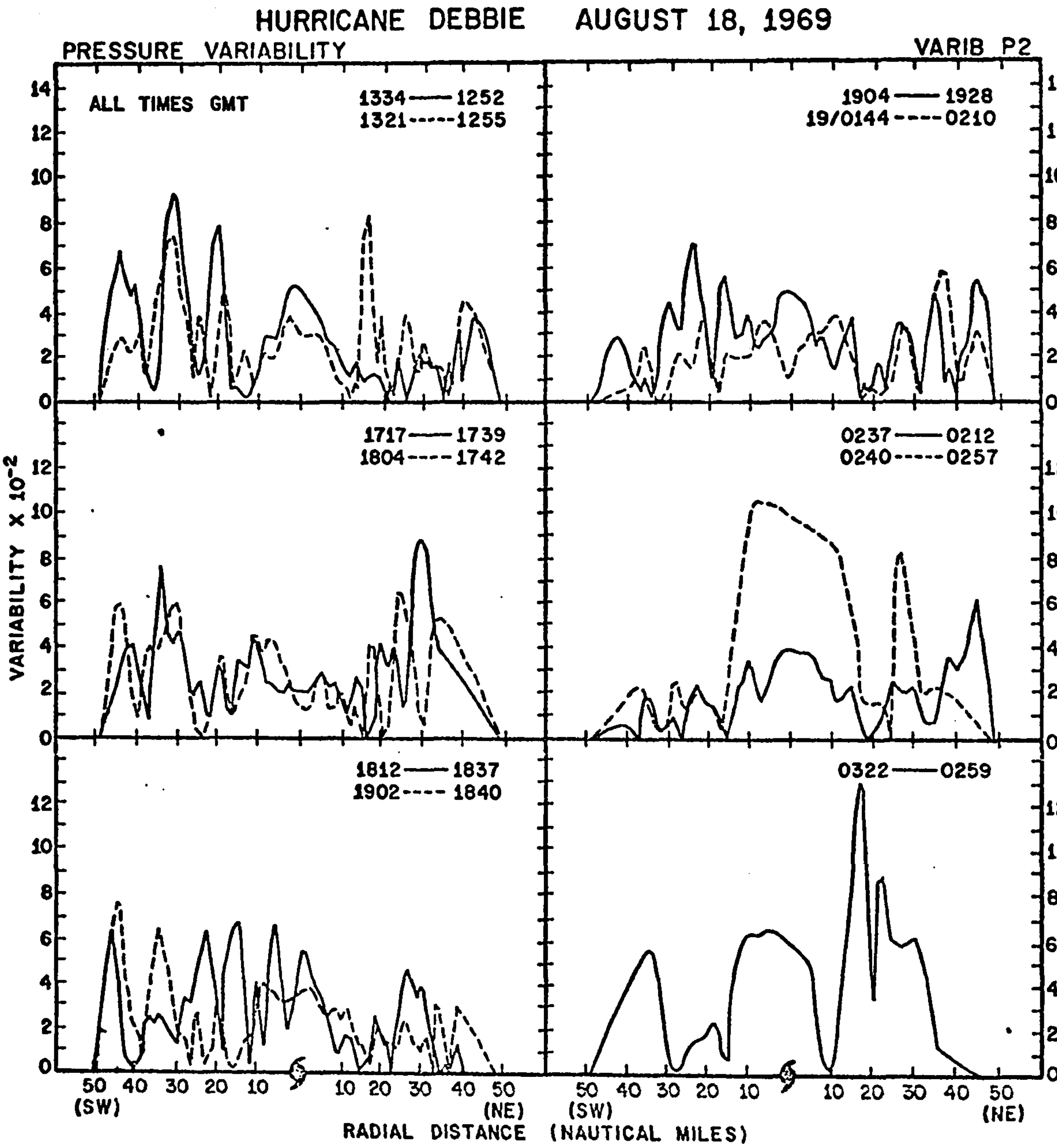

Fig. 23. Pressure variability profiles for approximate rainband scale motion.

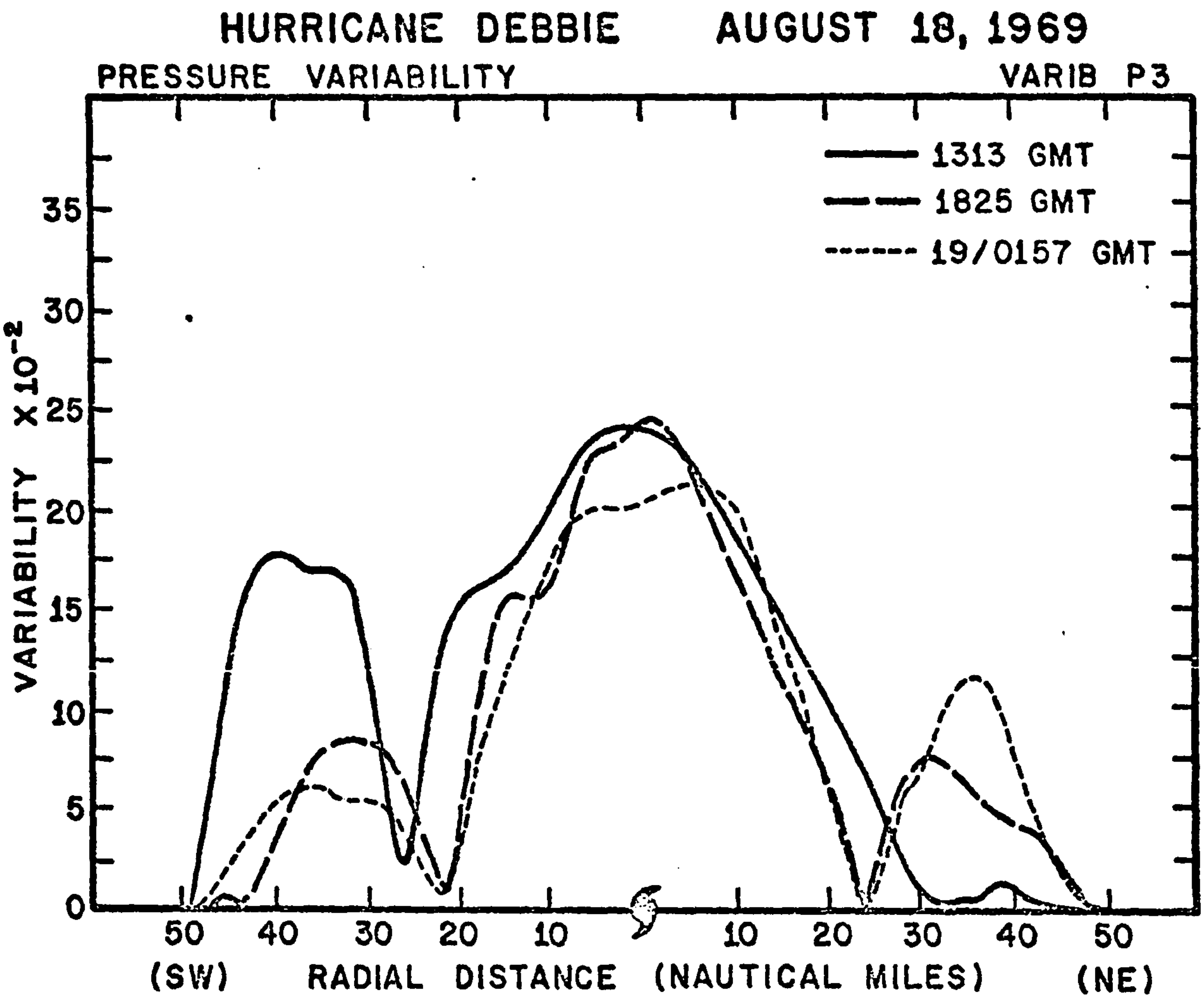

Fig. 24. Pressure variability profiles for approximate eyewall scale motion.

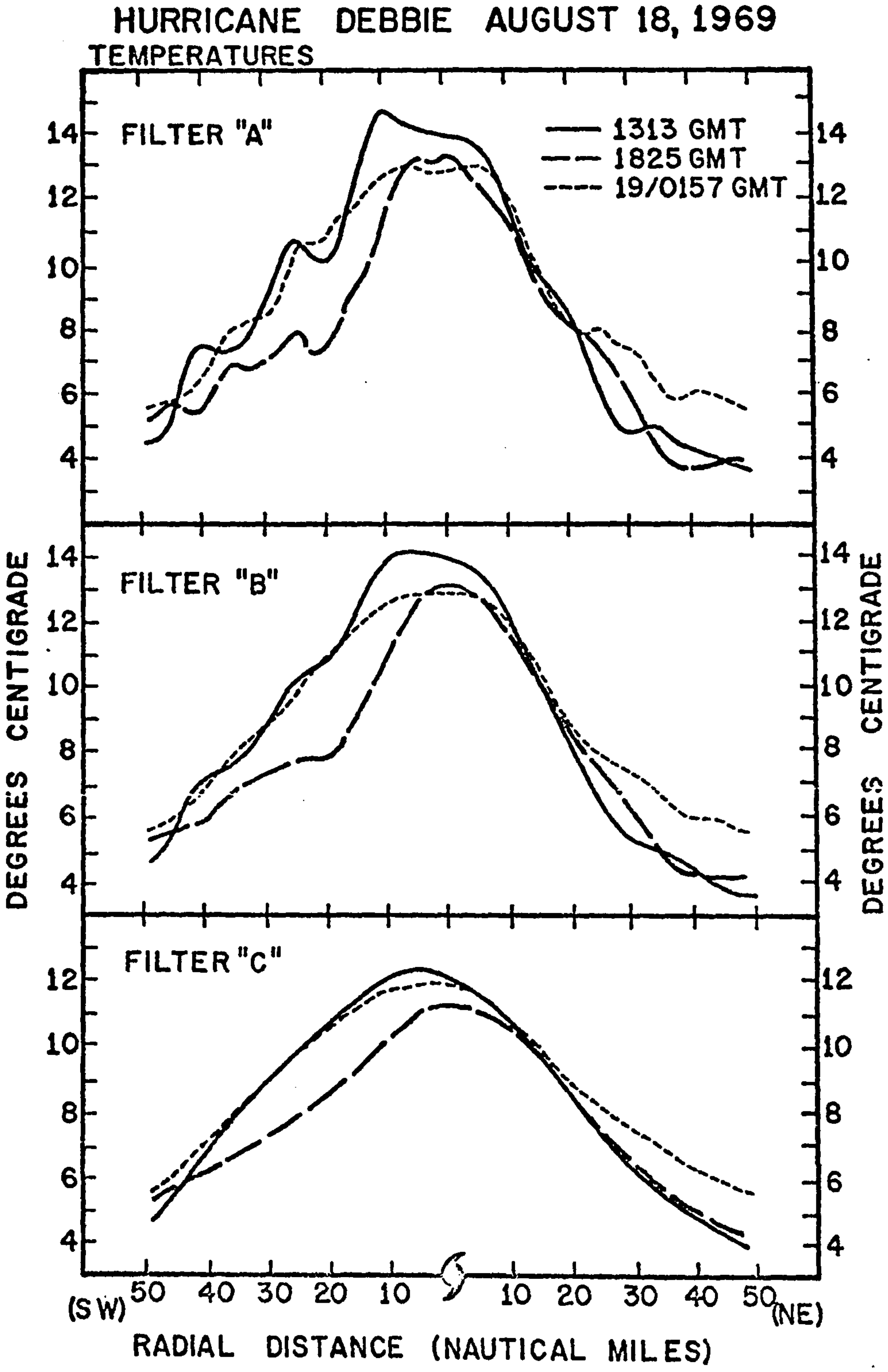

Fig. 25. Temperature profiles obtained by application of filters "A", "B", and "C" for the periods of before, during and after the series of seeding events.

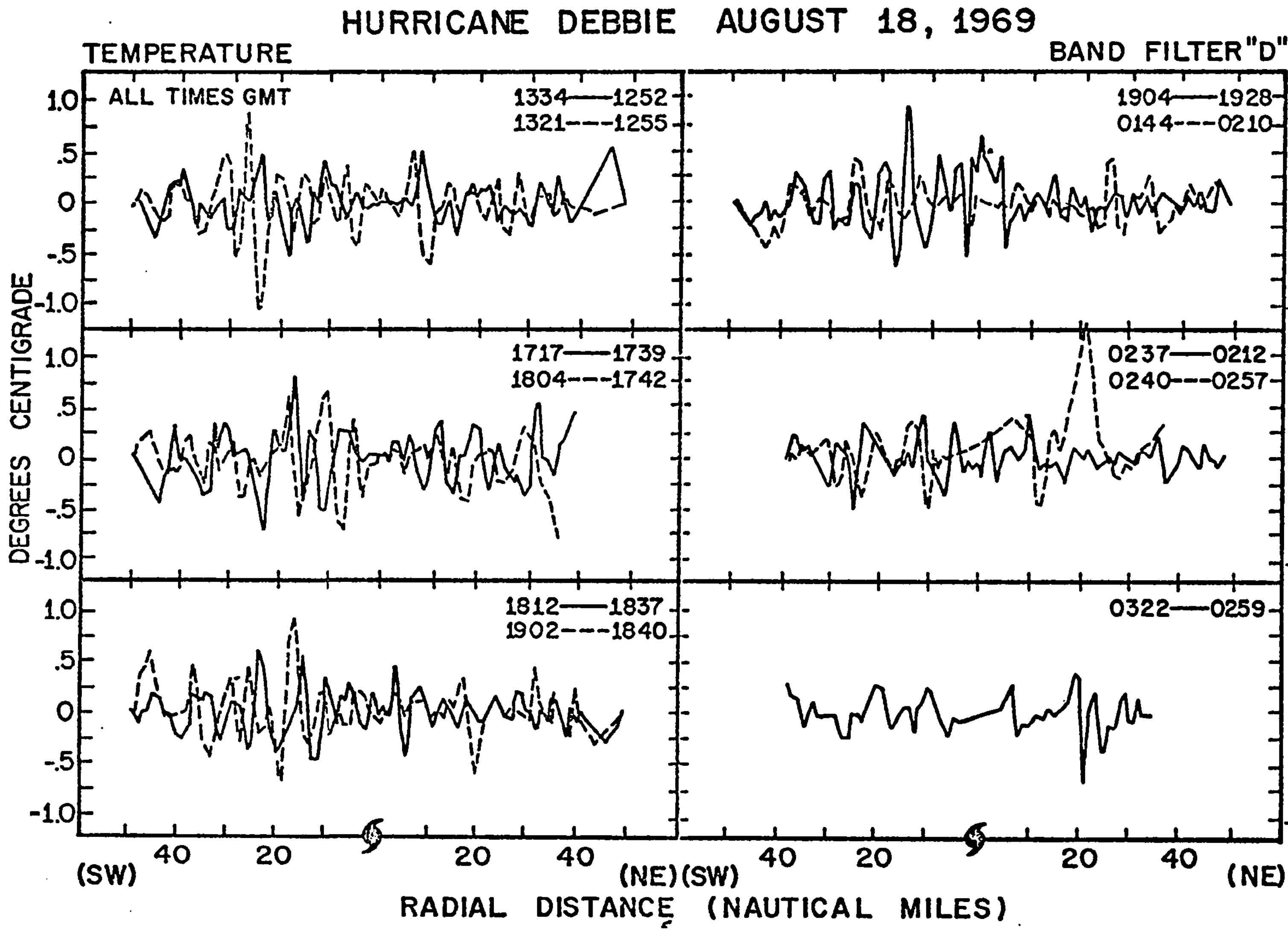

Fig. 26. Temperature profiles resulting from application of band filter "D" (~ cumulonimbus scale) to the observed data.

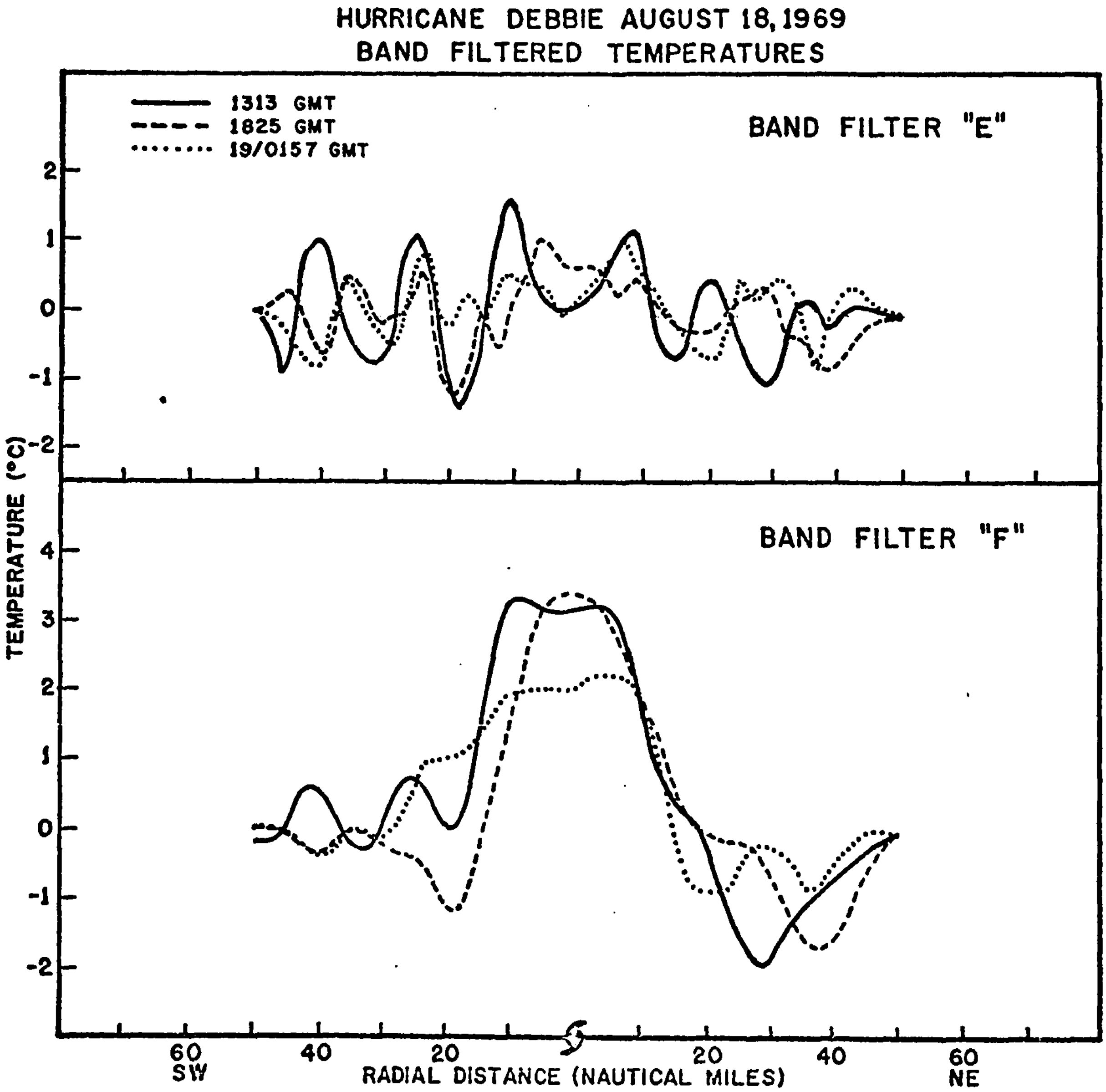

Fig. 27. Temperature profiles resulting from application of band filters "E" and "F" (~ rainband and eyewall scales respectively) to the observed data.

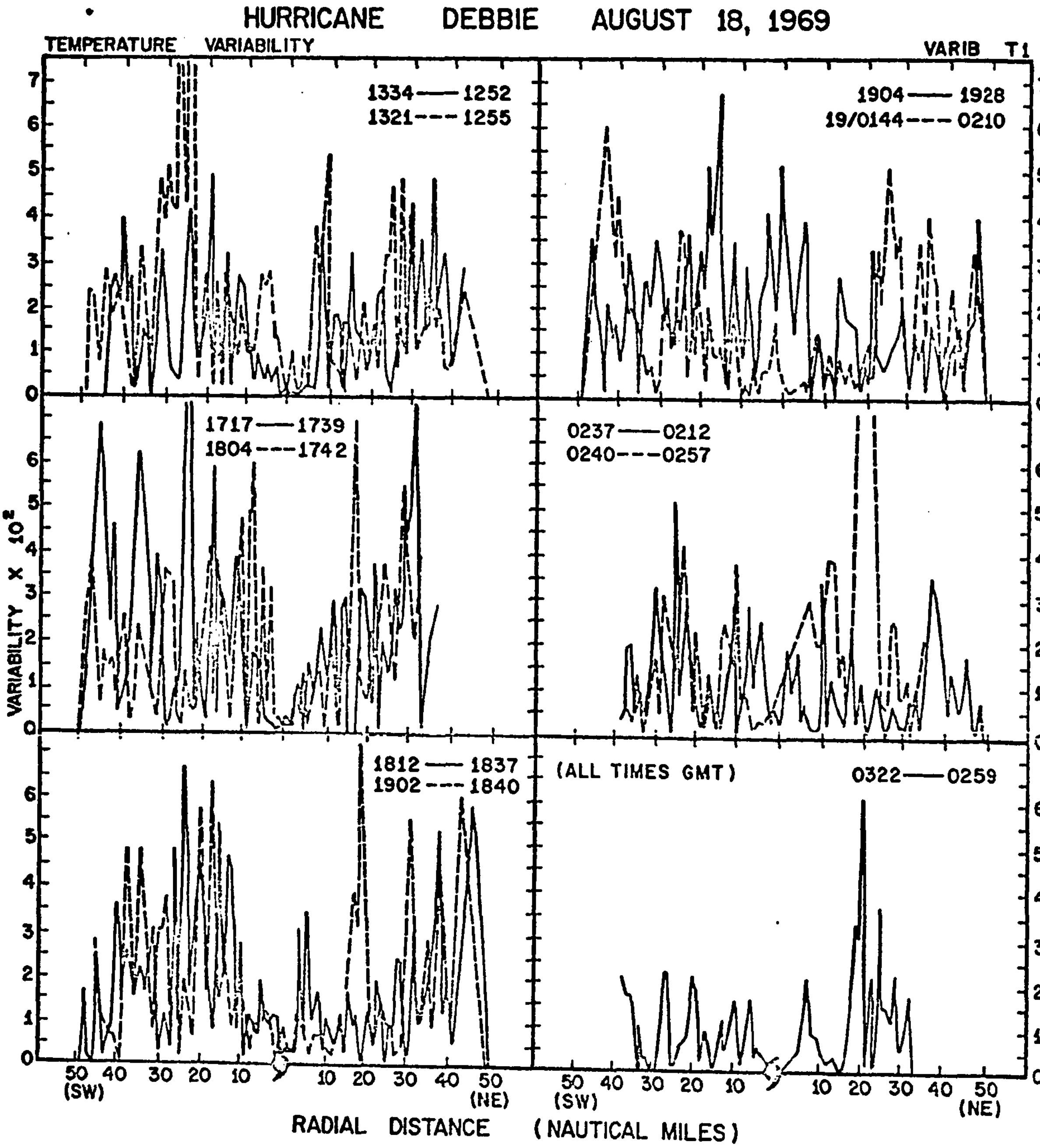

Fig. 28. Temperature variability profiles for approximate cumulonimbus scale motion.

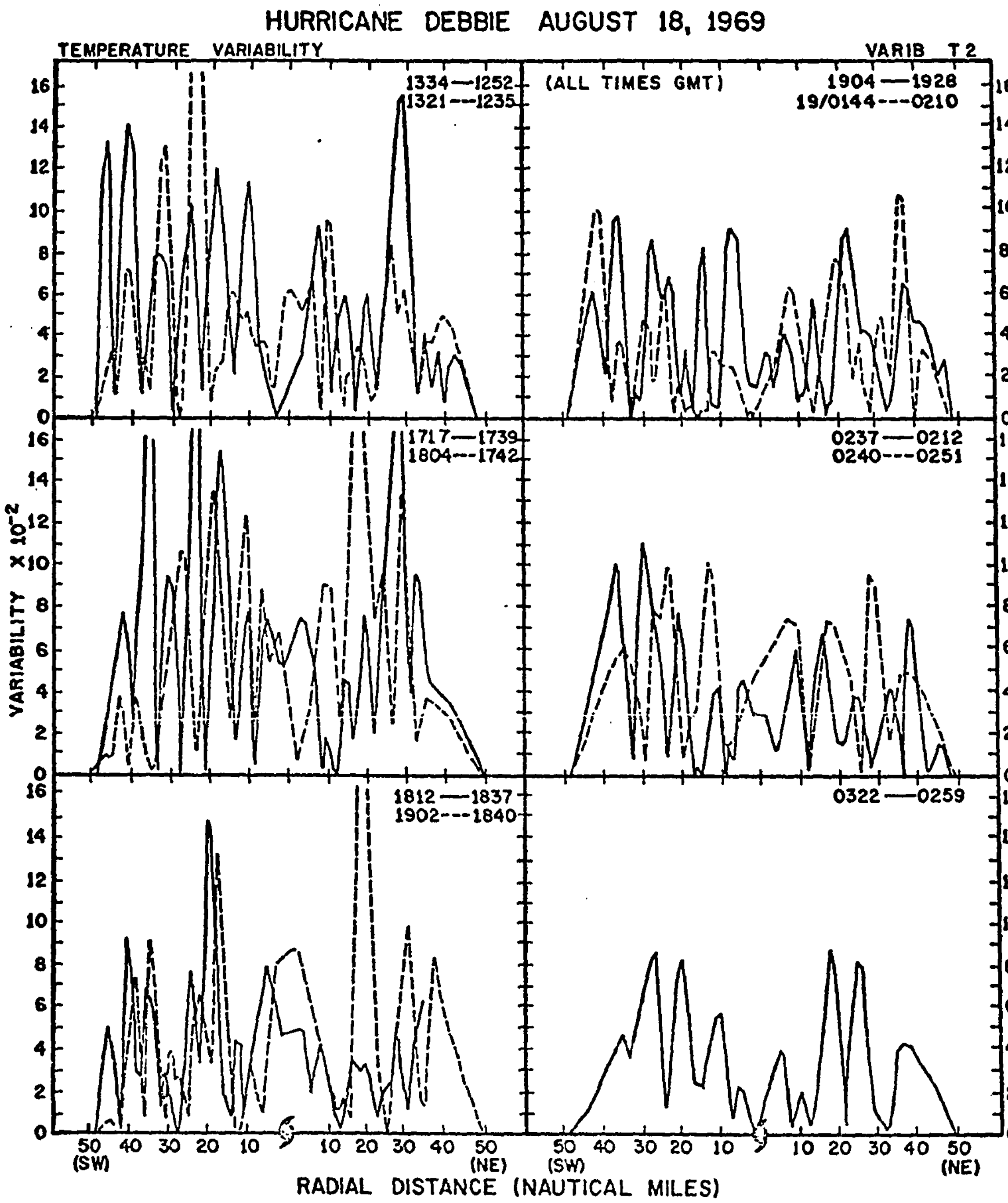

Fig. 29. Temperature variability profiles for approximate rainband scale motion.

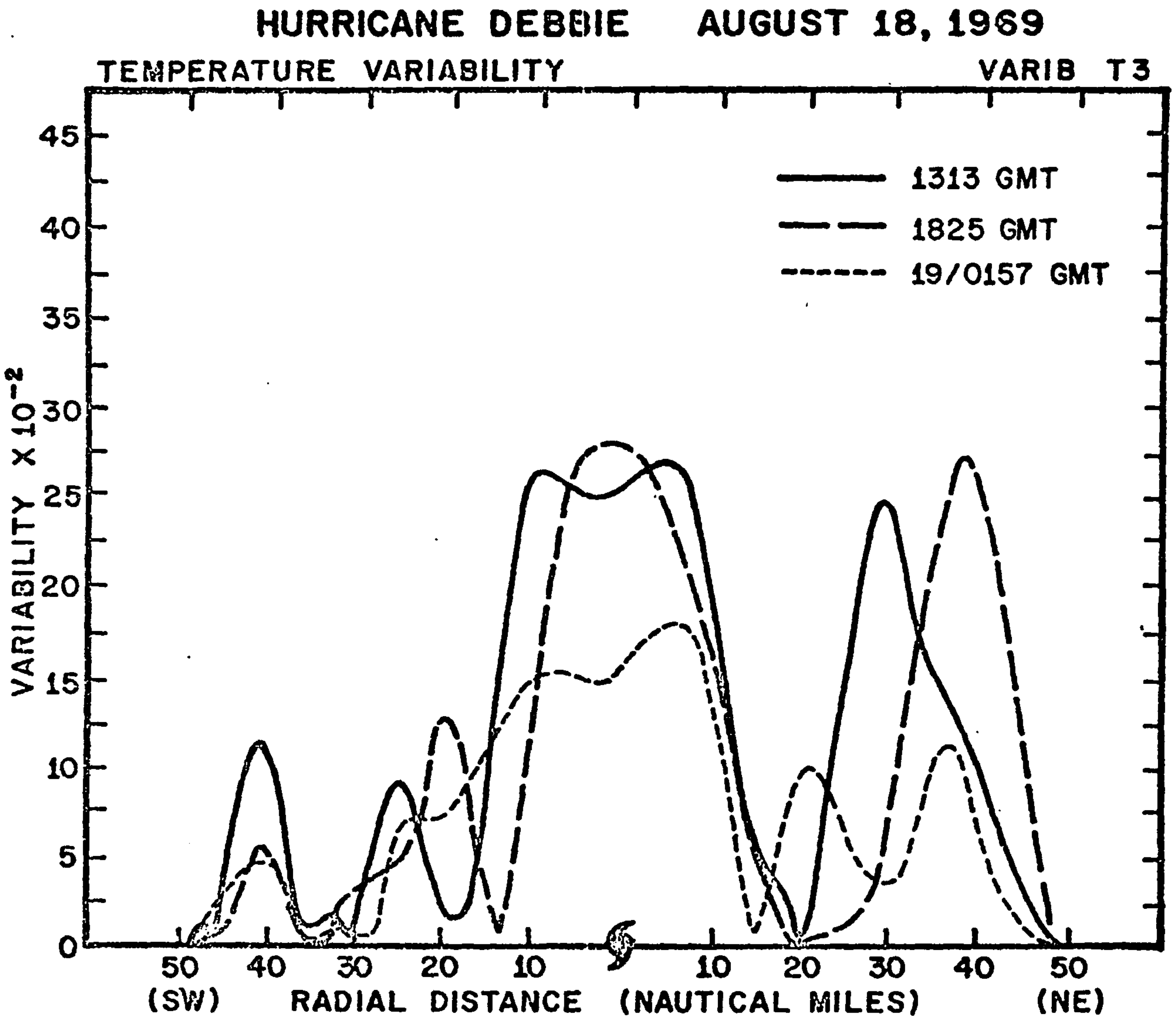

Fig. 30. Temperature variability profiles for approximate eyewall scale motion.

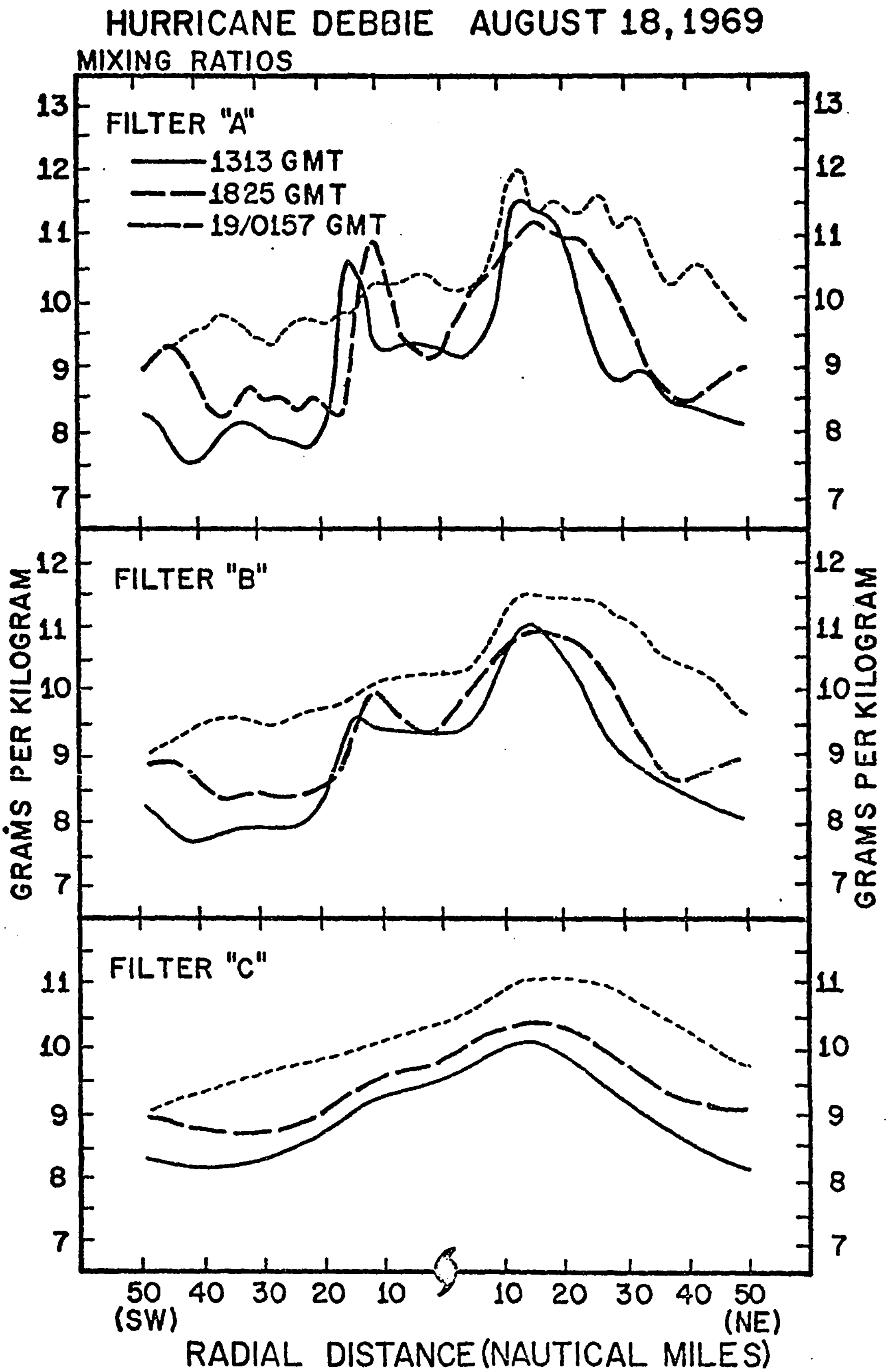

Fig. 31. Mixing ratio profiles resulting from application of filters "A", "B", and "C" to the observed data for the periods of before, during, and after the series of seeding events.

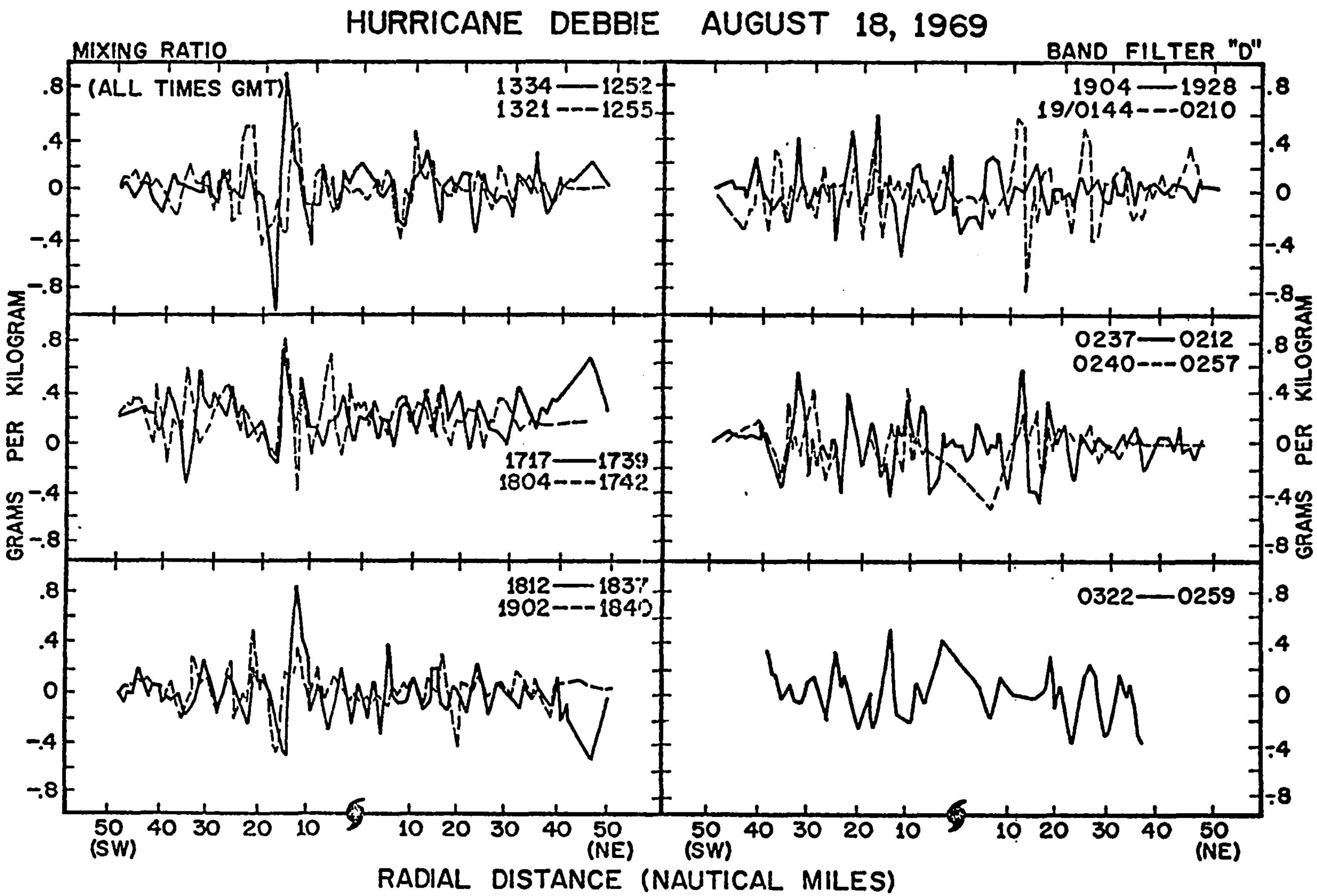

Fig. 32. Mixing ratio profiles resulting from application of band filter "D" to observed data (~ cumulonimbus scale).

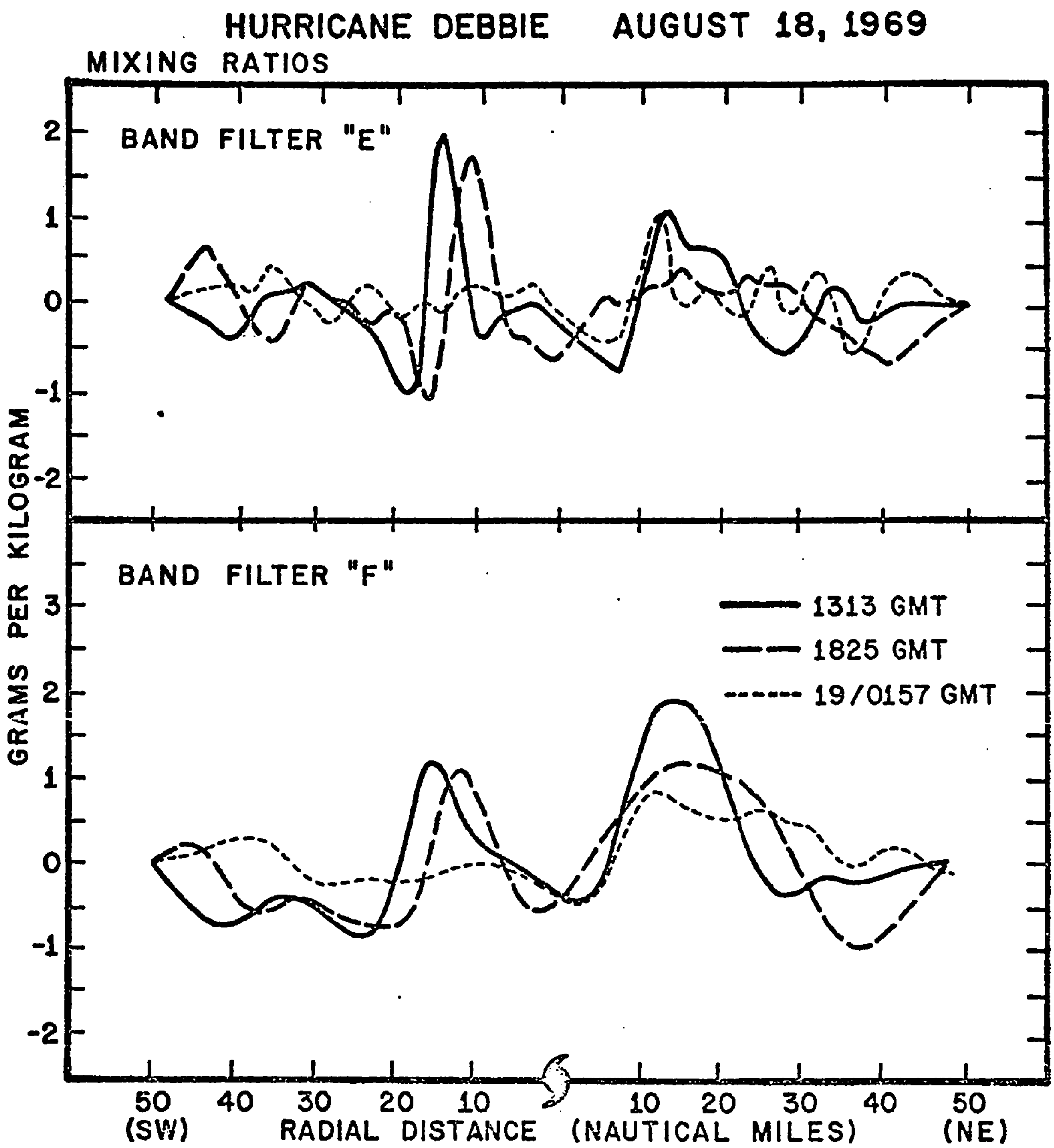

Fig. 33. Mixing ratio profiles resulting from application of band filters "E", and "F" (~ rainband and eyewall scales respectively) to the observed data.

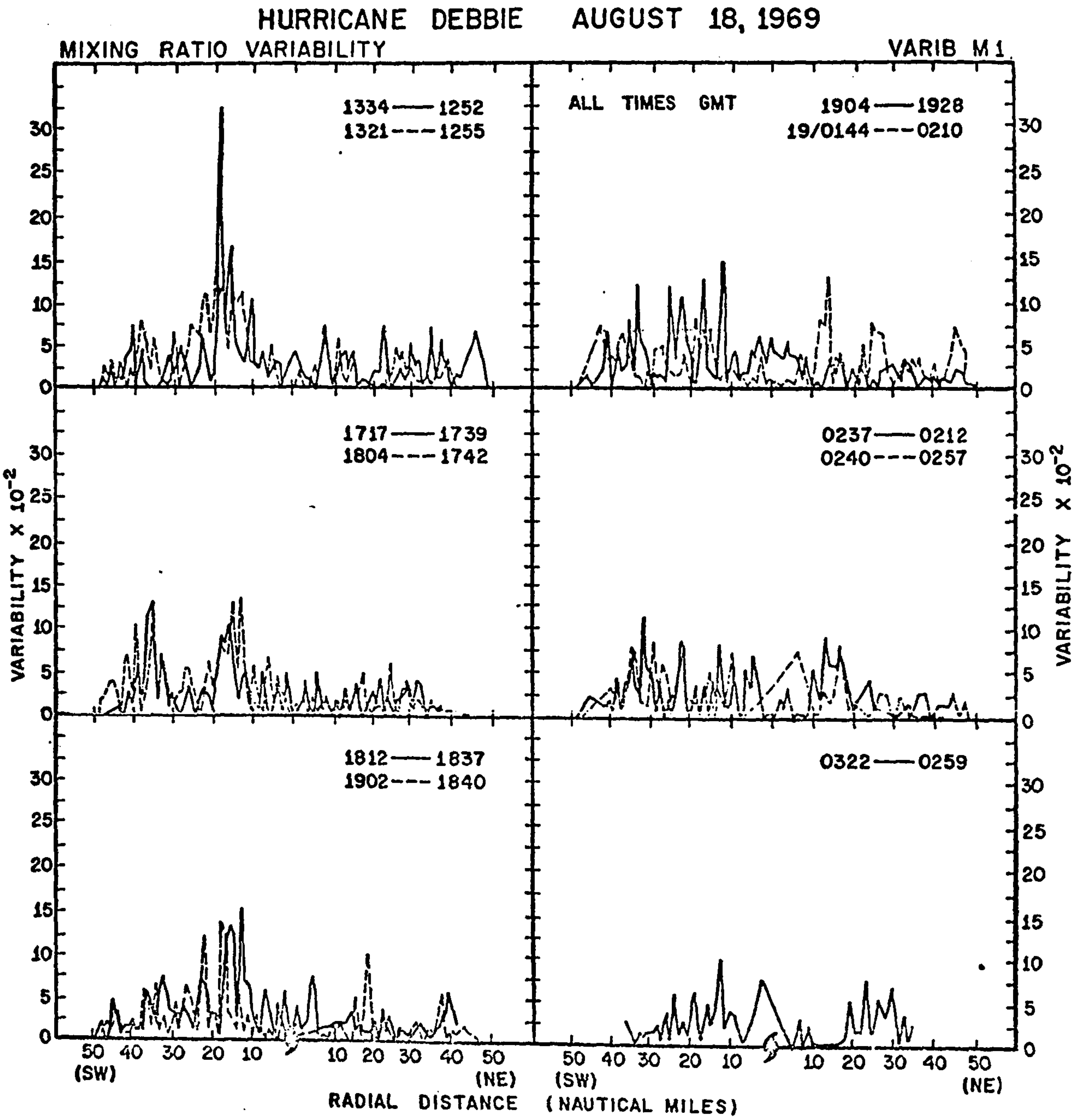

Fig. 34. Moisture variability profiles for approximate cumulonimbus scale motion.

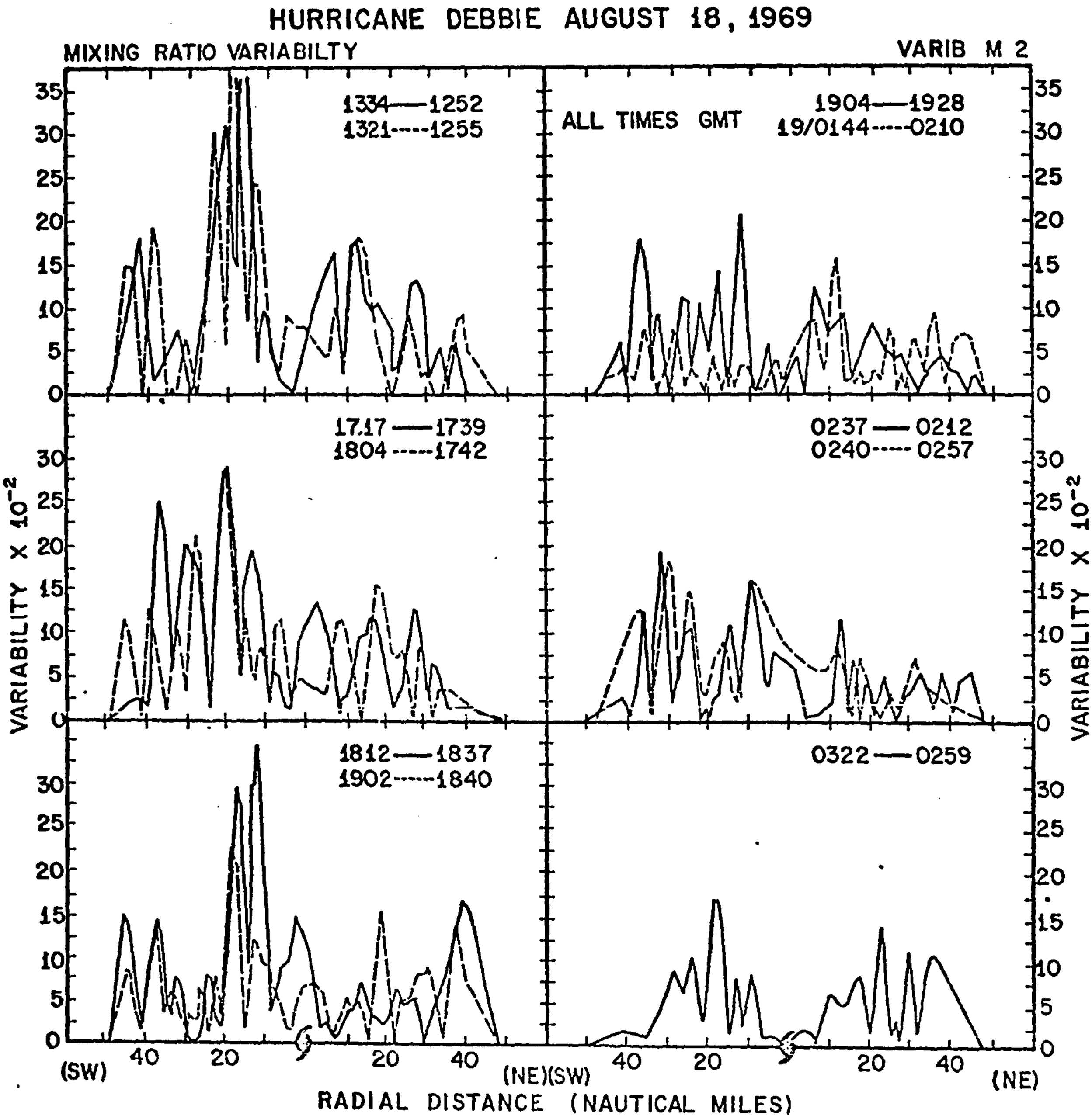

Fig. 35. Moisture variability profiles for approximate rainband scale motion.

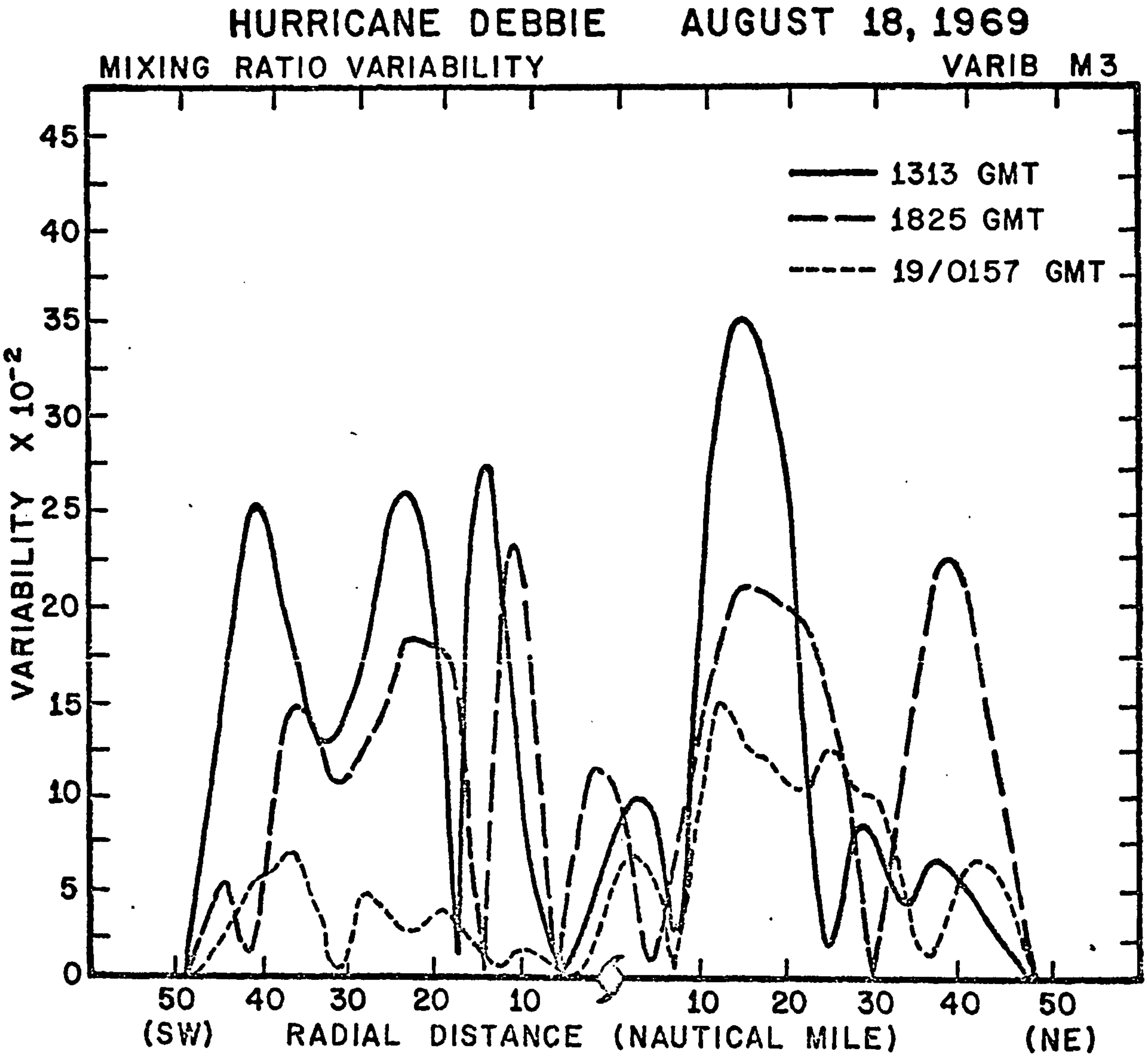

Fig. 36. Moisture variability profiles for approximate eyewall scale motion.

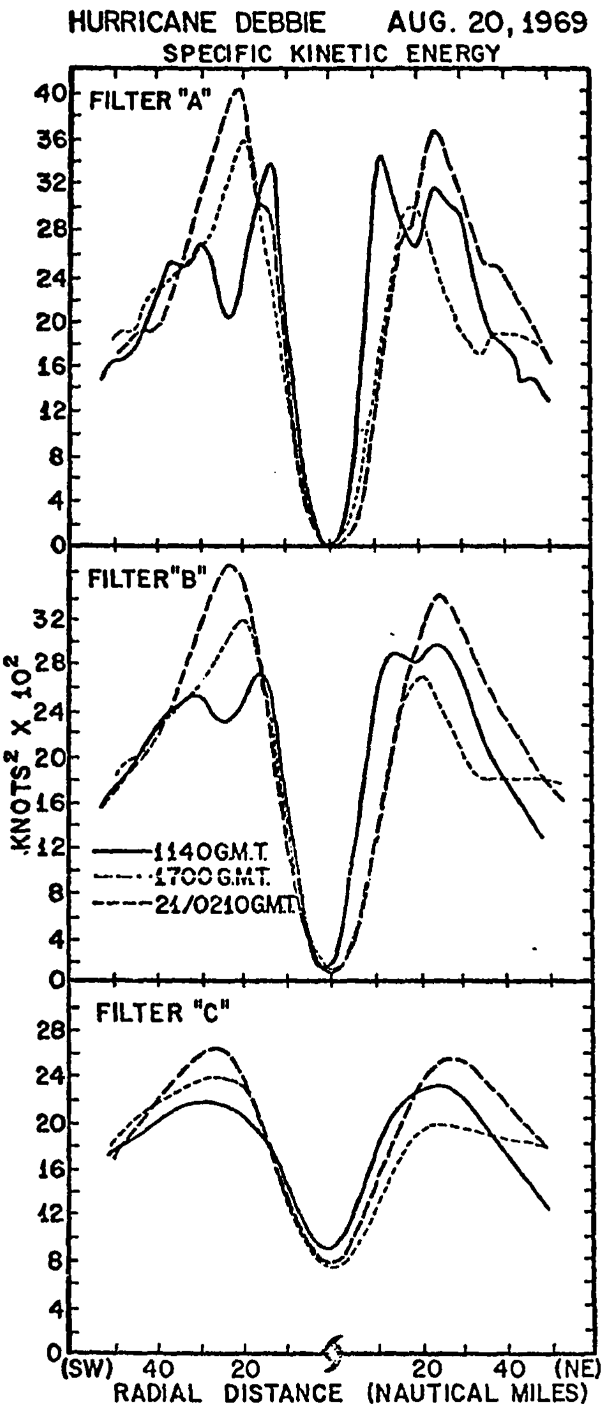

Fig. 37. Kinetic energy profiles for the left and right (SW-NE) sides of the storm, resulting from application of filters "A", "B", and "C" to the observed data

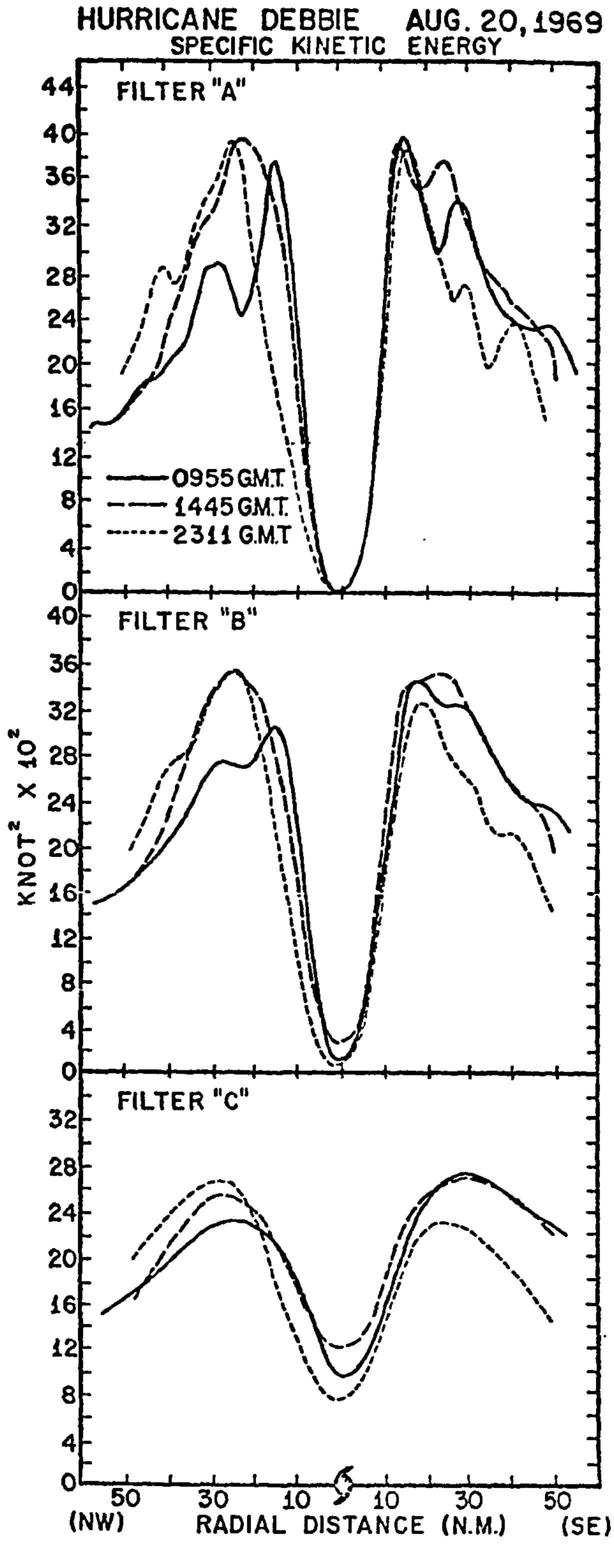

Fig. 38. Kinetic energy profiles for the front and rear (NW-SE) portions of the storm, resulting from application of filters "A", "B", and "C" to the observed data.

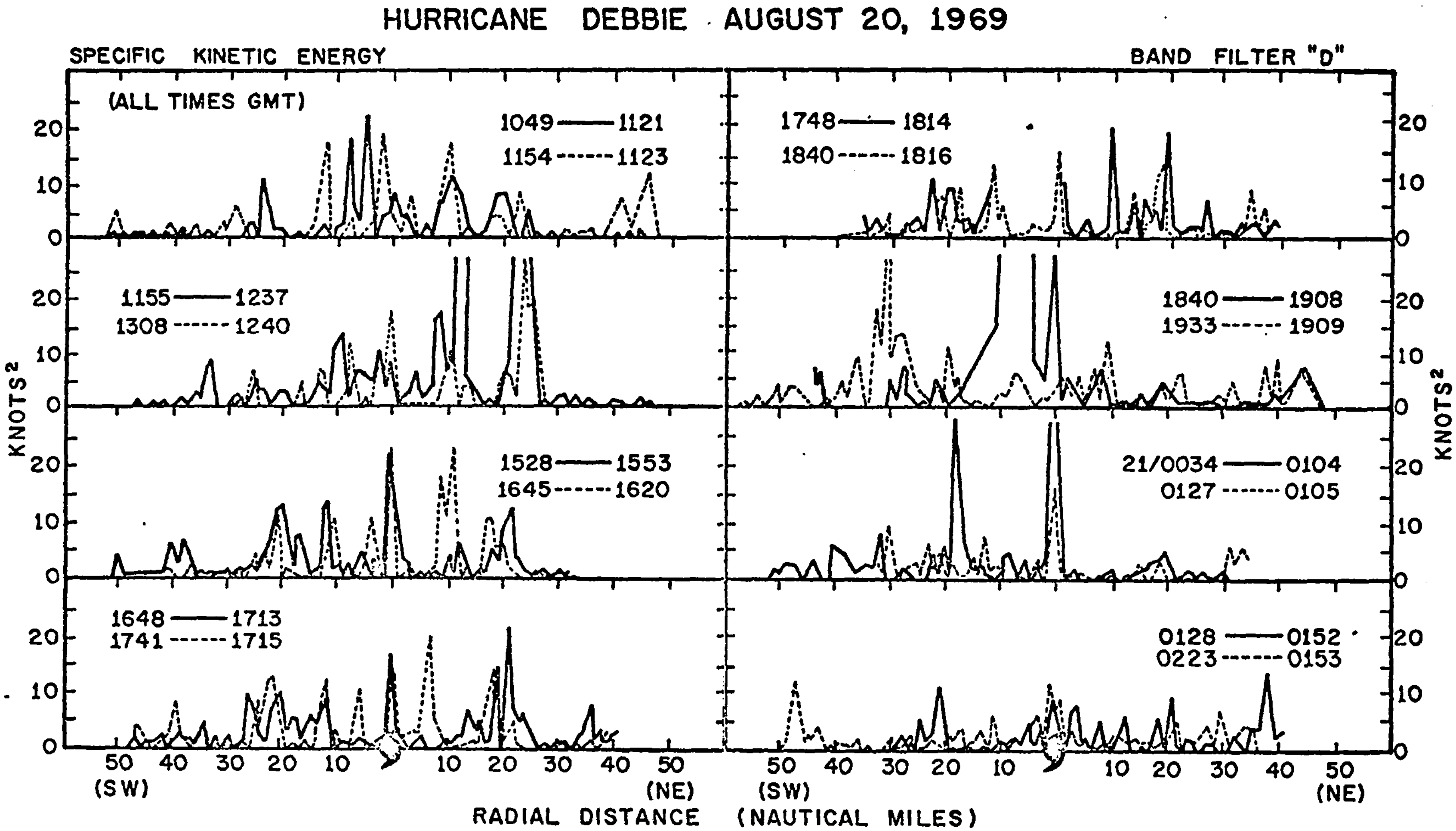

Fig. 39. Kinetic energy profiles resulting from application of band filter "D" (~ cumulonimbus scale) to the data recorded in the southwest and northeast portions of the storm.

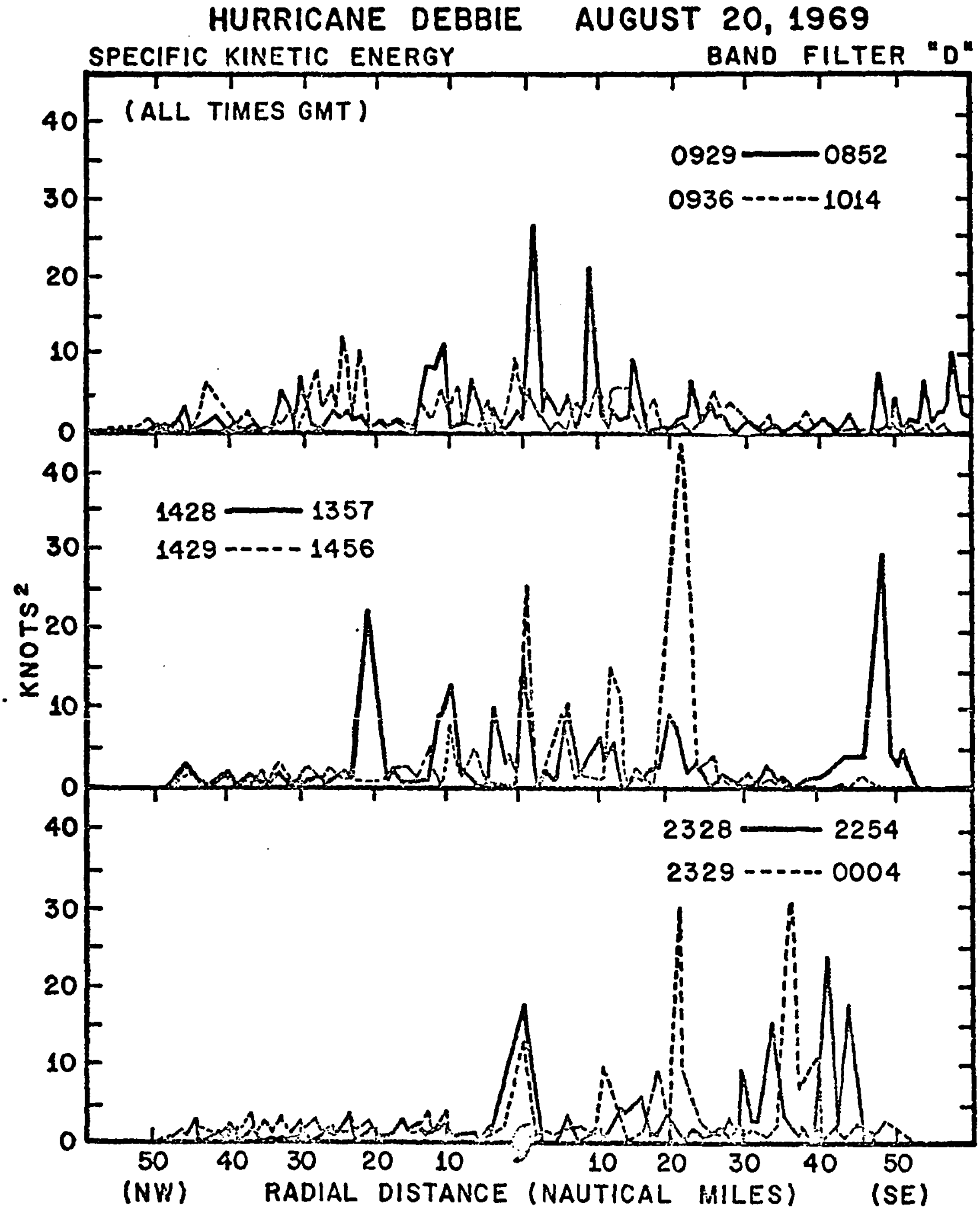

Fig. 40. Kinetic energy profiles for the front and rear (NW-SE) portions of the storm resulting from application of band filter "D" (~ cumulonimbus scale) to the observed data.

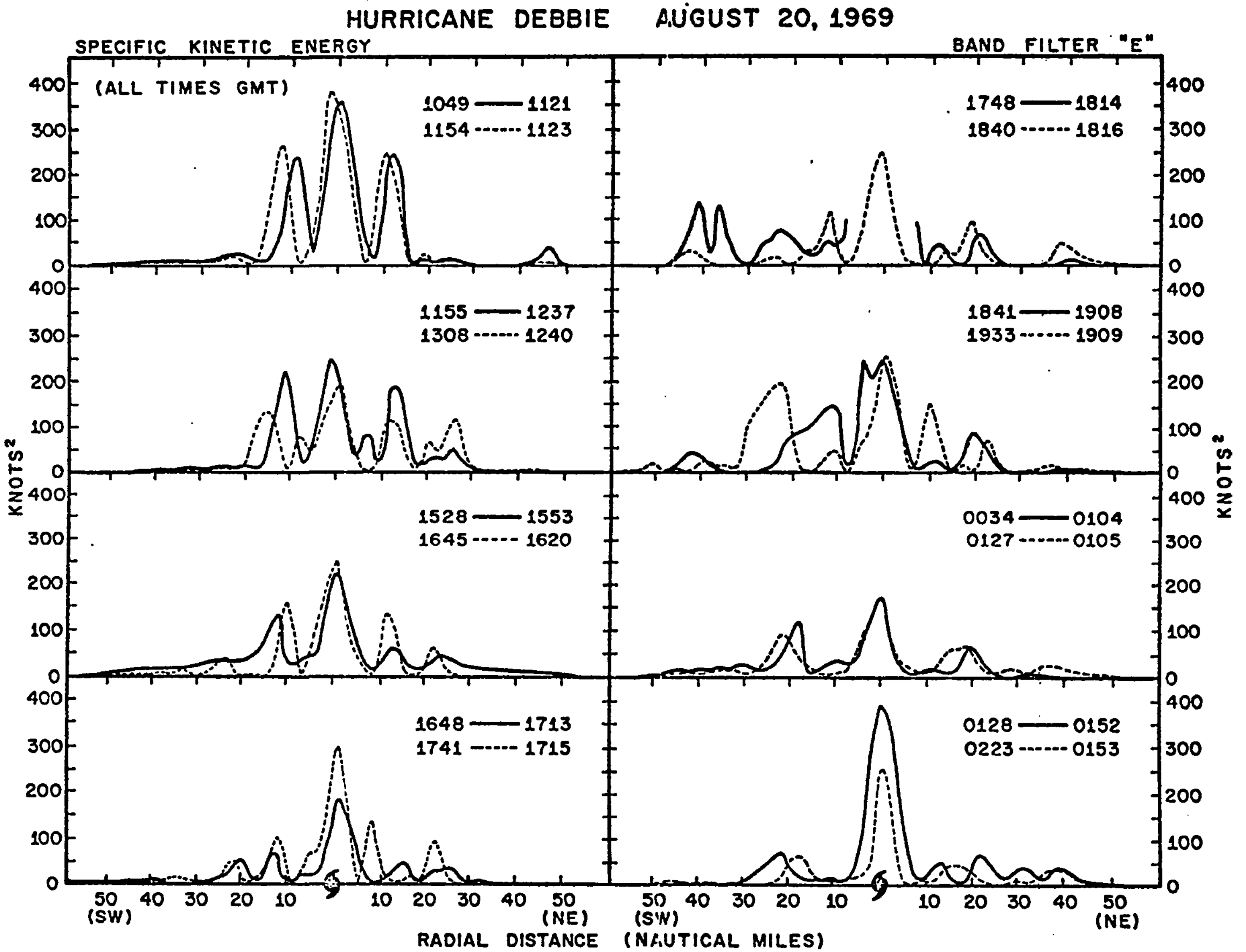

Fig. 41. Kinetic energy profiles for the left and right (SW-NE) sides of the storm resulting from application of band filter "E" (~ rainband scale) to the observed data.

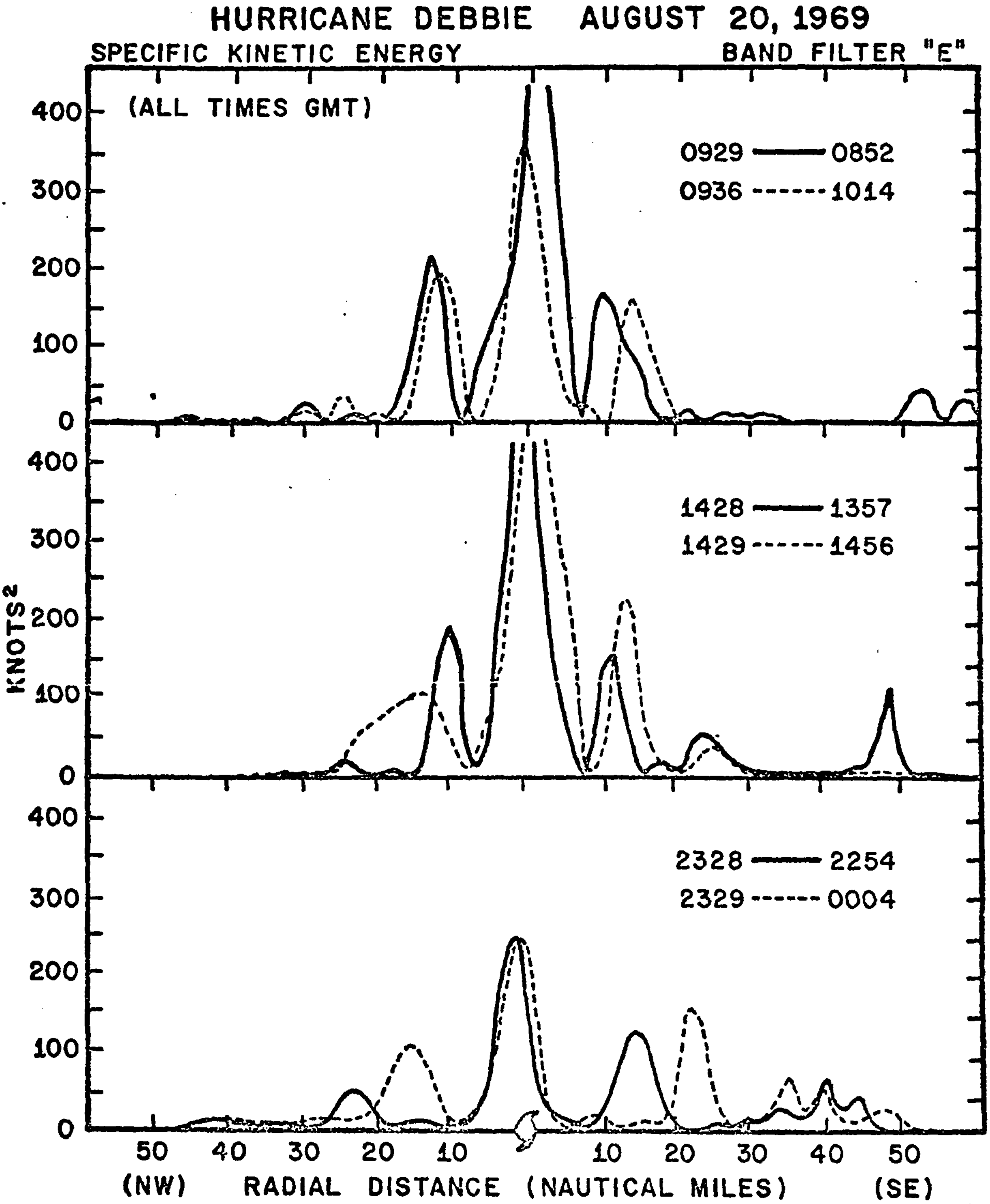

Fig. 42. Kinetic energy profiles for the front and rear (NW-SE) portions of the storm, resulting from application of band filter "E" (~ rainband scale) to the observed data.

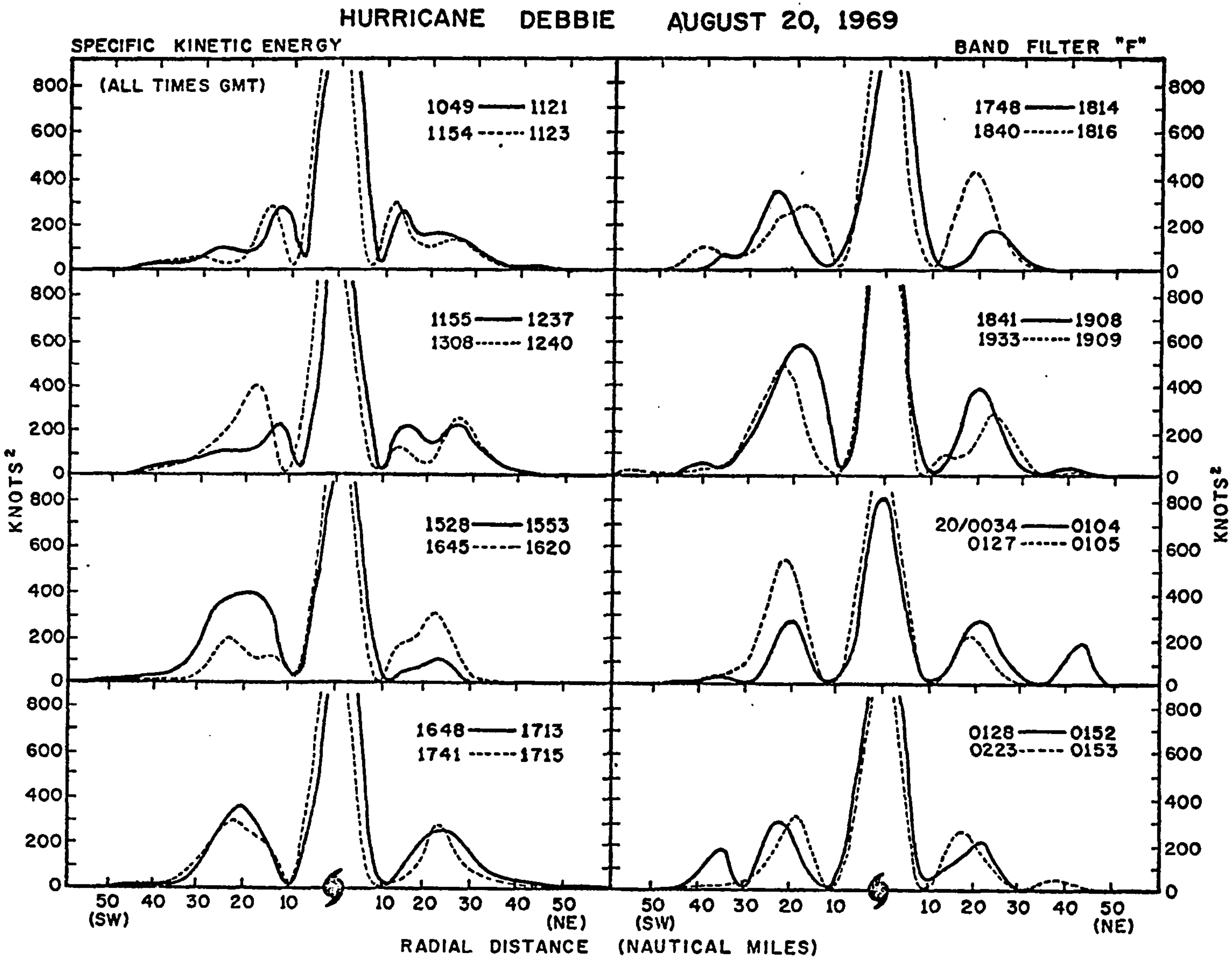

Fig. 43. Kinetic energy profiles for the left and right (SW-NE) sides of the storm resulting from application of band filter "F" (~ eyewall scale) to the observed data.

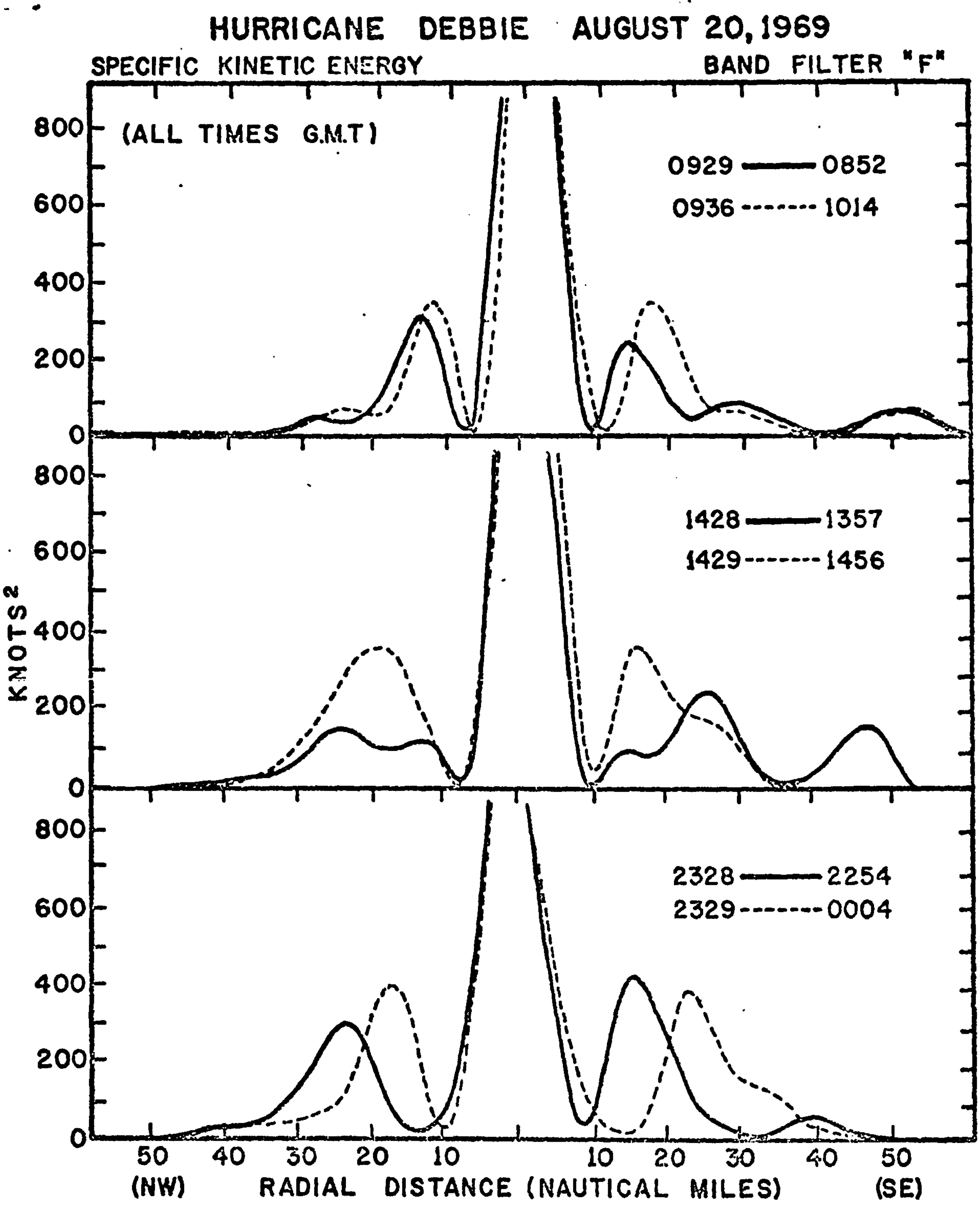

Fig. 44. Kinetic energy profiles for the front and rear (NW-SE) portions of the storm, resulting from application of band filter "F" (~ eyewall scale) to the observed data.

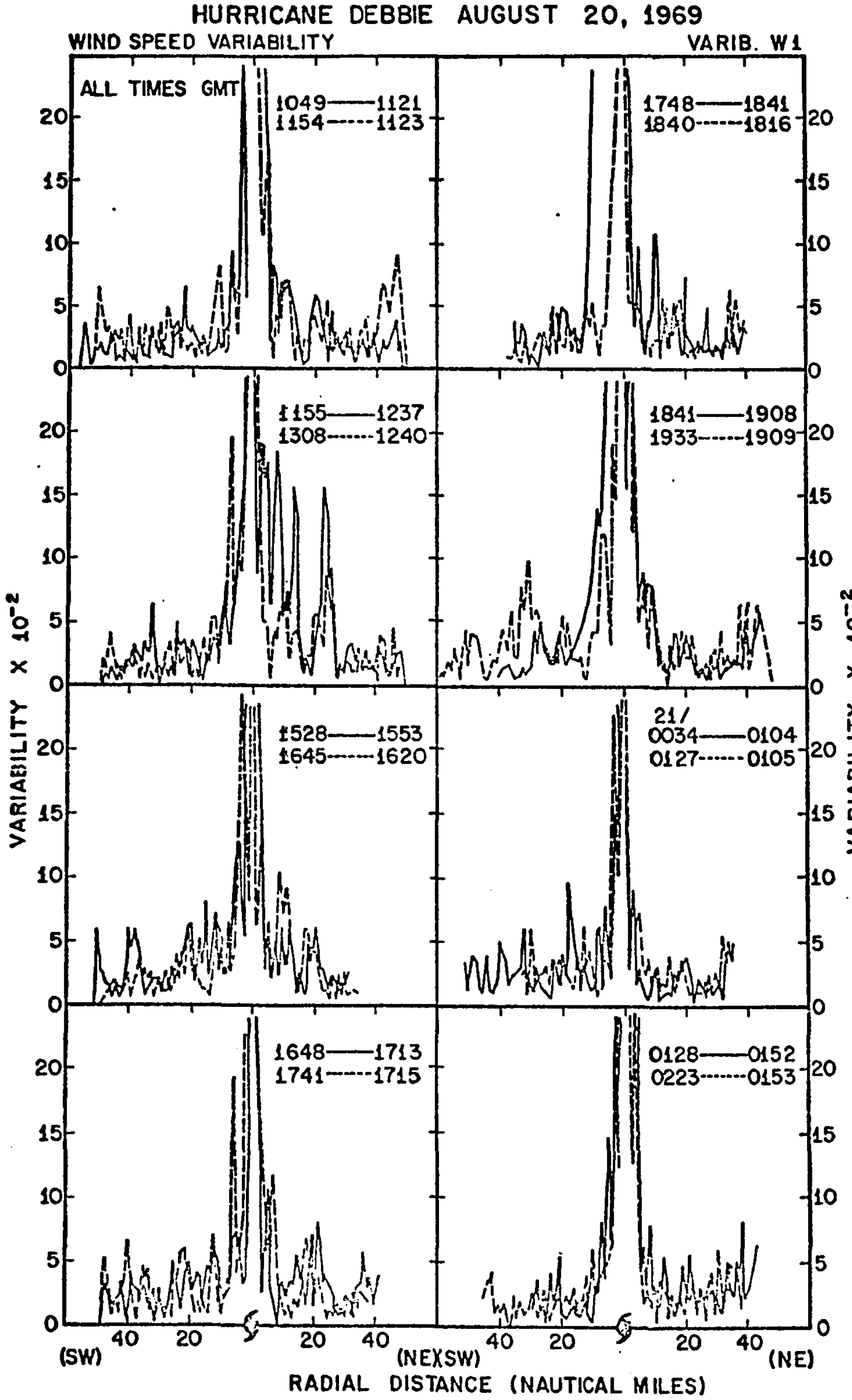

Fig. 45. Relative wind speed variability profiles for approximate cumulonimbus scale motion.

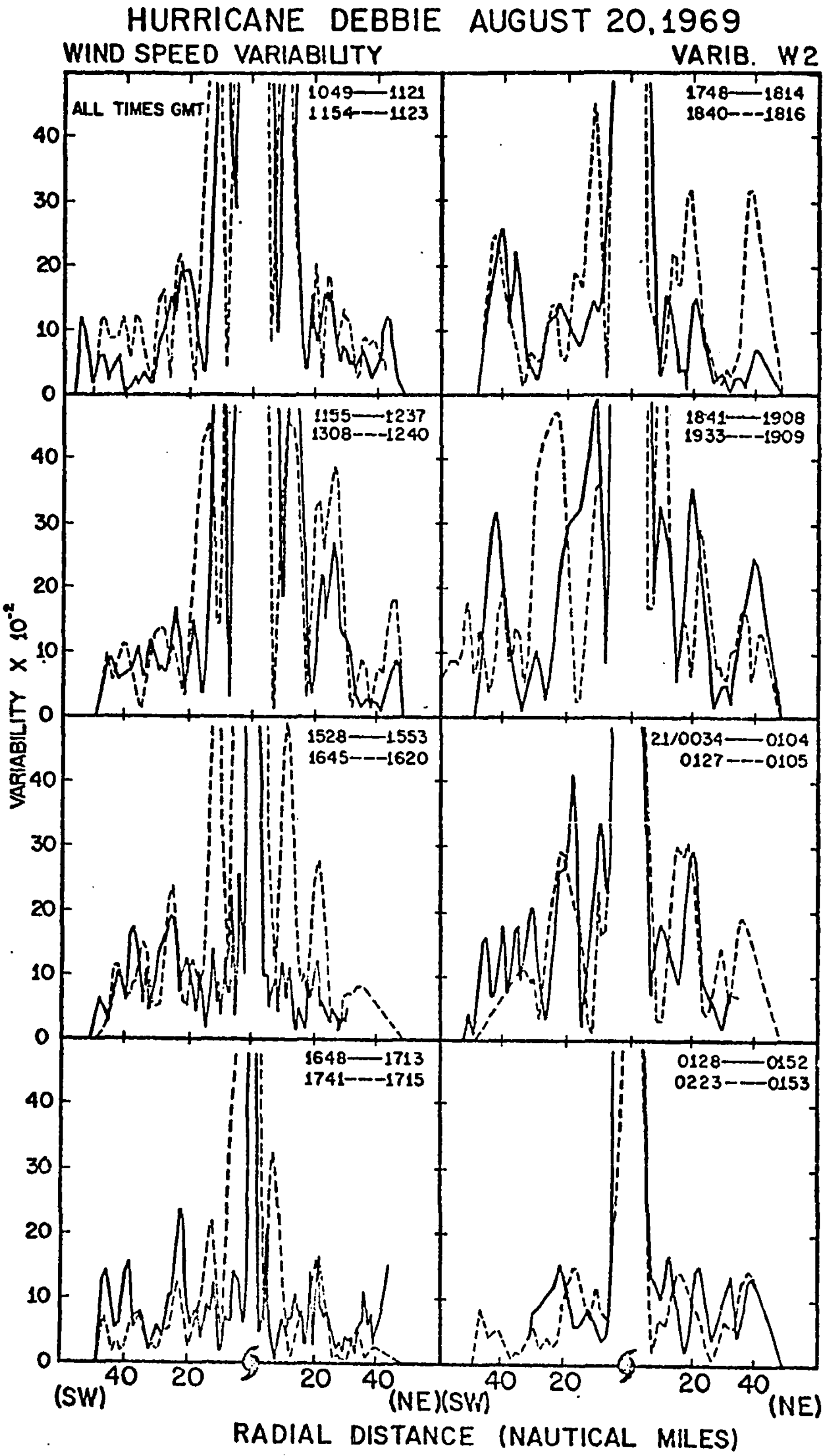

Fig. 46. Relative wind speed variability profiles for approximate rainband scale motion.

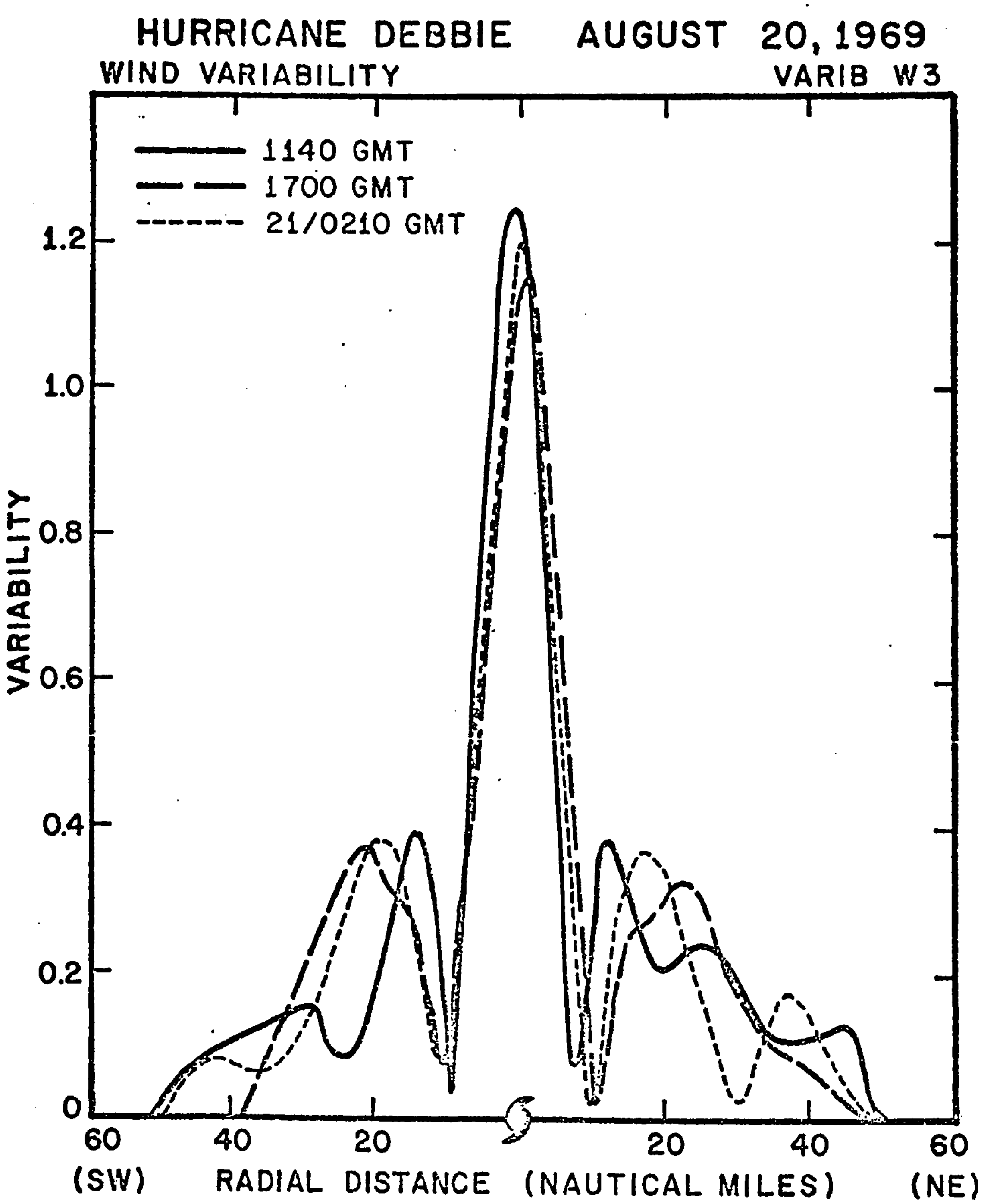

Fig. 47. Relative wind speed variability profiles for approximate eyewall scale motion.

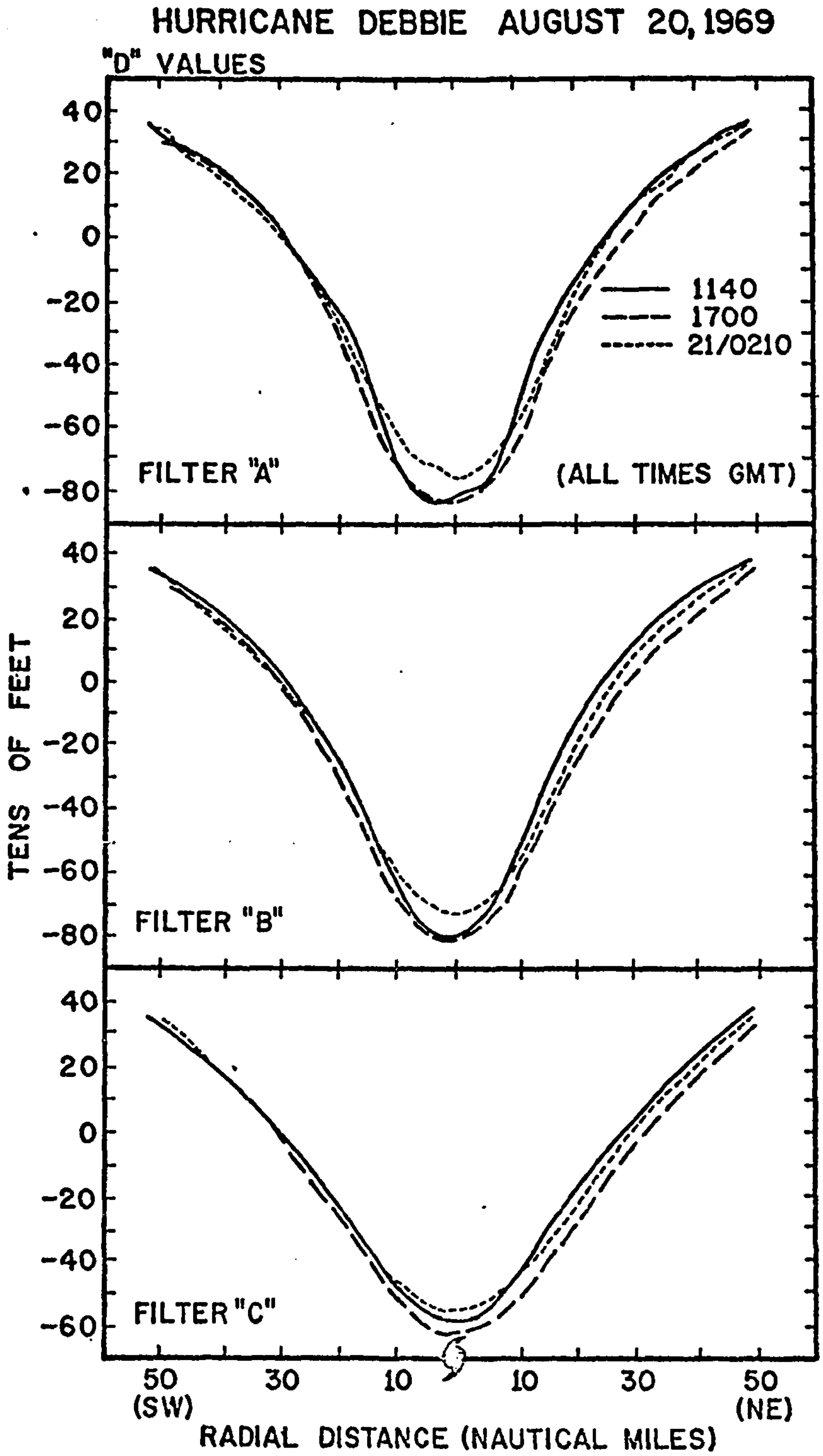

Fig. 48. Profiles of "D" values resulting from application of filters "A", "B", and "C" for the periods of before, during and after the series of seeding events.

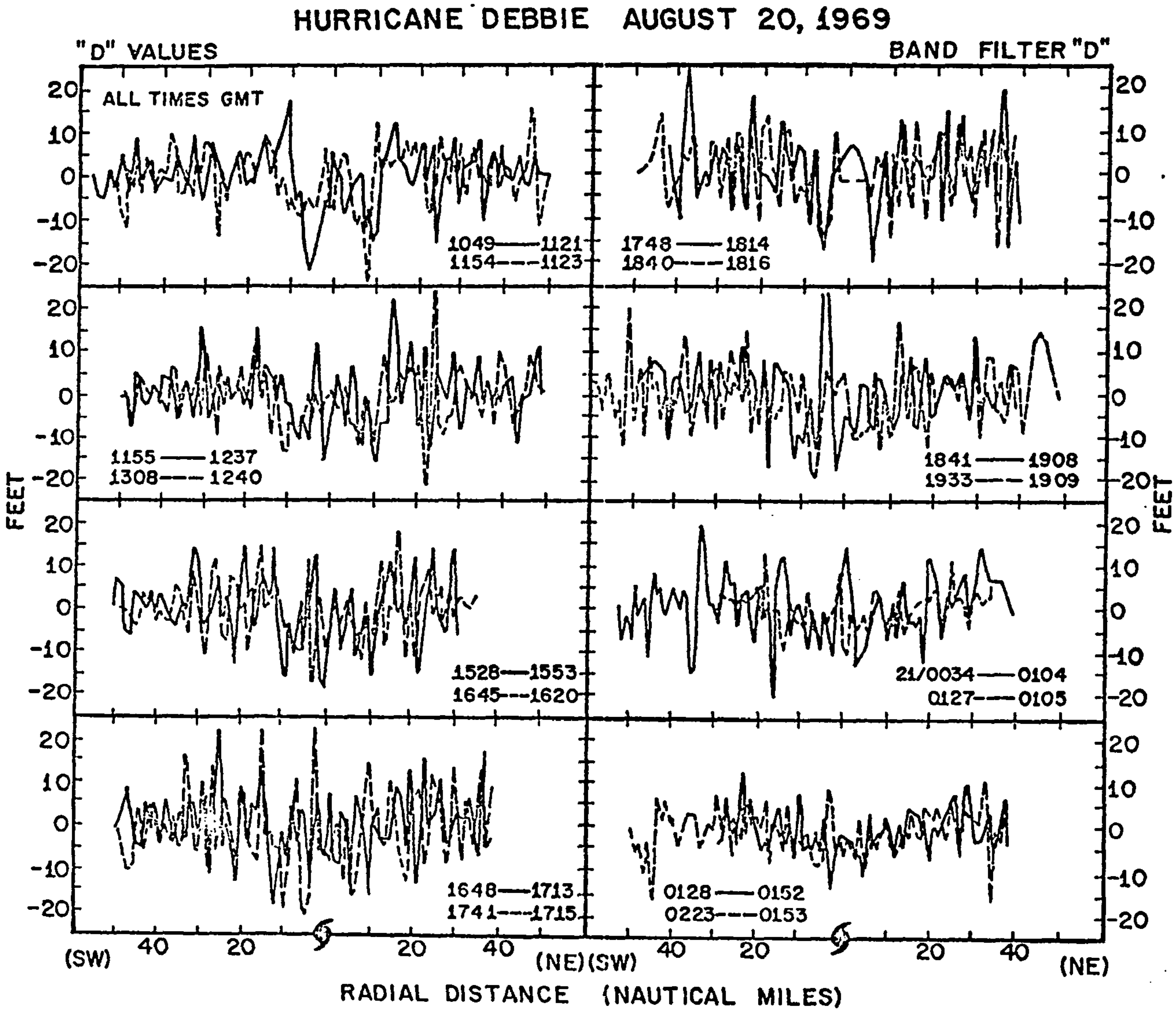

Fig. 49. Profiles of "D" values resulting from application of band filter "D" (~ cumulonimbus scale) to the observed data.

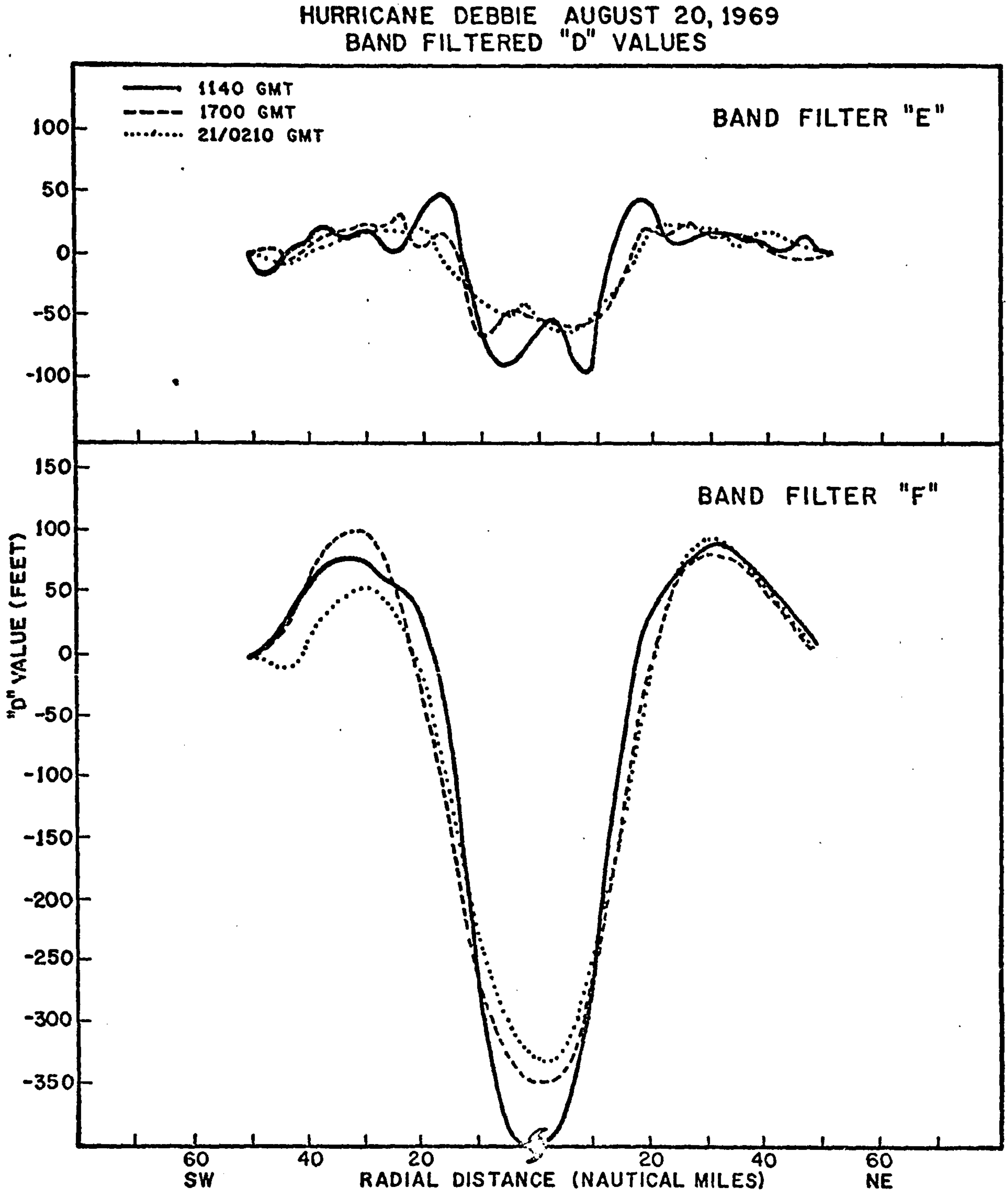

Fig. 50. Profiles of "D" values resulting from application of band filters "E" and "F" (~ rainband and eyewall scales respectively) to the observed data.

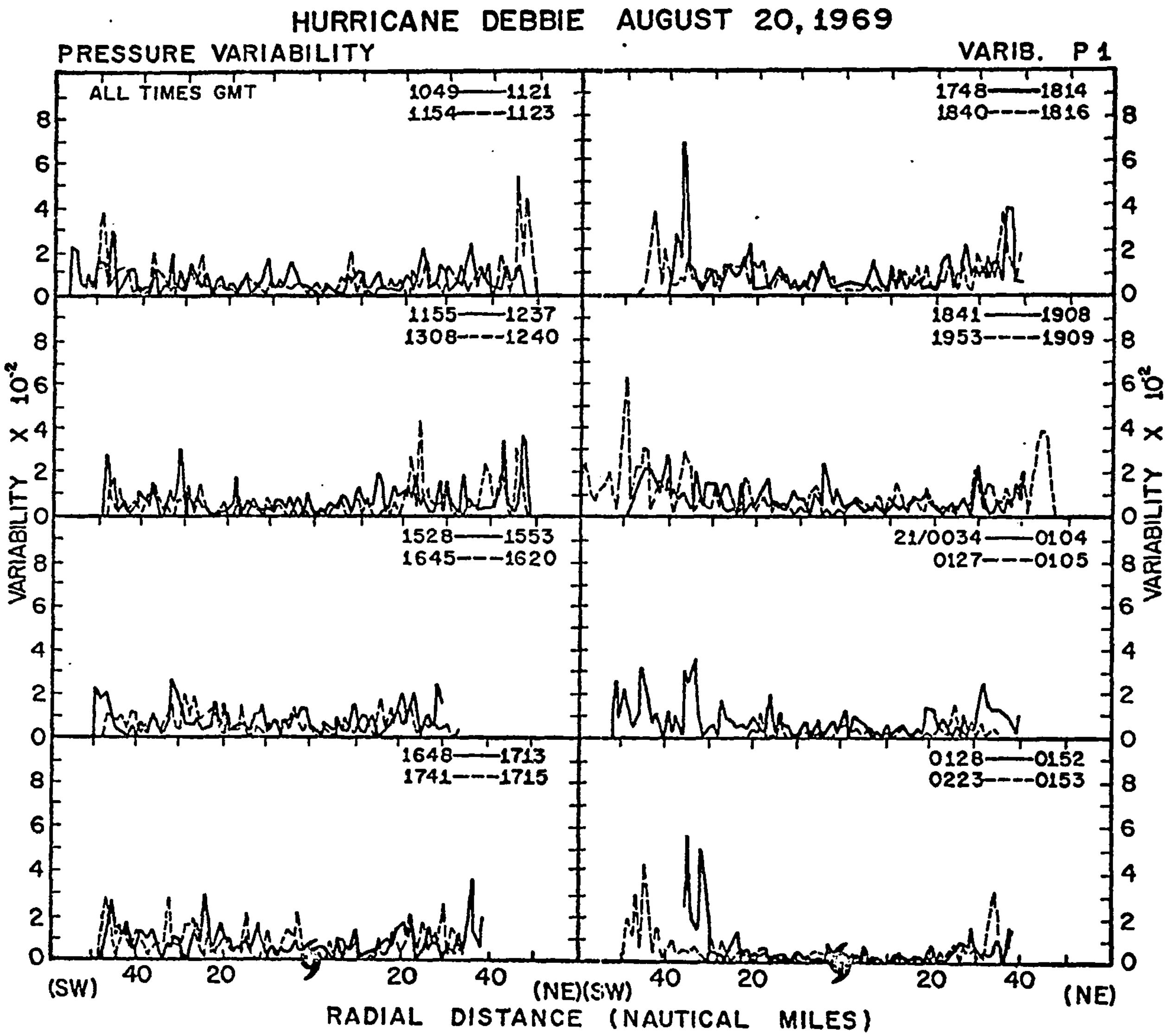

Fig. 51. Pressure variability profiles for approximate cumulonimbus scale motion.

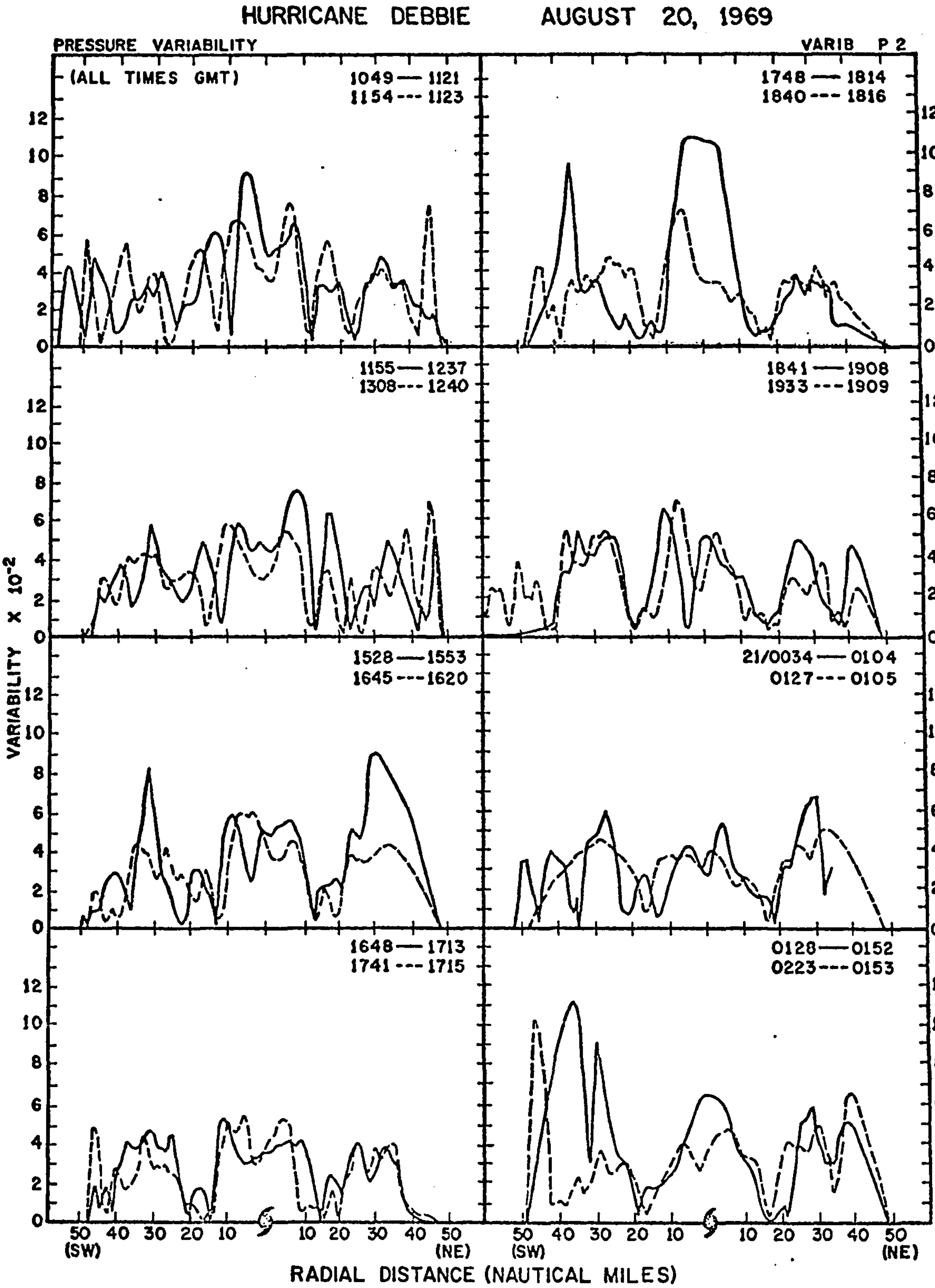

Fig. 52. Pressure variability profiles for approximate rainband scale motion.

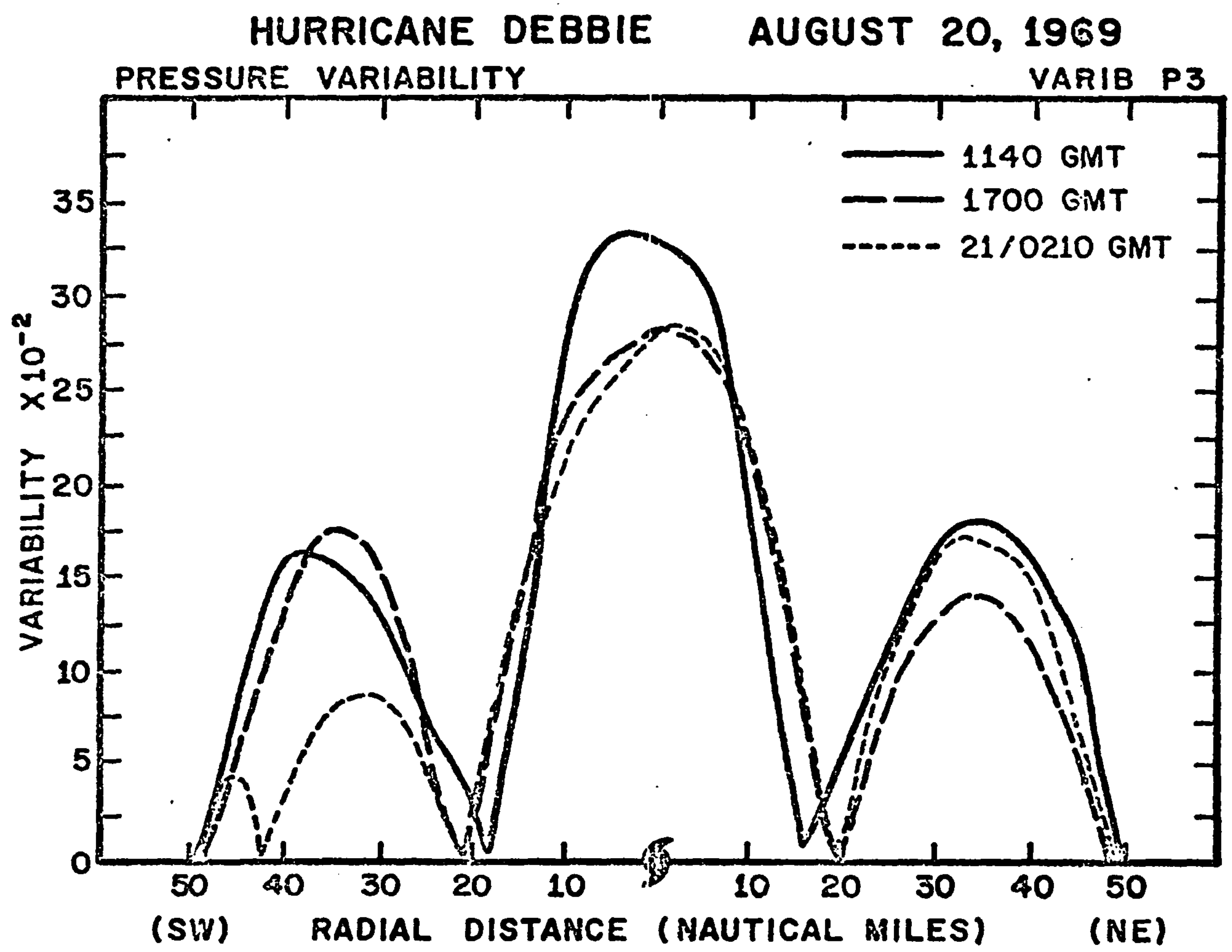

Fig. 53. Pressure variability profiles for approximate eyewall scale motion.

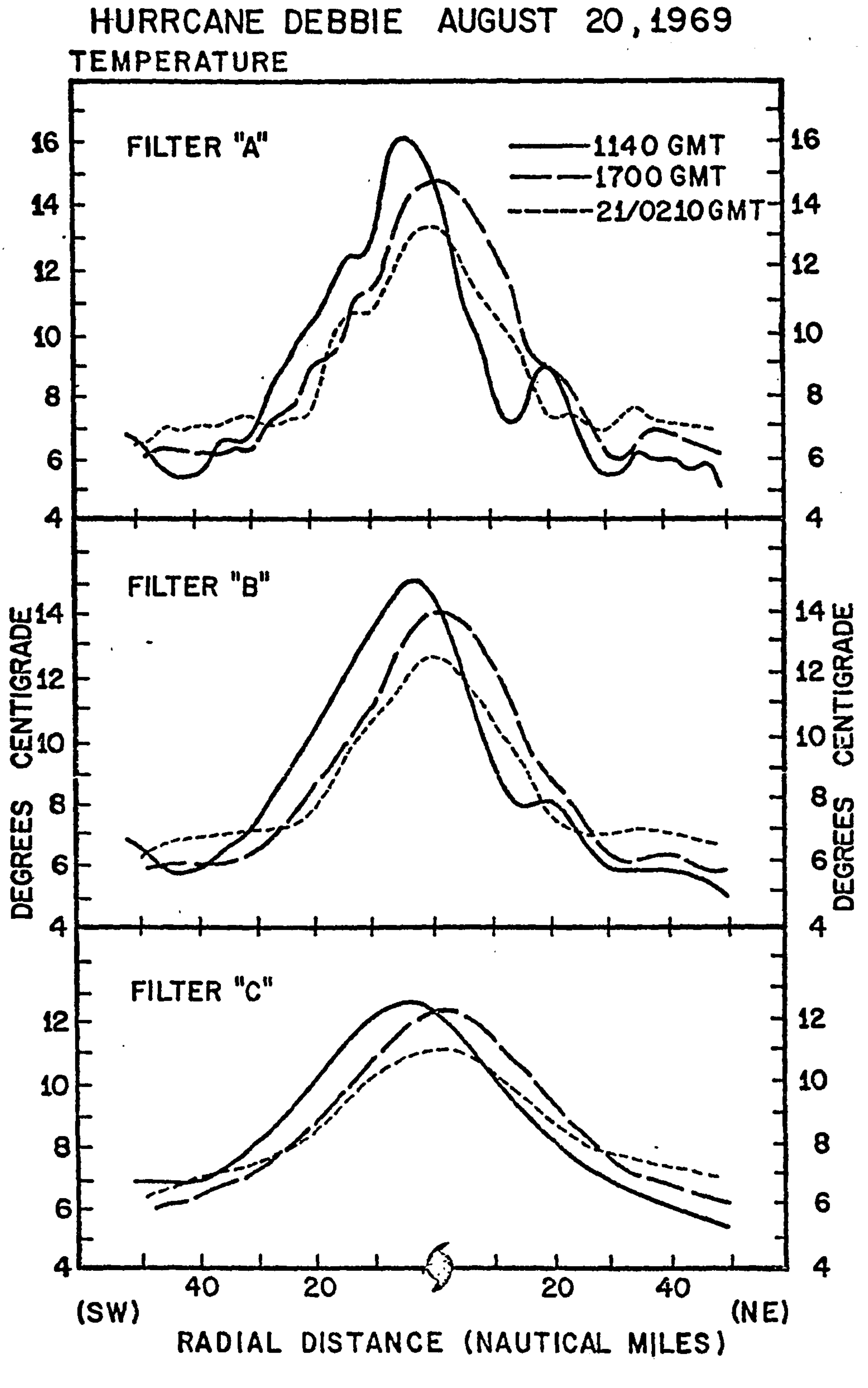

Fig. 54. Temperature profiles resulting from application of filters "A", "B", and "C" for the periods of before, during, and after the series of seeding events.

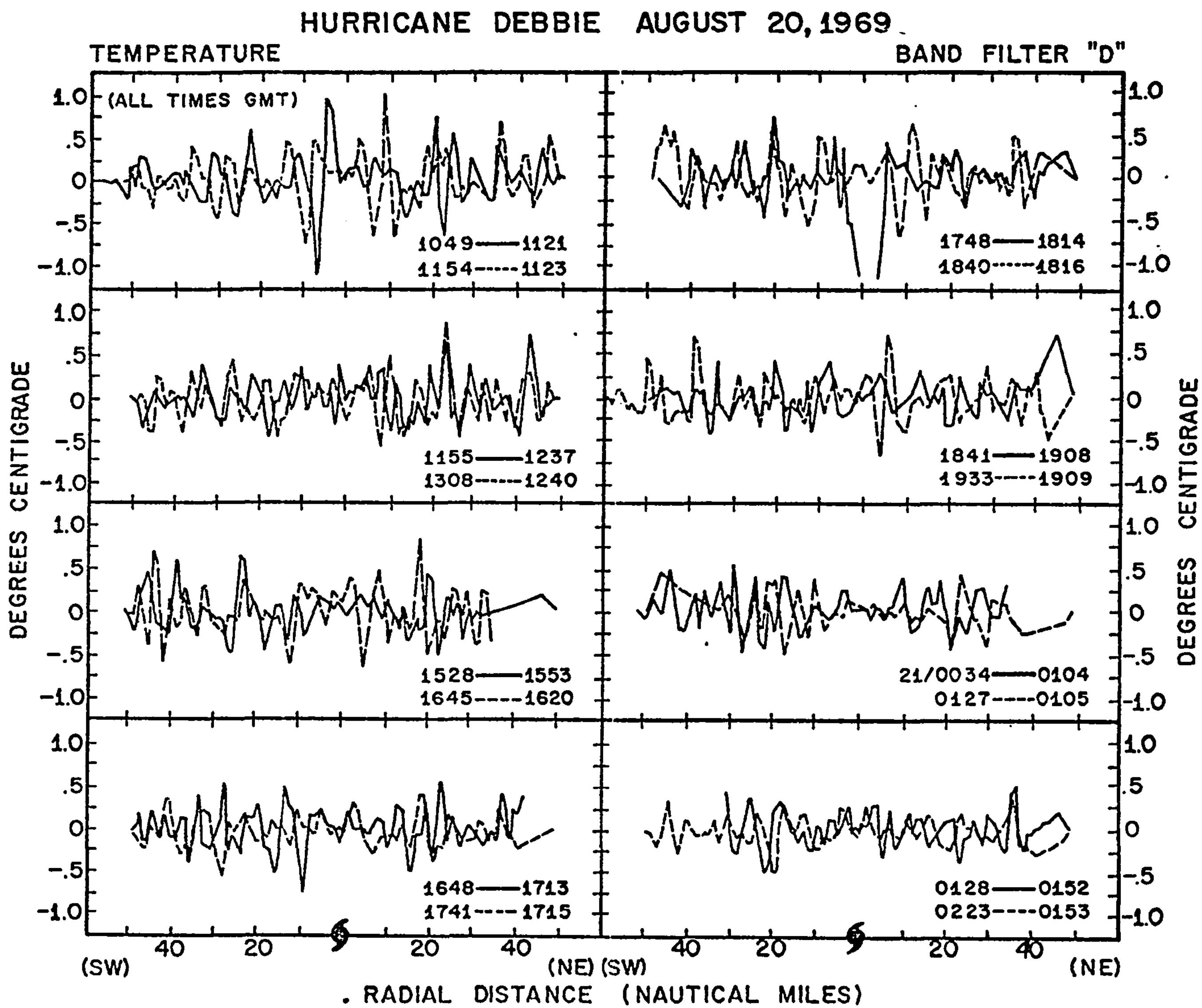

Fig. 55. Temperature profiles resulting from application of band filter "D" (~ cumulonimbus scale) to the observed data.

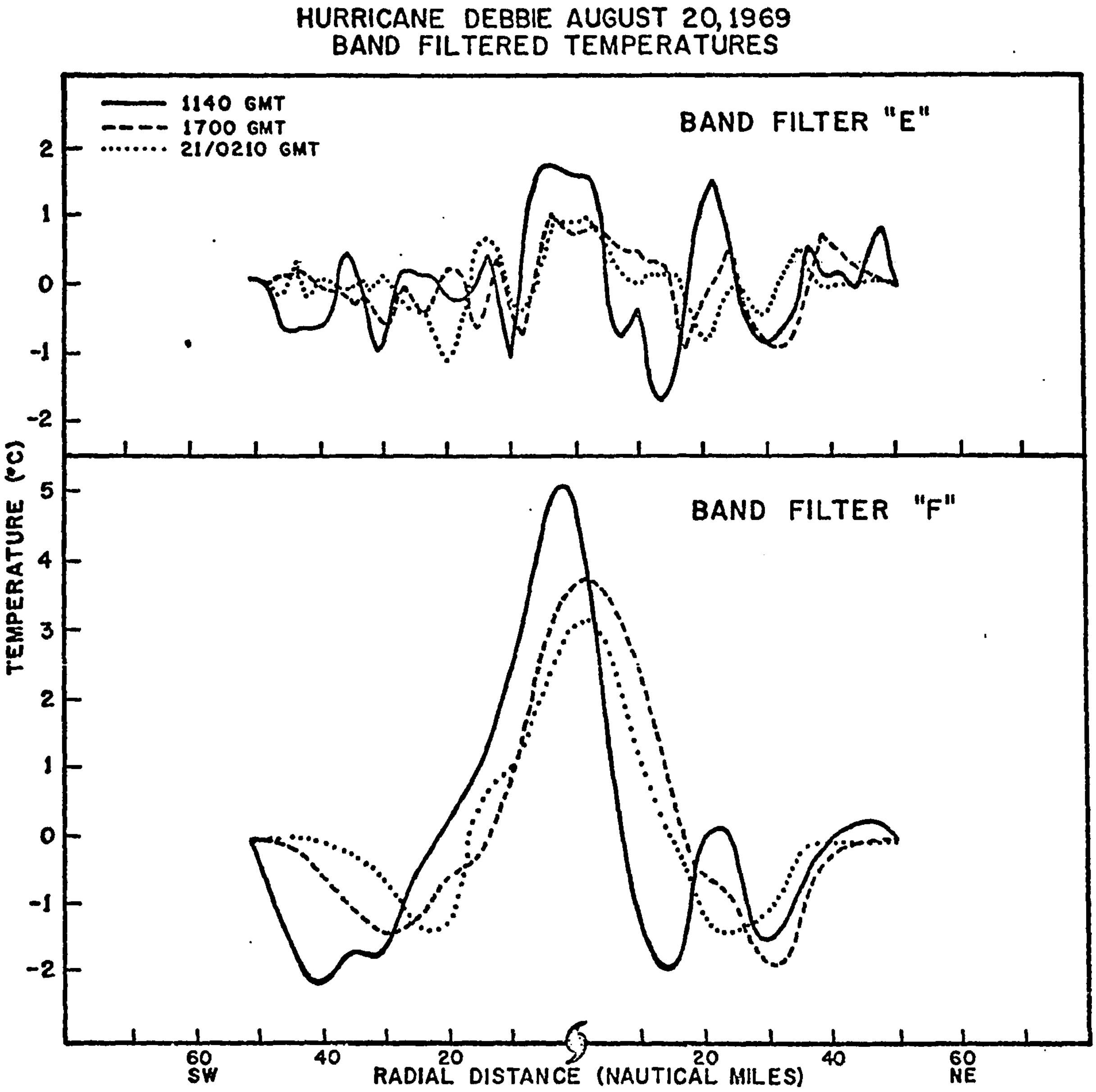

Fig. 56. Temperature profiles resulting from application of band filters "E" and "F" (∿ rainband and eyewall scales respectively) to the observed data.

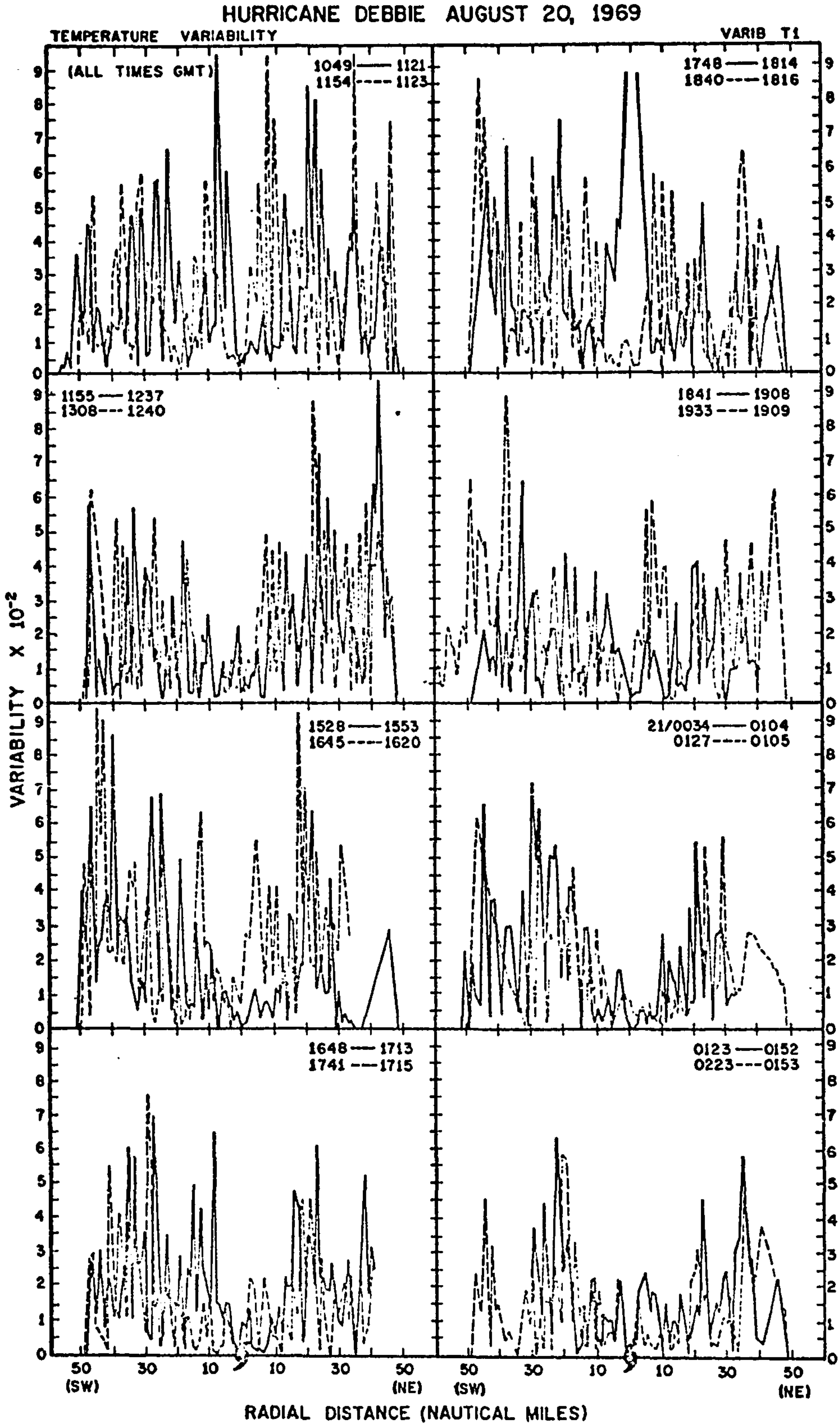

Fig. 57. Temperature variability profiles for approximate cumulonimbus scale motion.

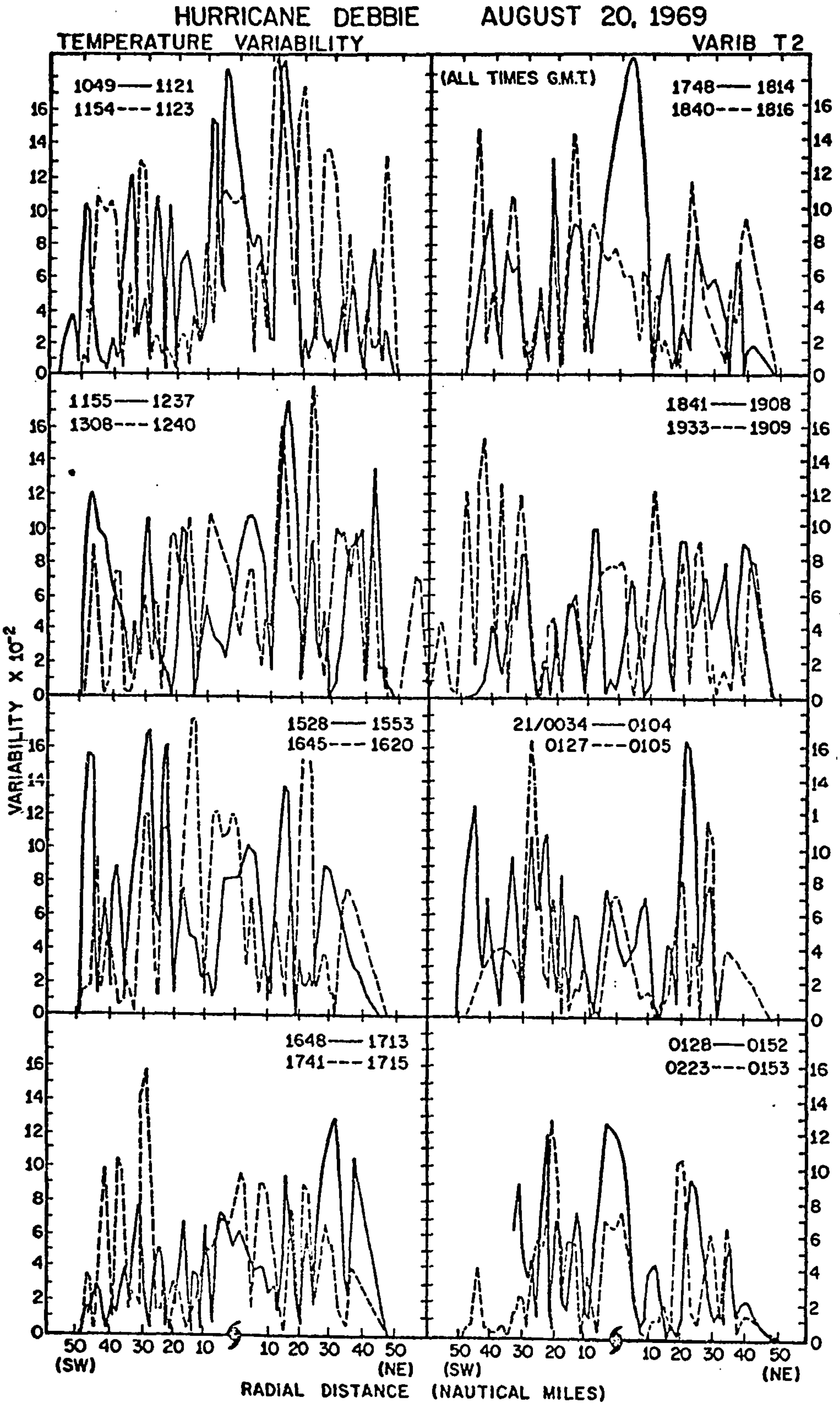

Fig. 58. Temperature variability profiles for approximate rainband scale motion.

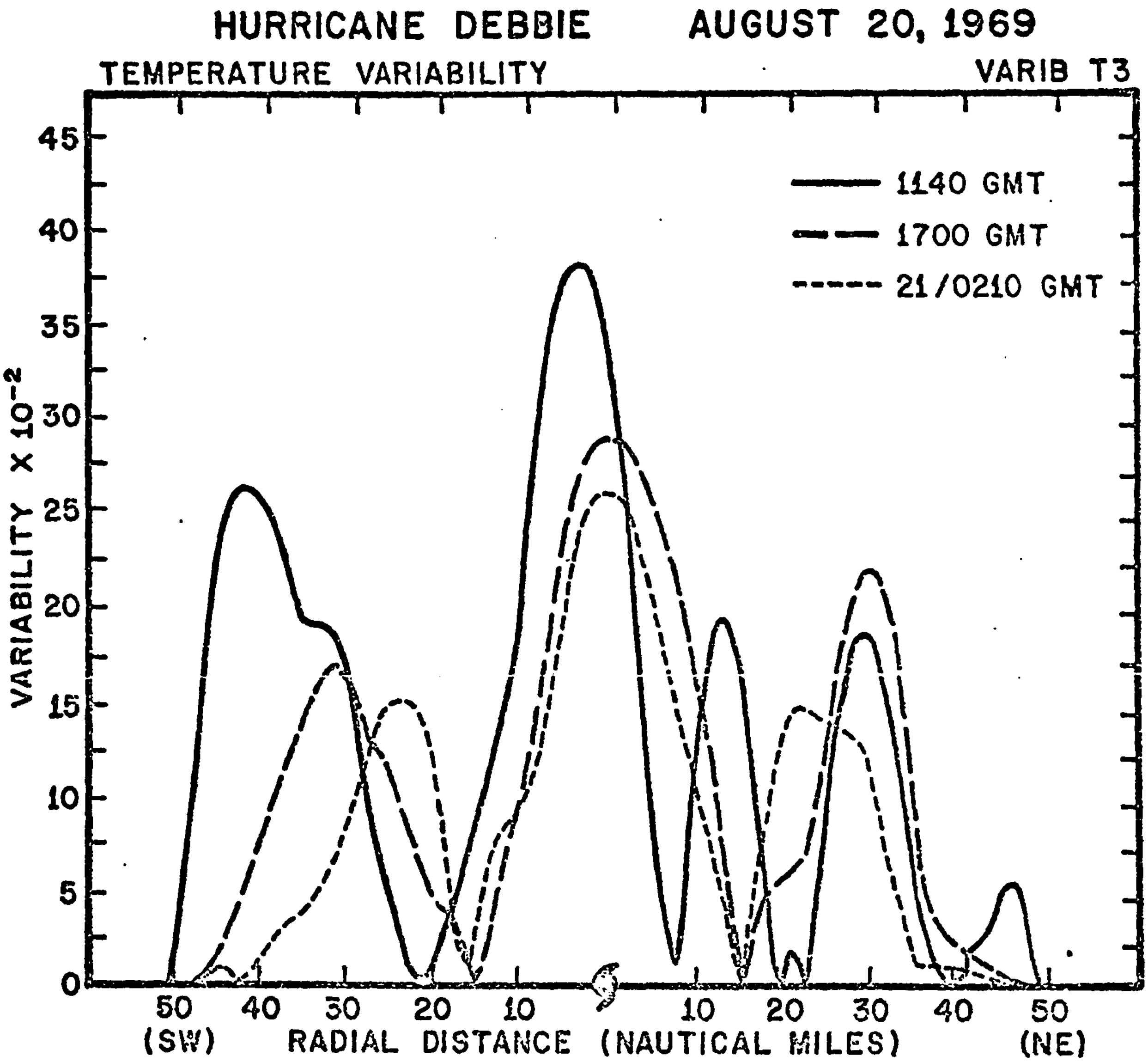

Fig. 59. Temperature variability profiles for approximate eyewall scale motion.

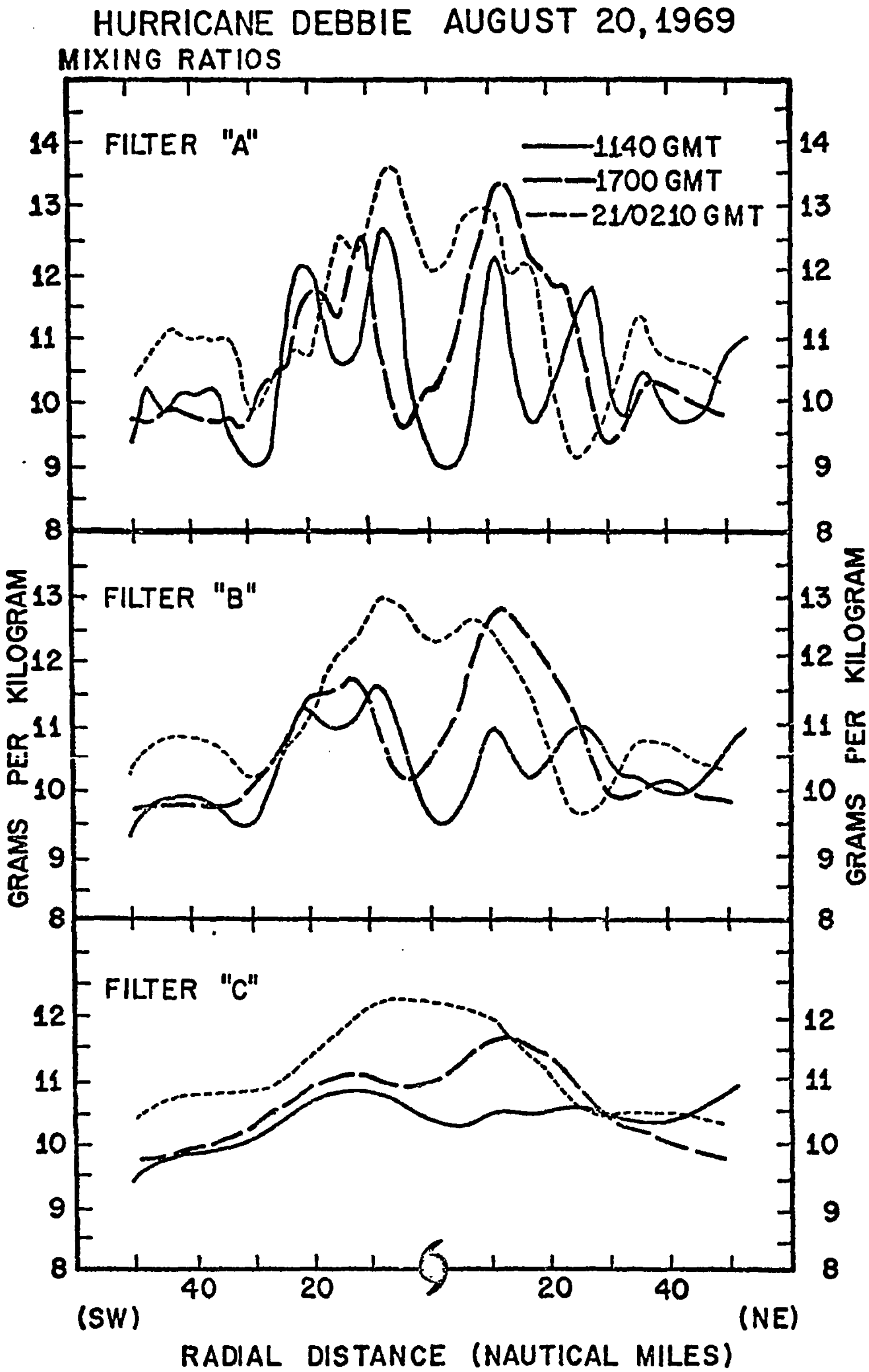

Fig. 60. Mixing ratio profiles resulting from application of filters "A", "B", and "C" to the observed data for the periods of before, during, and after the series of seeding events.

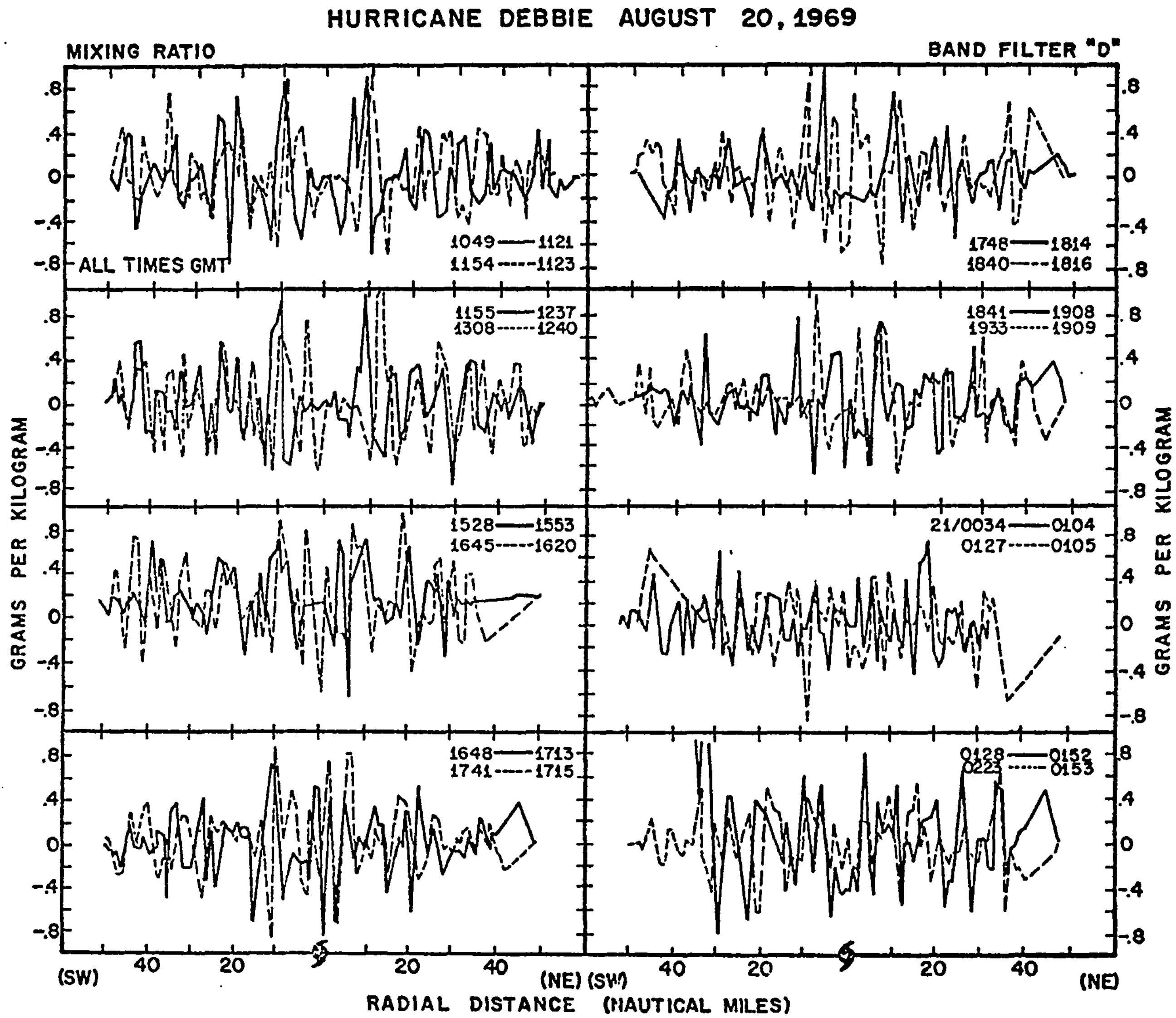

Fig. 61. Mixing ratio profiles resulting from application of band filter "D" (~ cumulonimbus scale) to the observed data.

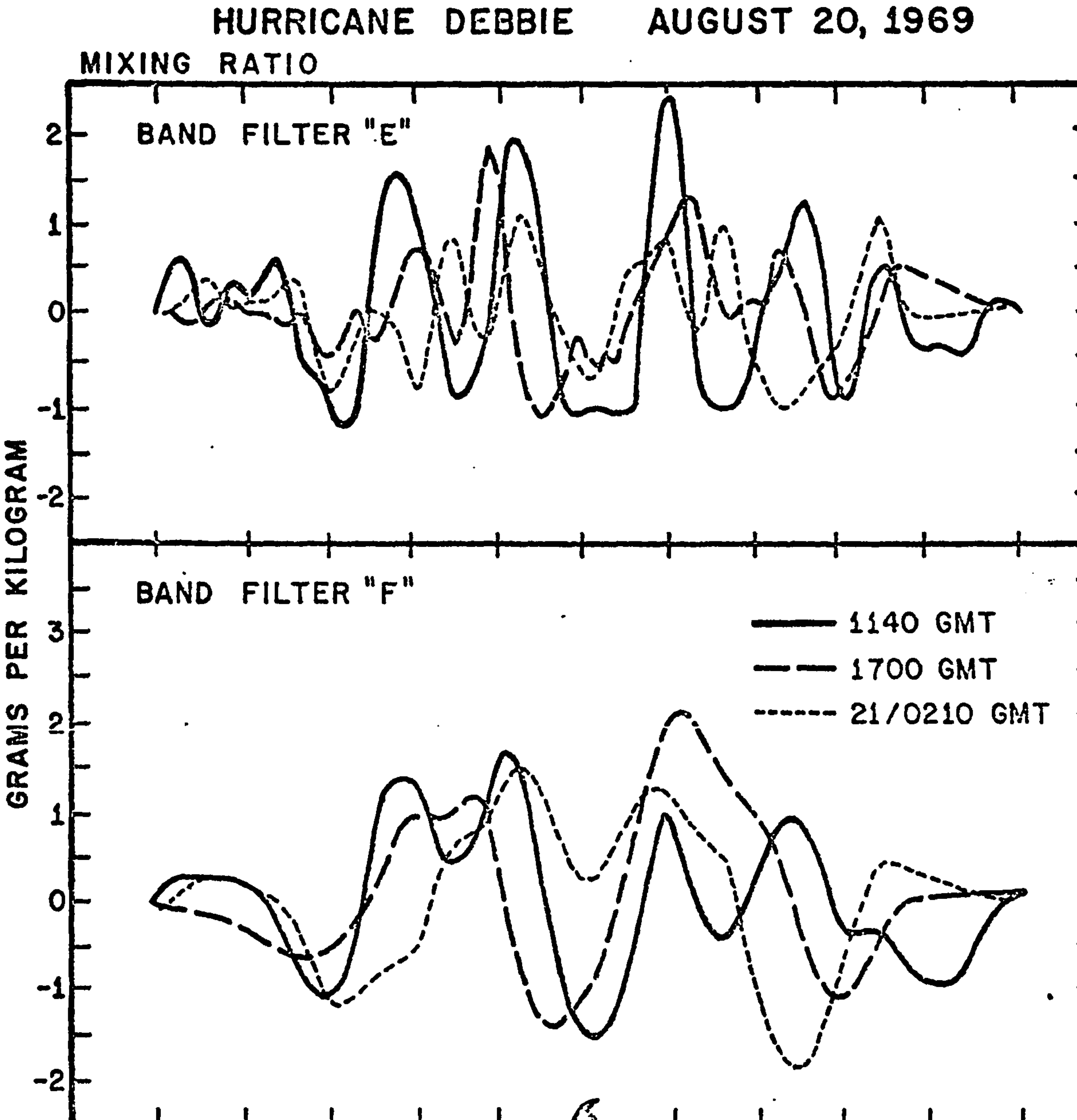

Fig. 62. Mixing ratio profiles resulting from application of band filters "E" and "F" (~ rainband and eyewall scales respectively) to the observed data.

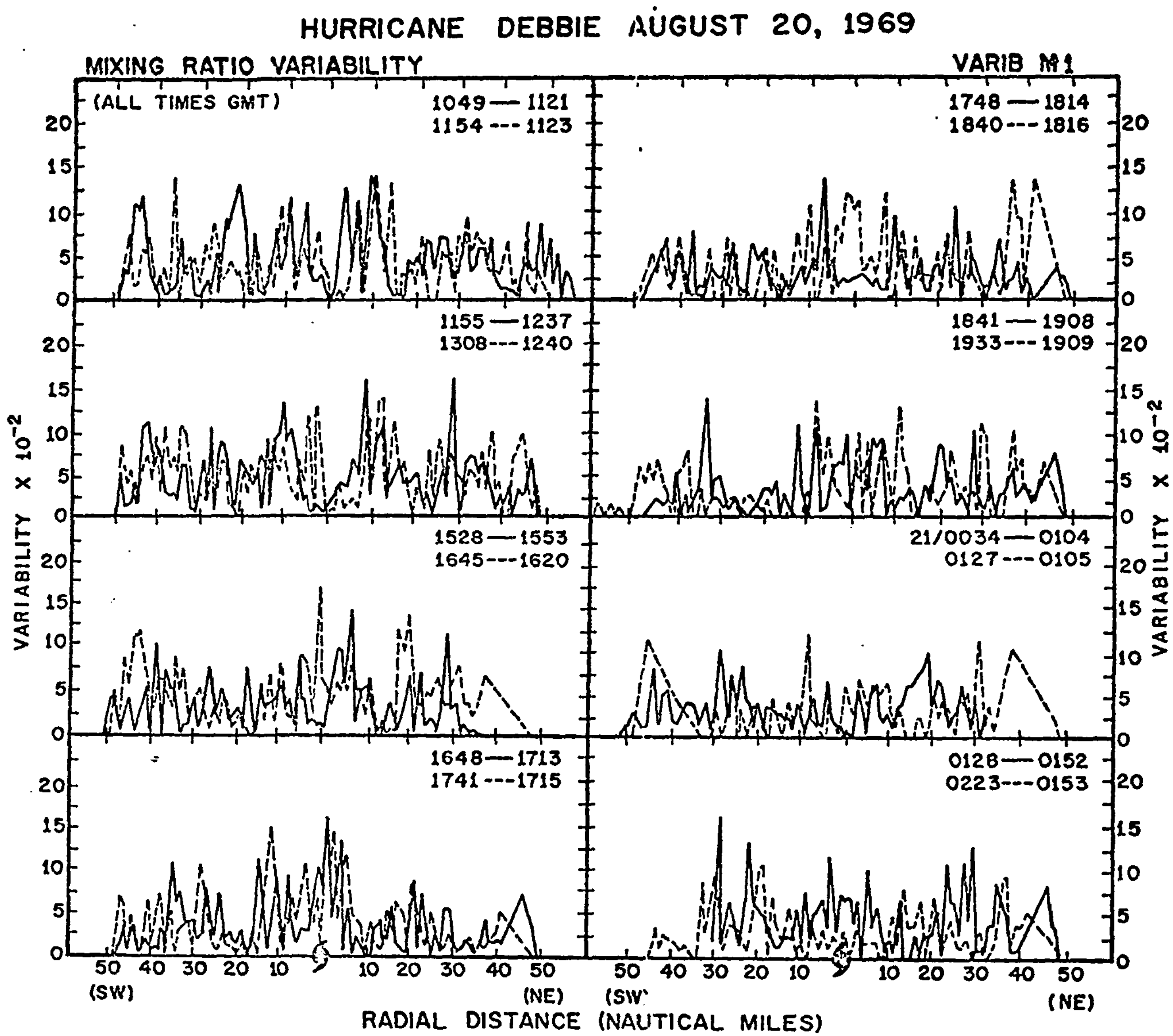

Fig. 63. Moisture variability profiles for approximate cumulonimbus scale motion.

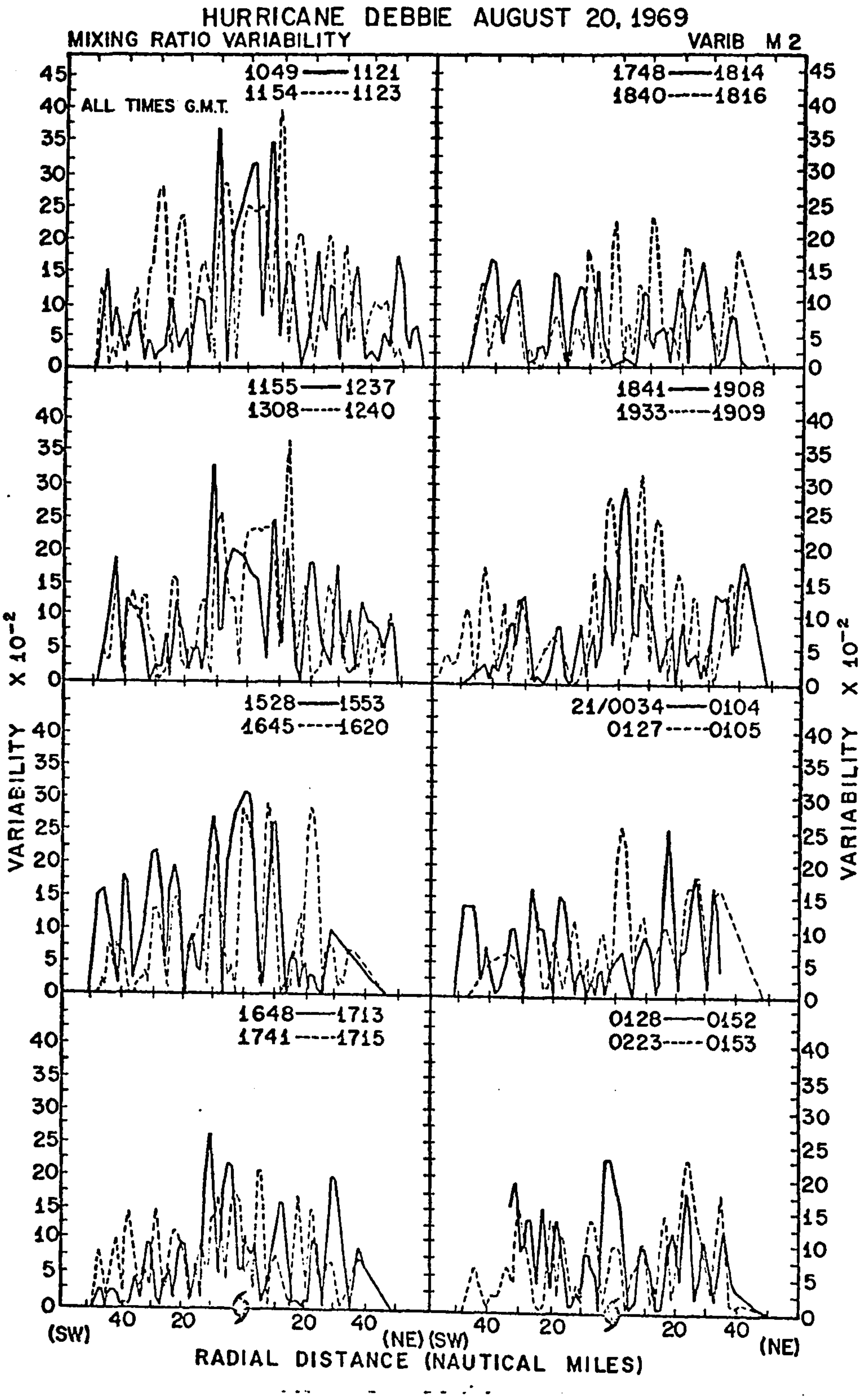

Fig. 64. Moisture variability profiles for approximate rainband scale motion.

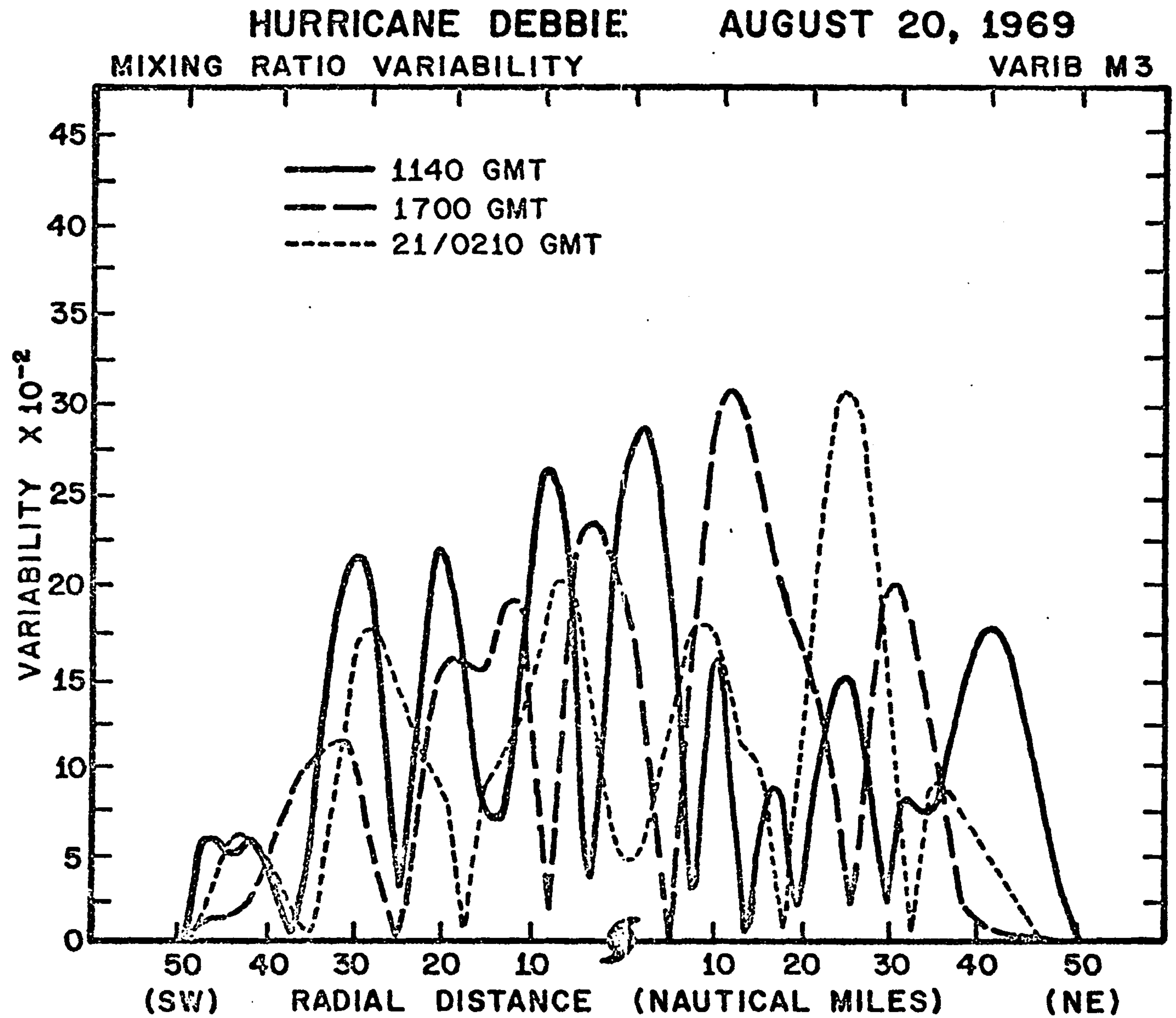

Fig. 65. Moisture variability profiles for approximate eyewall scale motion.

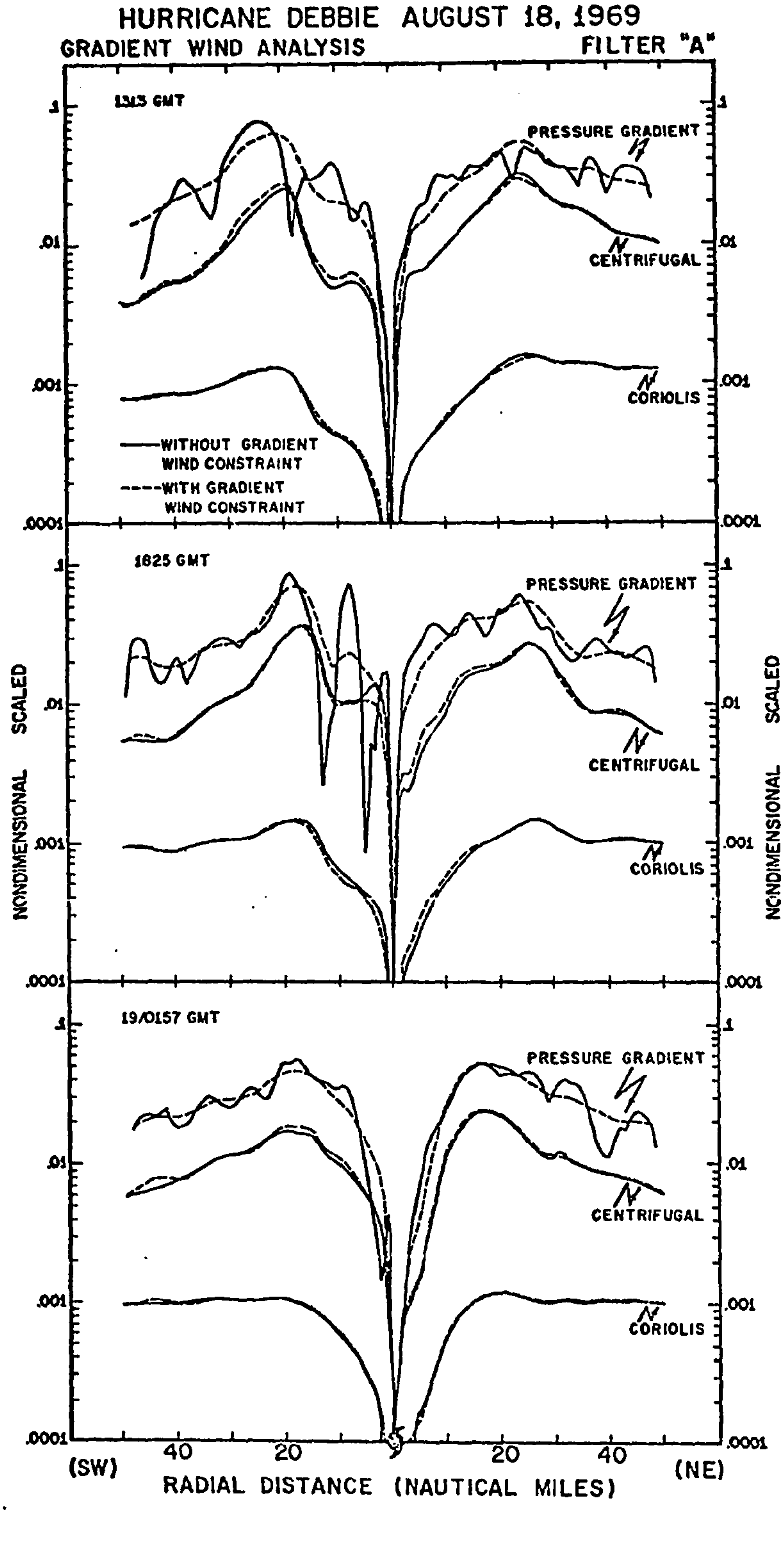

Fig. 66. Gradient wind component analysis resulting from application of filter "A", with and without gradient wind constraint, to the observed pressure and wind fields.

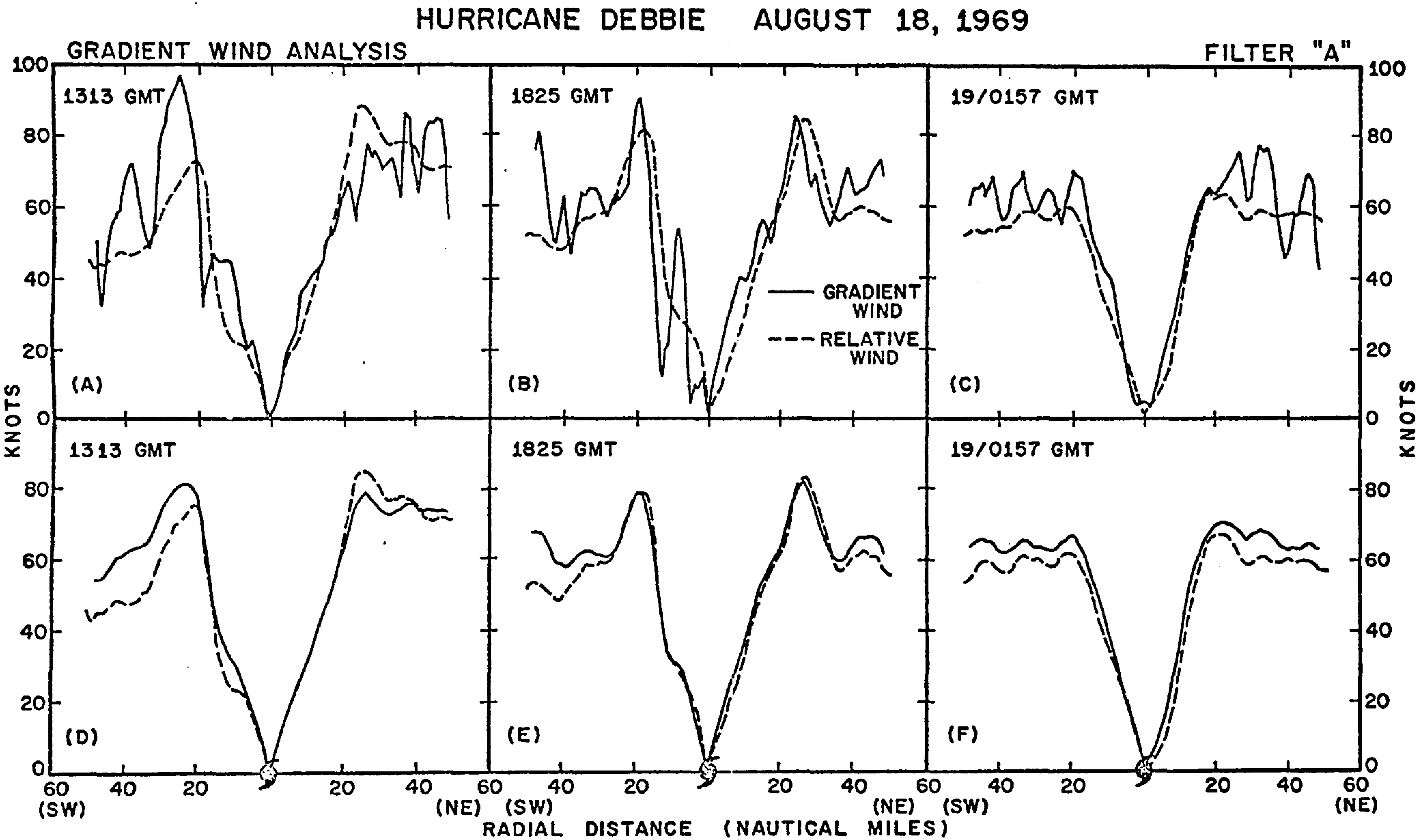

Fig. 67. Wind speed profiles resulting from application of filter "A" with (D, E, and F) and without (A, B, and C) the gradient wind constraint. The relative wind speed is obtained directly from the analysis while the gradient wind profile is computed from the resulting pressure field.

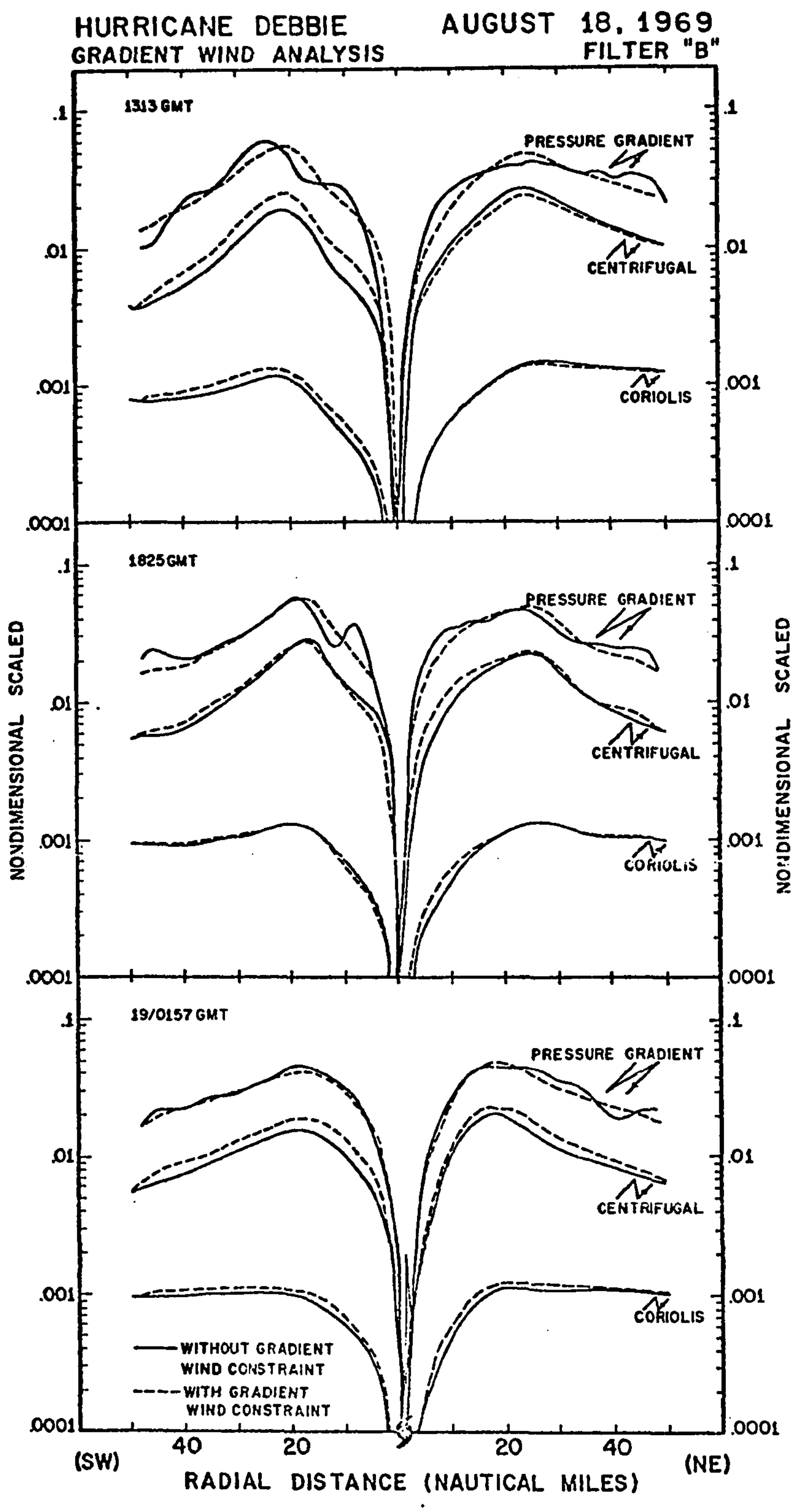

Fig. 68. Gradient wind component analysis resulting from application of filter "B", with and without the gradient wind constraint, to the observed pressure and wind fields.

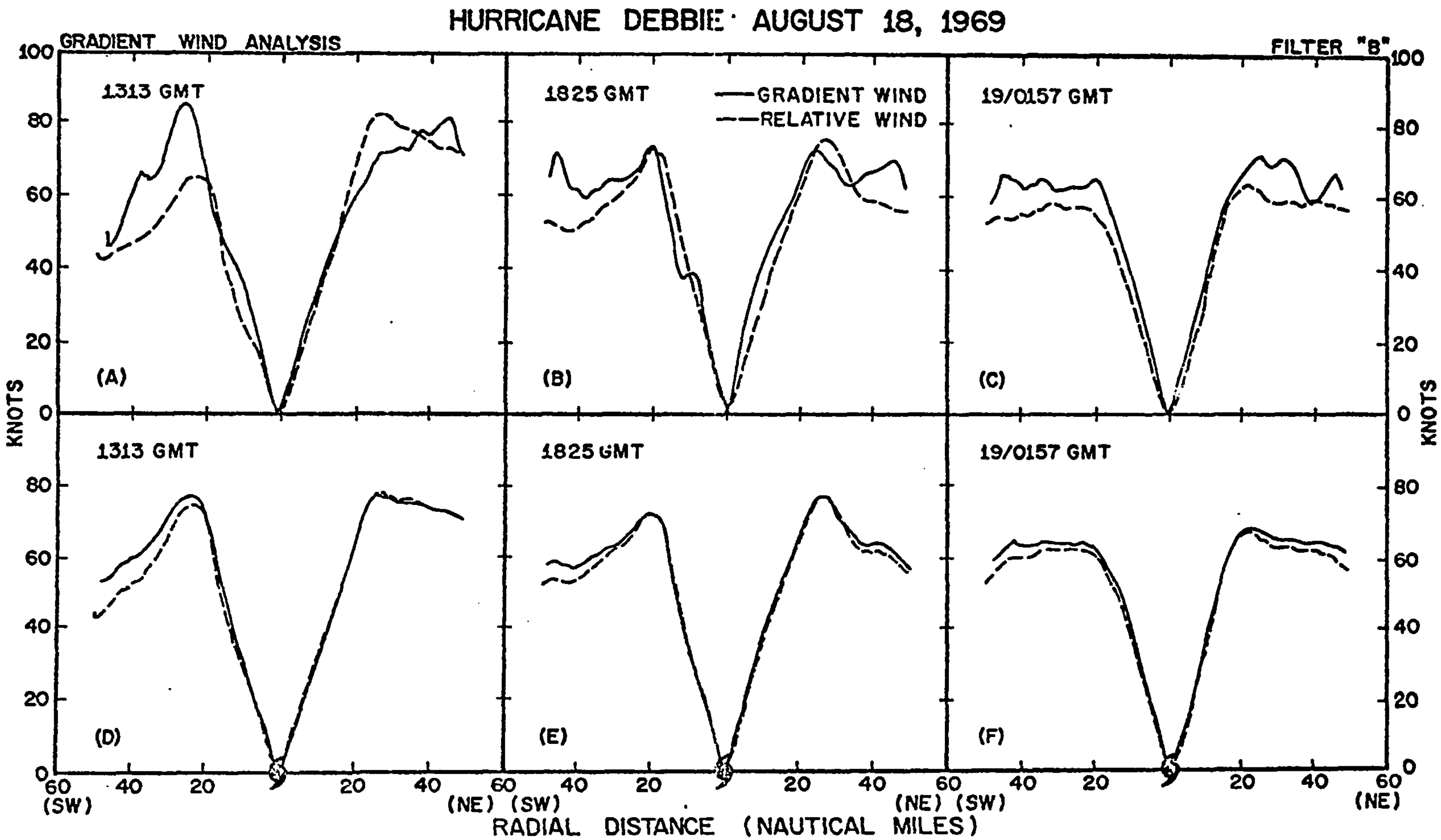

Fig. 69. Wind speed profiles resulting from application of filter "B", with (D, E, and F) and without (A, B, and C) the gradient wind constraint. The relative wind speed results directly from the analysis, while the gradient wind is computed from the resulting pressure field.

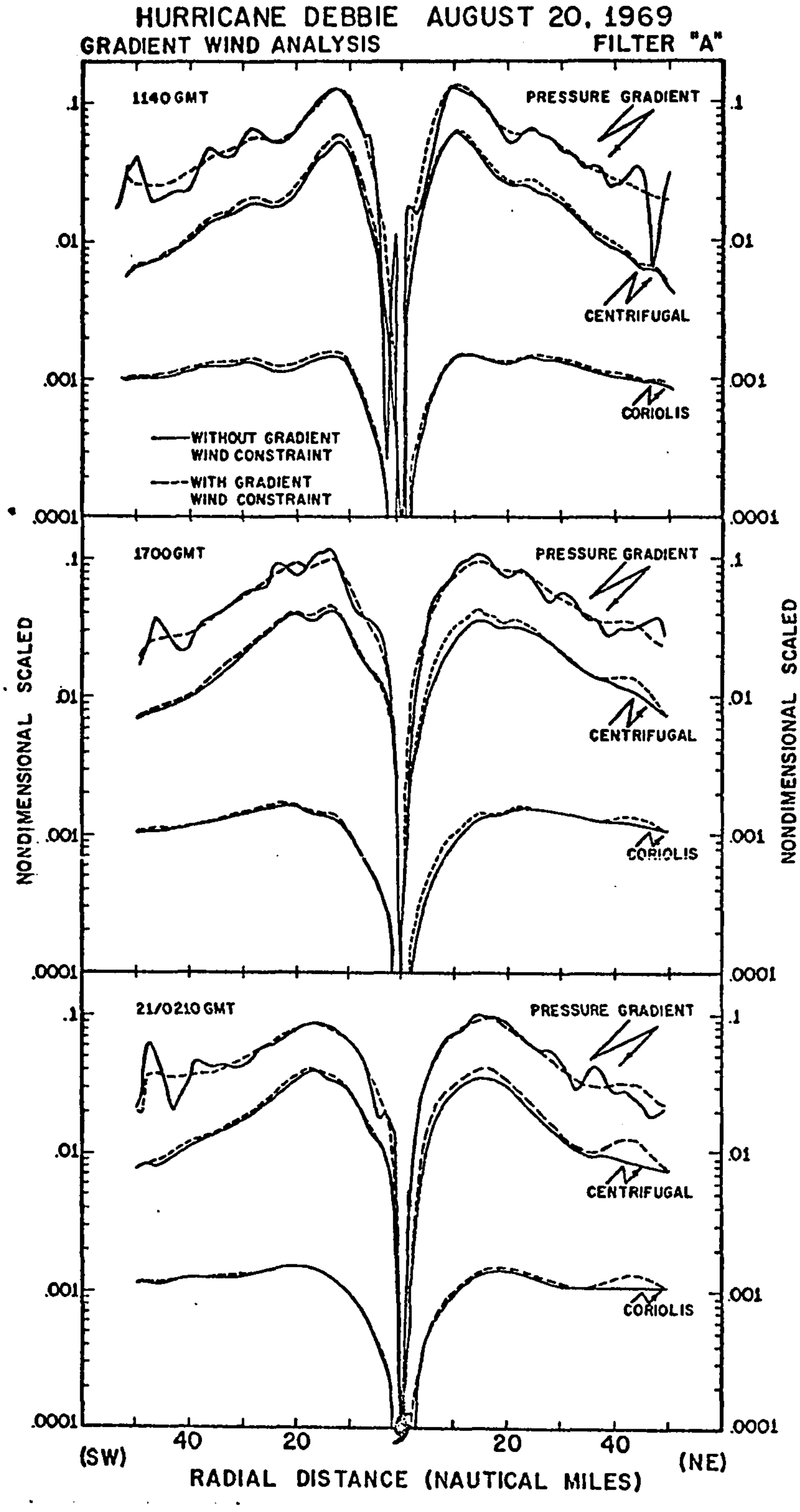

Fig. 70. Gradient wind component analysis resulting from application of filter "A", with and without the gradient wind constraint, to the observed pressure and wind fields.

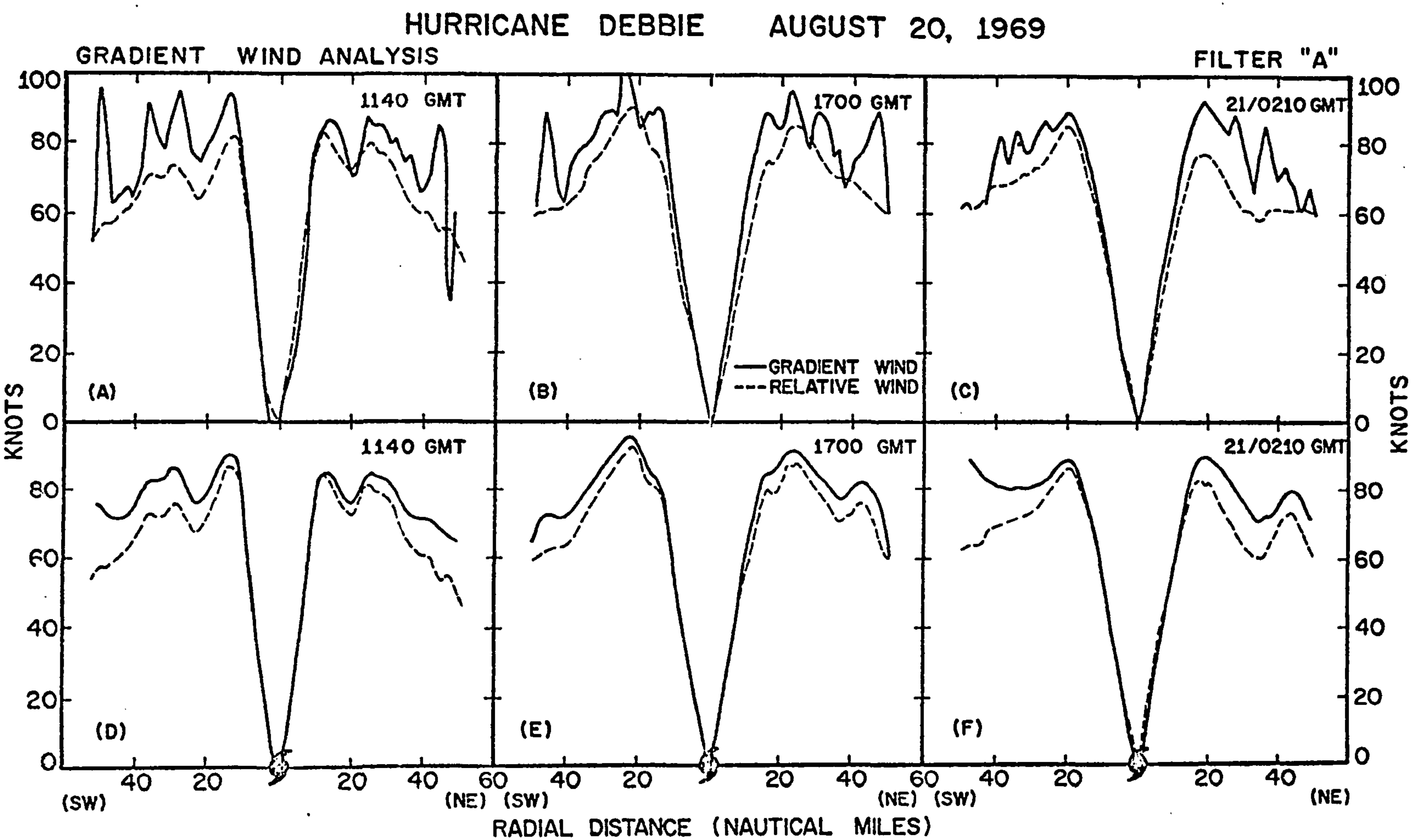

Fig. 71. Wind speed profiles resulting from application of filter "A", with (D, E, and F) and without (A, B, and C) the gradient wind constraint. The relative wind speed results directly from the analysis, while the gradient wind profile is computed from the resulting pressure field.

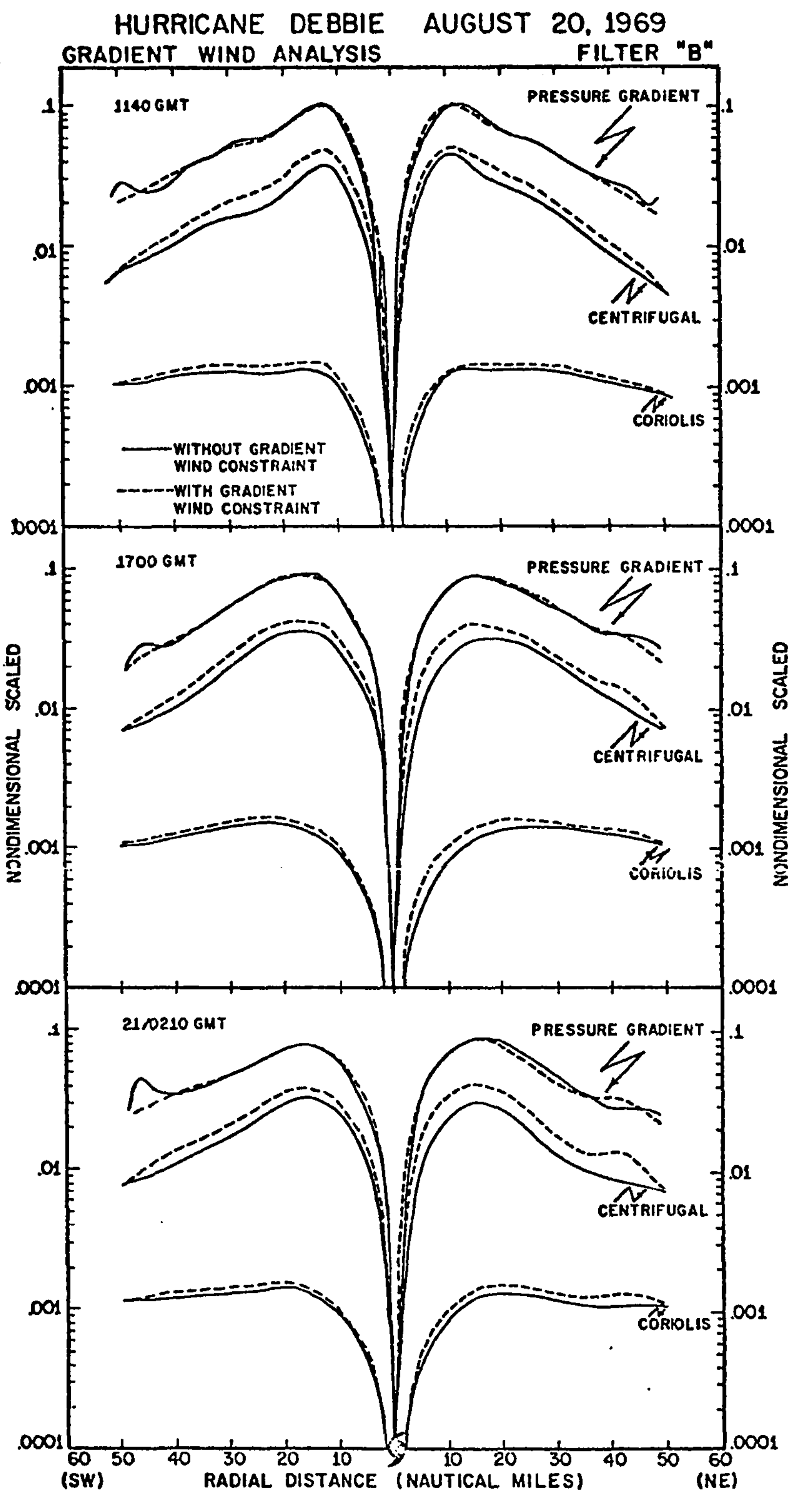

Fig. 72. Gradient wind component analysis resulting from application of filter "B", with and without the gradient wind constraint, to the observed pressure and wind fields.

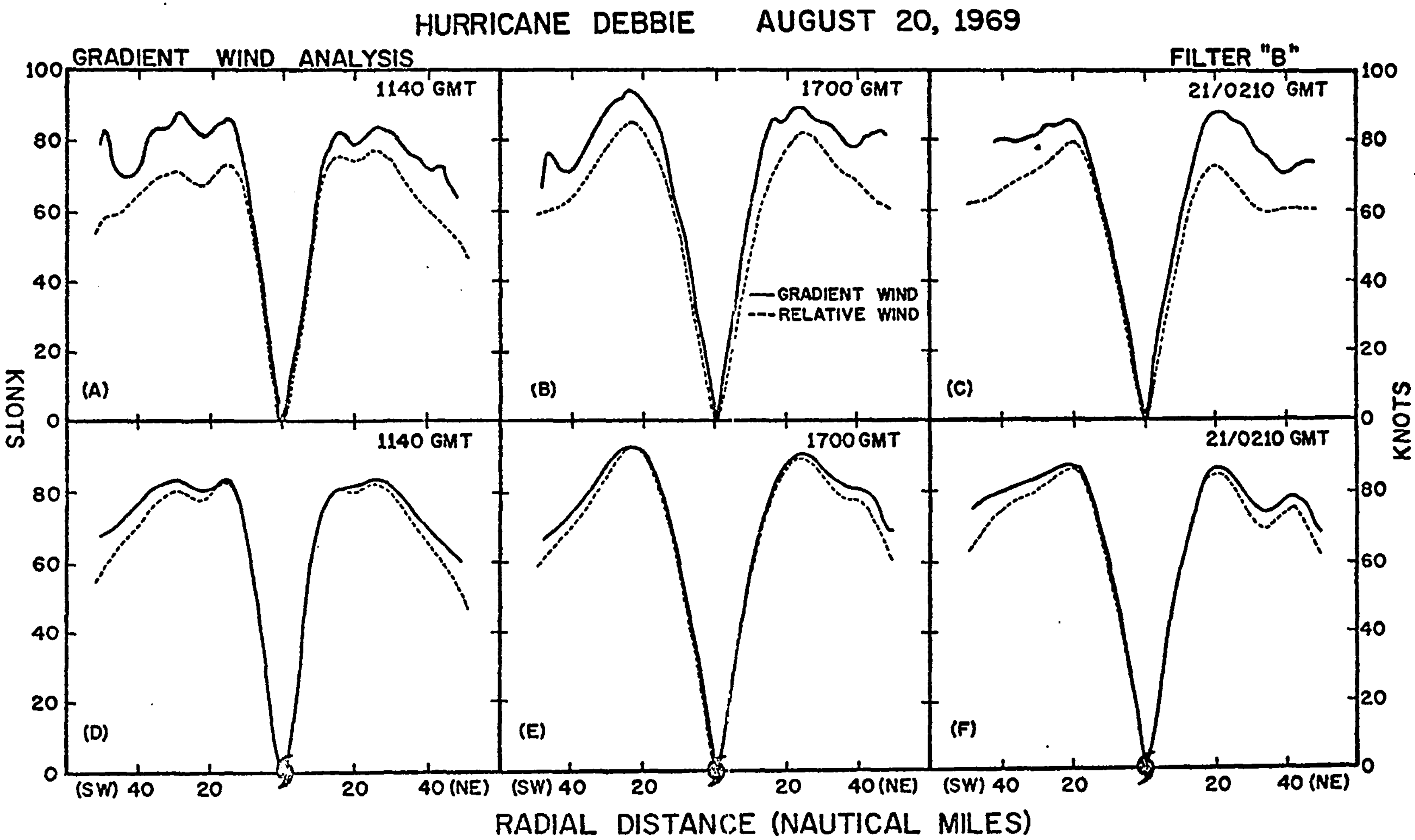

Fig. 73. Wind speed profiles resulting from application of filter "B", with (D, E, and F) and without (A, B, and C) the gradient wind constraint. The relative wind speed results directly from the analysis, while the gradient wind is computed from the resulting pressure field.